Title

RESONANCE PRODUCTION, PARTICULARLY Y1* (1385) AND p , IN K-p->An+non- AND K-p->An+n-; PK =2.1-2.7 BeV/c

Author

Siegel, Daniel M.

Publication Date

1967-12-26

UCRL-18041

cy. 2

University of California

Ernest O. Lawrence Radiation Laboratory

RESONANCE PRODUCTION, PARTICULARLY $Y_1^*(1385)$ AND ρ, IN $K^-p \rightarrow \Lambda\pi^+\pi^0\pi^-$ AND $K^-p \rightarrow \Lambda\pi^+\pi^-$; $p_{K^-} = 2.1 - 2.7$ BeV/c

Daniel M. Siegel
(Ph.D. Thesis)

December 26, 1967

E-LRL

DISCLAIMER

UCRL-18041

UNIVERSITY OF CALIFORNIA

Lawrence Radiation Laboratory
Berkeley, California

AEC Contract No. W-7405-eng-48

RESONANCE PRODUCTION, PARTICULARLY $Y_1^*(1385)$ AND ρ, IN $K^-p \rightarrow \Lambda\pi^+\pi^0\pi^-$ AND $K^-p \rightarrow \Lambda\pi^+\pi^-$; $p_{K^-} = 2.1 - 2.7$ BeV/c

Daniel M. Siegel
(Ph.D. Thesis)

December 26, 1967

RESONANCE PRODUCTION, PARTICULARLY $Y_1^*(1385)$ AND ρ, IN $K^- p \to \Lambda\pi^+\pi^0\pi^-$ AND $K^- p \to \Lambda\pi^+\pi^-$; p_{K^-} = 2.1-2.7 BeV/c

Contents

RESONANCE PRODUCTION, PARTICULARLY $Y_1^*(1385)$ AND ρ, IN $K^- p \to \Lambda \pi^+ \pi^0 \pi^-$ AND $K^- p \to \Lambda \pi^+ \pi^-$; $p_{K^-} = 2.1\text{-}2.7$ BeV/c

Daniel M. Siegel

Lawrence Radiation Laboratory
University of California
Berkeley, California

December 26, 1967

ABSTRACT

Some 20,000 $K^- p \to \Lambda \pi^+ \pi^0 \pi^-$ and 10,000 $K^- p \to \Lambda \pi^+ \pi^-$ events are identified in the 72-inch hydrogen bubble chamber. Analysis of these reactions, by means of maximum likelihood fits to comprehensive models involving known resonances, yields cross sections and production angular distributions for quasi-two-body states $Y_1^*(1385)^{\pm}_{0}\ \rho^{\mp}_{0}$, $Y_1^*(1385)^{\pm}\ \pi^{\mp}$, and $\Lambda^0 \rho^0$. Analysis of decay angular distributions for peripheral reactions indicates predominance of K meson exchange for $K^- p \to Y_1^*(1385)^+ \rho^-$, and K^* exchange for $K^- p \to Y_1^*(1385)^+ \pi^-$.

I. INTRODUCTION

This investigation was planned as a systematic experimental analysis of the reactions $K^- p \to \Lambda \pi^+ \pi^o \pi^-$ and $K^- p \to \Lambda \pi^+ \pi^-$, for K^- beam momenta ranging from 2.1 to 2.7 BeV/c. These reactions are dominated by production of known resonances, primarily $Y_1^*(1385)^{\pm}_{o}$, $\rho^{\pm}_{o}$, and ω. The analysis is complicated by the large number of intermediate states involving resonances through which the reactions proceed. Thus for $K^- p \to \Lambda \pi^+ \pi^o \pi^-$, for example, the following intermediate states are significant:

$Y_1^*(1385)^+ \rho^-$

$Y_1^*(1385)^o \rho^o$

$Y_1^*(1385)^- \rho^+$

$Y_1^*(1385)^+ \pi^o \pi^-$

$Y_1^*(1385)^o \pi^+ \pi^-$

$Y_1^*(1385)^- \pi^+ \pi^o$

$\rho^+ \Lambda \pi^-$

$\rho^o \Lambda \pi^o$

$\rho^- \Lambda \pi^+$

$\Lambda \omega$

$\Lambda \eta$

$Y_o^*(1520) \pi^o$

Experimental parameters characterizing these many resonant processes are heavily correlated, and this has lead to the development and use of a maximum likelihood fitting procedure, which allows for simultaneous fitting of large numbers of parameters referring to various resonant processes.

The plan of this report is as follows: Chapter II deals with the gathering of the data and its reduction to useful form. Criteria for the separation of the reactions of interest are discussed here. Chapter III describes the maximum likelihood fitting procedures used to arrive at cross sections and production and decay angular distributions for resonant processes. Chapter IV describes the application of these procedures to the reaction $K^- p \to \Lambda \pi^+ \pi^o \pi^-$. Results, particularly for the resonant processes $K^- p \to Y_1^*(1385)^{\pm}_{o} \; \rho^{\mp}_{o}$, are presented. Chapter V deals similarly with the reaction $K^- p \to \Lambda \pi^+ \pi^-$. Chapter VI discusses results for masses and widths of $Y_1^*(1385)$ in its various charge states.

II. GATHERING AND REDUCTION OF DATA

A. The Bubble Chamber Exposure

This report is based on data extracted from over one million stereo triads of photographs of a separated K^- beam[1] passing through the Lawrence Radiation Laboratory 72-inch hydrogen bubble chamber. Table I summarizes the characteristics of the beam in its five momentum settings ranging from 2.1 to 2.7 BeV/c.

The following particular circumstances of the exposure have bearing on the subsequent analysis: Correction for chromatic aberration of beam focusing was achieved by means of cocked mass separation slits,[1] which entailed isolation in space of the various momentum components of the beam. This led to a correlation between the precise direction of a beam track in the chamber and its momentum; this correlation was utilized in estimating momenta for individual beam tracks. The occurrence, about halfway through the run, of a short in the bubble chamber magnet coil, occasioned some further study of the magnetic field in the chamber, described in Appendix A.

B. Scanning, Measuring, and Fitting

The entire film sample was scanned once, and a substantial portion scanned twice, with the scanners looking for all interaction topologies of interest. This investigation is based on events classified according to topology as type 32 (see Figure 1): an incoming beam track yields two oppositely charged visible tracks, and a neutral which is seen to decay into two oppositely charged visible tracks (a vee). A vee is recorded only if it points back toward the primary vertex and is not an obvious electron-positron pair.

Table I. Characteristics of K^- beam momentum settings.

K^- path length (events/millibarn)[a]	Central K^- momentum (BeV)[b]	Variance of K^- momentum (BeV)[b]	π^- contamination (%)[c]
6660 ± 220	2.102 ± .007	0.038	3 ± 1 %
2040 ± 80	2.472 ± .009	0.035	7 ± 4 %
3960 ± 130	2.587 ± .009	0.024	15 ± 4 %
6950 ± 210	2.636 ± .009	0.034	15 ± 4 %
3590 ± 120	2.727 ± .009	0.035	34 ± 8 %

[a] Estimated from number of $K^- \rightarrow 3$ charged particle decays.

[b] Estimated from fitted $K^- \rightarrow \pi^+\pi^-\pi^-$ decays, corrected for magnetic field errors.

[c] Estimated from number of events with two vees and no charged prongs which fit $\pi^- p \rightarrow \Lambda^o K^o$.

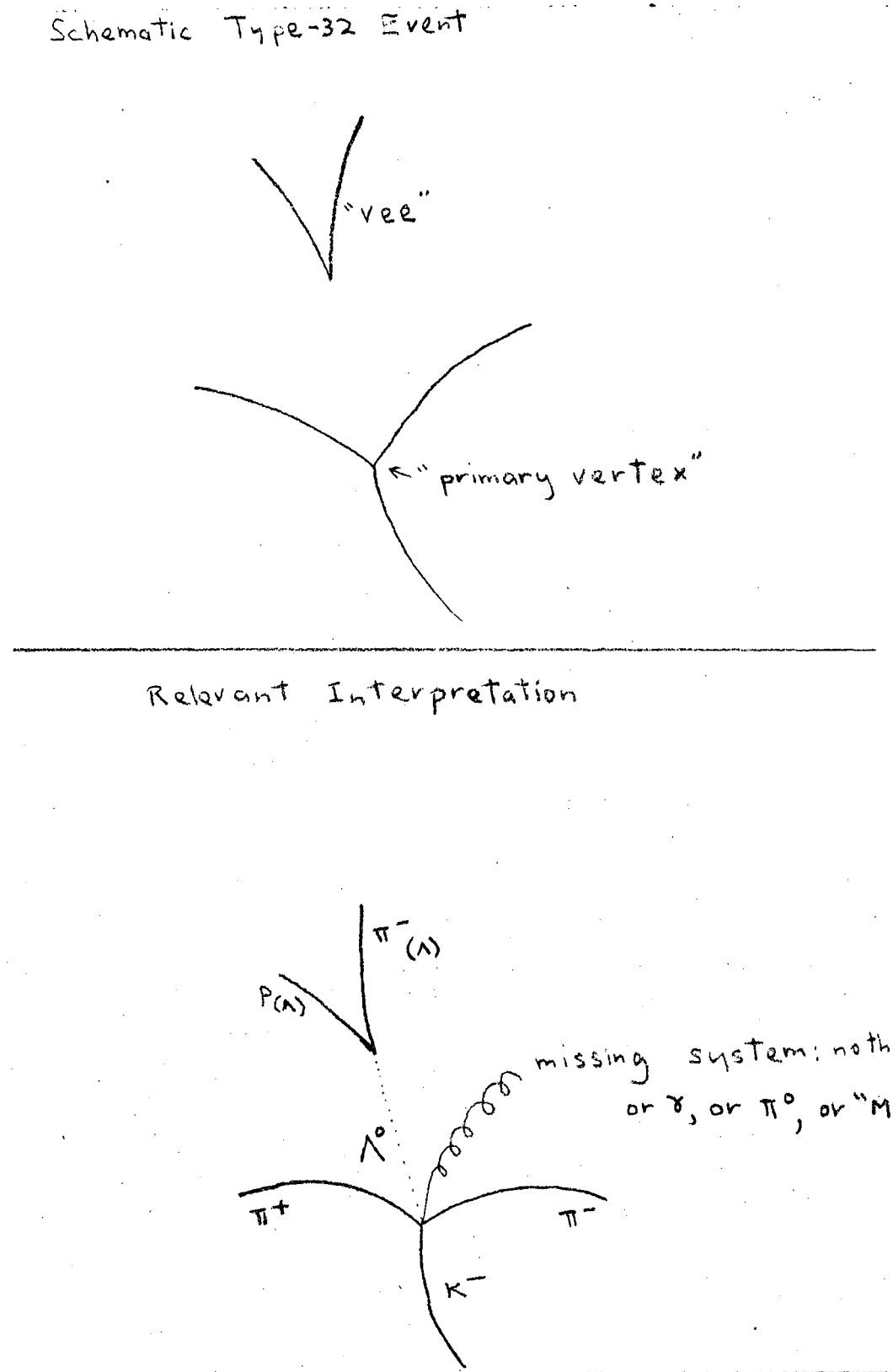

Fig. 1. The type-32 event.

A majority of the type 32 events were measured on the SMP scanning and measuring projectors,[2] while the rest were measured on Franckensteins. The measurements were processed through the computer program PACKAGE.

Measurements of beam tracks are altered before fitting by beam averaging: the curvature used in fitting is a weighted average of the measured curvature, and the average curvature of a class of similar beam tracks.

For each measured type 32 event, fits to some 23 different reaction hypotheses are attempted in PACKAGE. For brevity, we list in Table II only those hypotheses in which the vee is fitted as the decay of a lambda which originates at the primary vertex. These include the reactions of interest in our investigation, $K^- p \rightarrow \Lambda \pi^+ \pi^-$ and $K^- p \rightarrow \Lambda \pi^+ \pi^o \pi^-$, and encompass all serious ambiguities. A confidence level was calculated for each hypothesis, using appropriately adjusted errors. (The confidence level for a fit to a hypothesis is the probability, if the hypothesis were true, of obtaining a worse fit, by the χ^2 criterion.[19]) Hypotheses with confidence levels less than 0.005 were abandoned. Several hypotheses in general survive: these are said to be ambiguous with each other. The most serious ambiguities, for our purposes, are among the hypotheses in column A. of Table II, and they are dealt with in the following section of this report.

The only serious ambiguity not encompassed in column A. of Table II is the ambiguity between $\Lambda K^+ K^-$ and $\Lambda \pi^+ \pi^o \pi^-$. In the sample of events for which the $\Lambda \pi^+ \pi^o \pi^-$ confidence level is the highest, up to 3/4 $^o/o$ of the events also have a $\Lambda K^+ K^-$ fit. (This at the highest beam momentum;

Table II. Reaction hypothesis involving a Λ^{o} originating at the primary vertex.

Number of constraints	A	B	C
4	$K^{-}p \rightarrow \Lambda\ \pi^{+}\pi^{-}$ (1)	$K^{-}p \rightarrow \Lambda\ K^{+}K^{-}$ (5)	
2	$K^{-}p \rightarrow \Sigma^{o}\pi^{+}\pi^{-}$ (2) $\hookrightarrow \Lambda + \gamma$	$K^{-}p \rightarrow \Sigma^{o}K^{+}K^{-}$ (6) $\hookrightarrow \Lambda + \gamma$	
1	$K^{-}p \rightarrow \Lambda\ \pi^{+}\pi^{-}\pi^{o}$ (3)	$K^{-}p \rightarrow \Lambda\ K^{+}K^{-}\pi^{o}$ (7)	$K^{-}p \rightarrow \Lambda K^{+}\pi^{-}K^{o}$ (8) $K^{-}p \rightarrow \Lambda\pi^{+}K^{-}K^{o}$ (9)
0	$K^{-}p \rightarrow \Lambda\pi^{+}\pi^{-}MM^{a}$ (4)		

[a] $K^{-}p \rightarrow \Lambda\ \pi^{+}\pi^{-}$ MM includes $K^{-}p \rightarrow \Sigma^{o}\pi^{+}\pi^{-}\pi^{o}$ ($\hookrightarrow \Lambda + \gamma$) and $K^{-}p \rightarrow \Lambda\pi^{+}\pi^{-} + n\pi^{o}$ ($n \geq 2$).

at lower beam momenta the effect is smaller.) This ambiguity is tolerated with no further resolution, with the proviso that the enhancement in the $\pi^+\pi^o\pi^-$ mass spectrum in the region of the $\varphi(1020)$ must be interpreted with care.[3]

C. Resolution of Serious Ambiguities

We will use as the basic data for further resolving serious ambiguities the measured (not fitted) quantities $M^2_{\Lambda^+ \text{ miss}}$, M^2_{miss}, and E_{miss}, which are calculated from measured momenta in the laboratory system as follows (see Fig. 1 for labelling of tracks):

$$P_{\text{miss}} = P_{K^-} + P_{\text{target}} - (P_{\pi^+} + P_{\pi^-} + P_{P(\Lambda)} + P_{\pi^-(\Lambda)}), \quad \text{(4-vectors)}$$

$$M^2_{\text{miss}} = P^2_{\text{miss}},$$

$$M^2_{\Lambda^+ \text{ miss}} = (P_{P(\Lambda)} + P_{\pi^-(\Lambda)} + P_{\text{miss}})^2.$$

Procedures important in establishing the accuracy of this unfitted data are discussed in Appendix A.

Distributions of $M^2_{\Lambda^+ \text{ miss}}$, M^2_{miss}, and E_{miss} are shown in Figures 2, 3, and 4, illustrating the nature and extent of the serious ambiguities. The division of the data into samples (1), (2), (3), and (4) anticipates the conclusions of this analysis, and the ordering of the samples is such that the serious ambiguities are between adjacent samples.

Separation of $\Lambda\pi^+\pi^-$ from $\Sigma^o\pi^+\pi^-$

The details of this separation are summarized in Figure 5. For a complete and pure sample of $\Lambda\pi^+\pi^-$ events, the distribution of $M^2_{\Lambda + \text{ miss}}$ (Fig. 5(a)) should be reasonably symmetrical[4] about the mass of the lambda

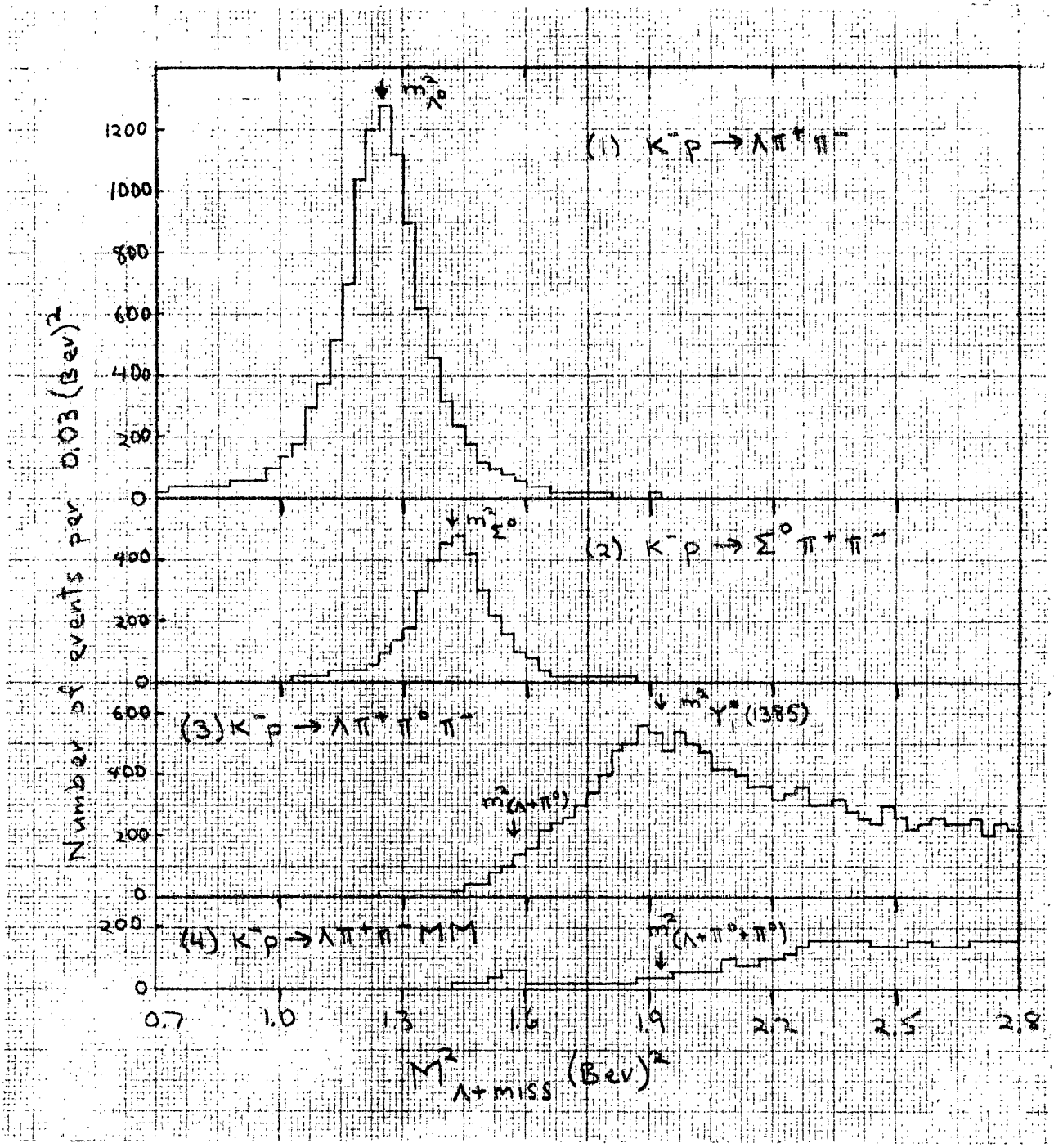

Fig. 2. Distributions of $M^2_{\Lambda+\text{ miss}}$, the invariant mass squared (unfitted) of the system consisting of the lambda and any unseen neutrals (for final data samples (1), (2), (3), and (4)).

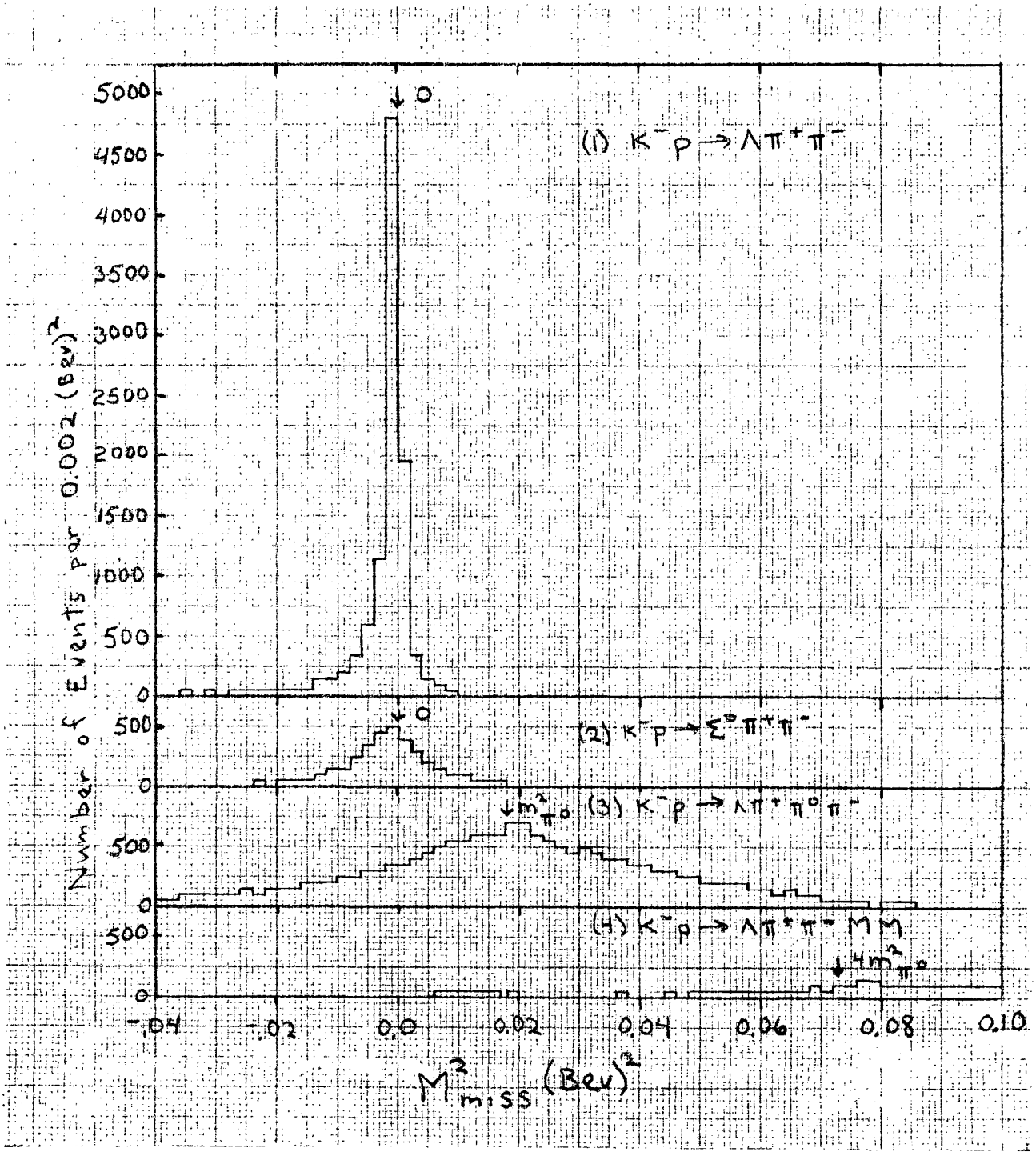

Fig. 3. Distributions of M^2_{miss}, the invariant mass squared (unfitted) of the system consisting of any unseen neutrals (for final data samples (1), (2), (3), and (4)).

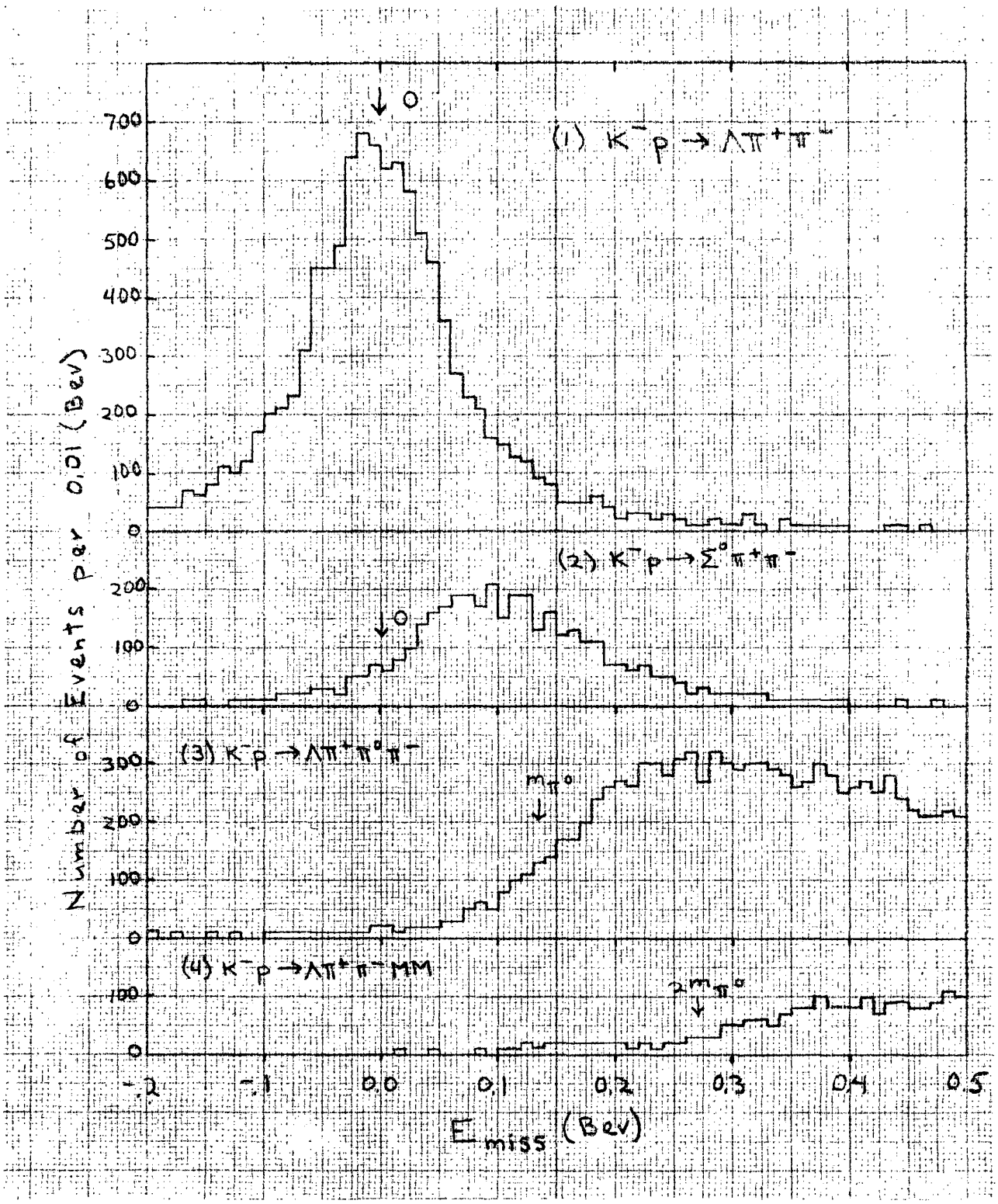

Fig. 4. Distributions of E_{miss}, the laboratory energy (unfitted) of the system consisting of any unseen neutrals (for final data samples (1), (2), (3), and (4)).

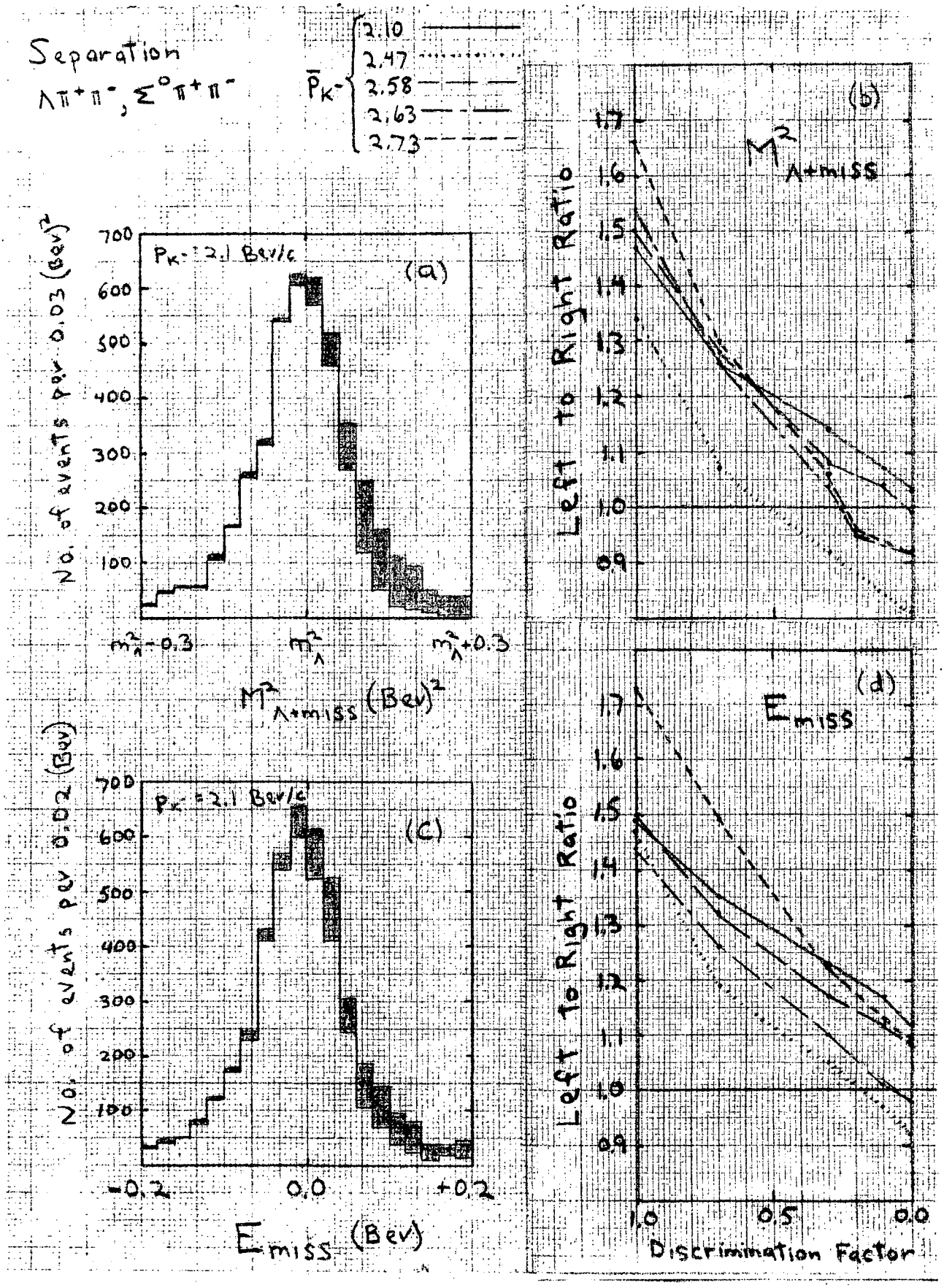

Fig. 5. Unshaded histograms (a) and (c) represent a sample of $\Lambda\pi^+\pi^-$ chosen on the basis of best confidence level. Different separation criteria are suggested by graphs (b) and (d) (see text), adding the shaded portions of (a) and (c) to the $\Lambda\pi^+\pi^-$ sample.

squared, while E_{miss} (Fig. 5(c)) should be reasonably symmetrical about zero. (M^2_{miss} is not useful in this separation, as it is not an unbiased estimator of the mass of the missing system when there is in fact no missing system.[4])

The unshaded histograms in Figures 5(a) and 5(c) represent samples of $\Lambda\pi^+\pi^-$ naively chosen on the basis of best confidence level. It can be seen that the high side of each peak is depleted. As events in these regions are lost primarily through having a better fit for $\Sigma^0\pi^+\pi^-$, we seek to improve the situation by discriminating against the $\Sigma^0\pi^+\pi^-$ hypothesis; we multiply the confidence level for the $\Sigma^0\pi^+\pi^-$ hypothesis by a "discrimination factor" less than one before comparing with the $\Lambda\pi^+\pi^-$ confidence level.

We vary this discrimination factor from one down to zero, in order to find the value which yields the most symmetric distributions in $M^2_{\Lambda + miss}$ and E_{miss}. As a convenient index of the symmetry of the distributions, we use the ratio of the number of events left of the proper center to the number right of the center. The separation criterion which gives 1.0 for this ratio is taken as the correct one. This procedure has been carried out independently at each of the five beam momentum settings, so that any systematic differences would be manifest. The left-to-right ratios are plotted as functions of discrimination factor in Figures 5(b) and 5(d).

The results at the various momenta, and for both the $M^2_{\Lambda + miss}$ and E_{miss} distributions, are consistent within expected errors (Appendix A), so we average the ten curves in Figures 5(b) and 5(d). An average left-to-right ratio of 1.0 is obtained for a discrimination factor of

almost exactly 0.0, which means that all events which have a good fit to the $\Lambda\pi^+\pi^-$ hypothesis are to be interpreted as true $\Lambda\pi^+\pi^-$ events, regardless of how well they fit $\Sigma^0\pi^+\pi^-$. This resolution of the ambiguity adds the shaded events in Figures 5(a) and 5(c) to the $\Lambda\pi^+\pi^-$ sample. This analysis yields an estimated error of ± 5 °/o on the total number of events in the resultant $\Lambda\pi^+\pi^-$ sample.

Separation of $\Sigma^0\pi^+\pi^-$ from $\Lambda\pi^+\pi^0\pi^-$

The remaining $\Sigma^0\pi^+\pi^-$ fits are seriously ambiguous only with $\Lambda\pi^+\pi^0\pi^-$, and the above procedure may be repeated, mutatis mutandis. The appropriate discrimination factor turns out to be 0.5. (See Figure 6). Errors on this separation will be discussed below.

Separation of $\Lambda\pi^+\pi^0\pi^-$ from $\Lambda\pi^+\pi^-$MM

This separation, illustrated in Figure 7, differs from the previous ones in that no straightforward confidence level is available for the missing mass hypothesis. We proceed by plotting the distribution of M^2_{miss} for all good $\Lambda\pi^+\pi^0\pi^-$ fits remaining after the previous separation. The data points with error bars are the results of a bin by bin subtraction of the left-hand side of the π^0 peak from the right-hand side, constituting a rough estimate of the contamination of the sample.[4] By eliminating the events with M^2_{miss} greater than $4M^2_{\pi^0}$, we lose a small portion of the real $\Lambda\pi^+\pi^0\pi^-$ events, but we also eliminate essentially all of the contamination from $\Lambda\pi^+\pi^-n\pi^0$, $n \geq 2$. The contamination in the remaining sample is presumably mainly from $\Sigma^0\pi^+\pi^0\pi^-$, where the missing system consists of a π^0 plus a gamma ray from the Σ^0 decay. We have found no way of distinguishing

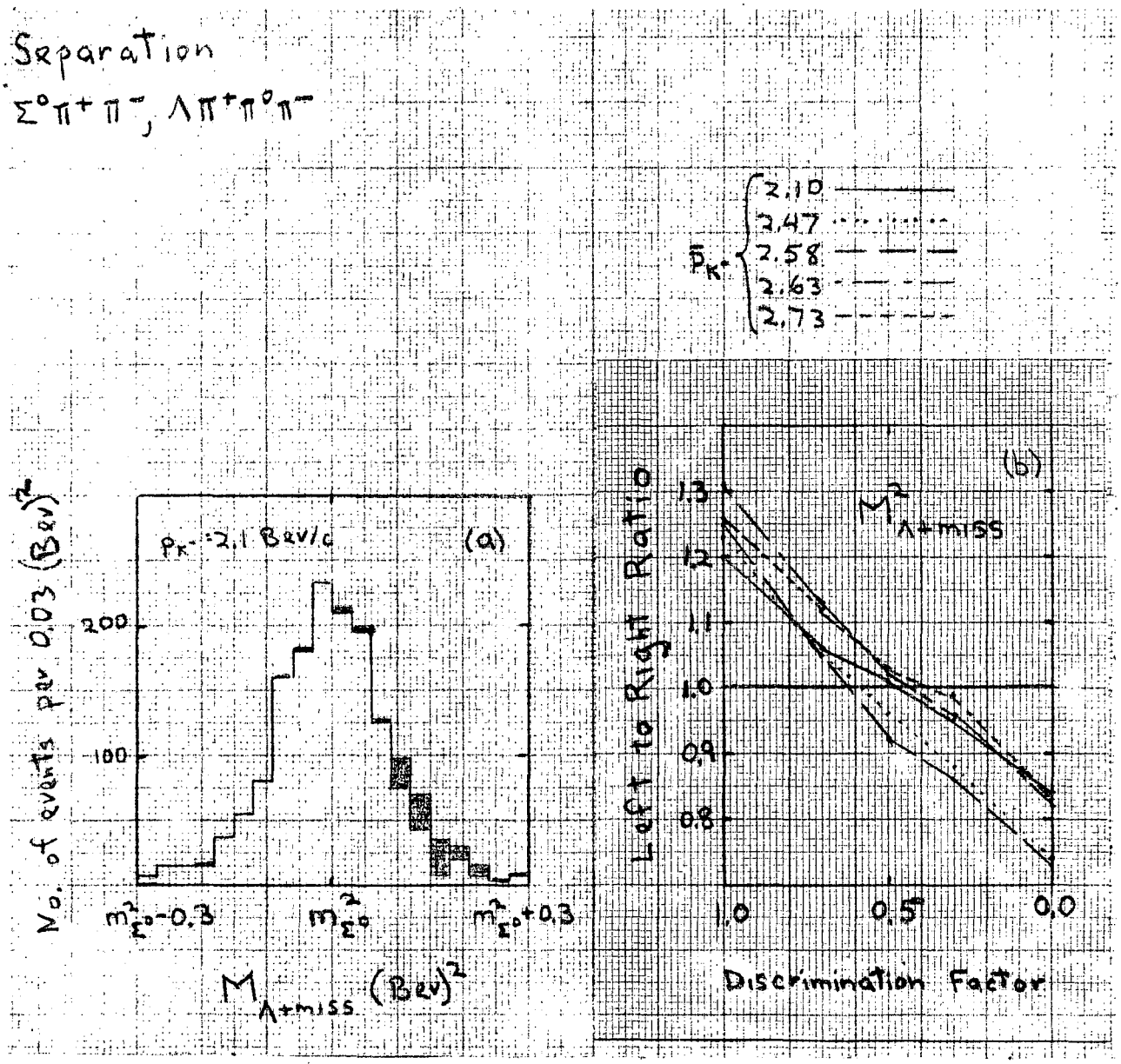

Fig. 6. The unshaded histogram (a) represents a preliminary sample of $\Sigma^0\pi^+\pi^-$. Final separation criteria are chosen according to graph (b) (see text), adding the shaded portions of (a) to the $\Sigma^0\pi^+\pi^-$ sample.

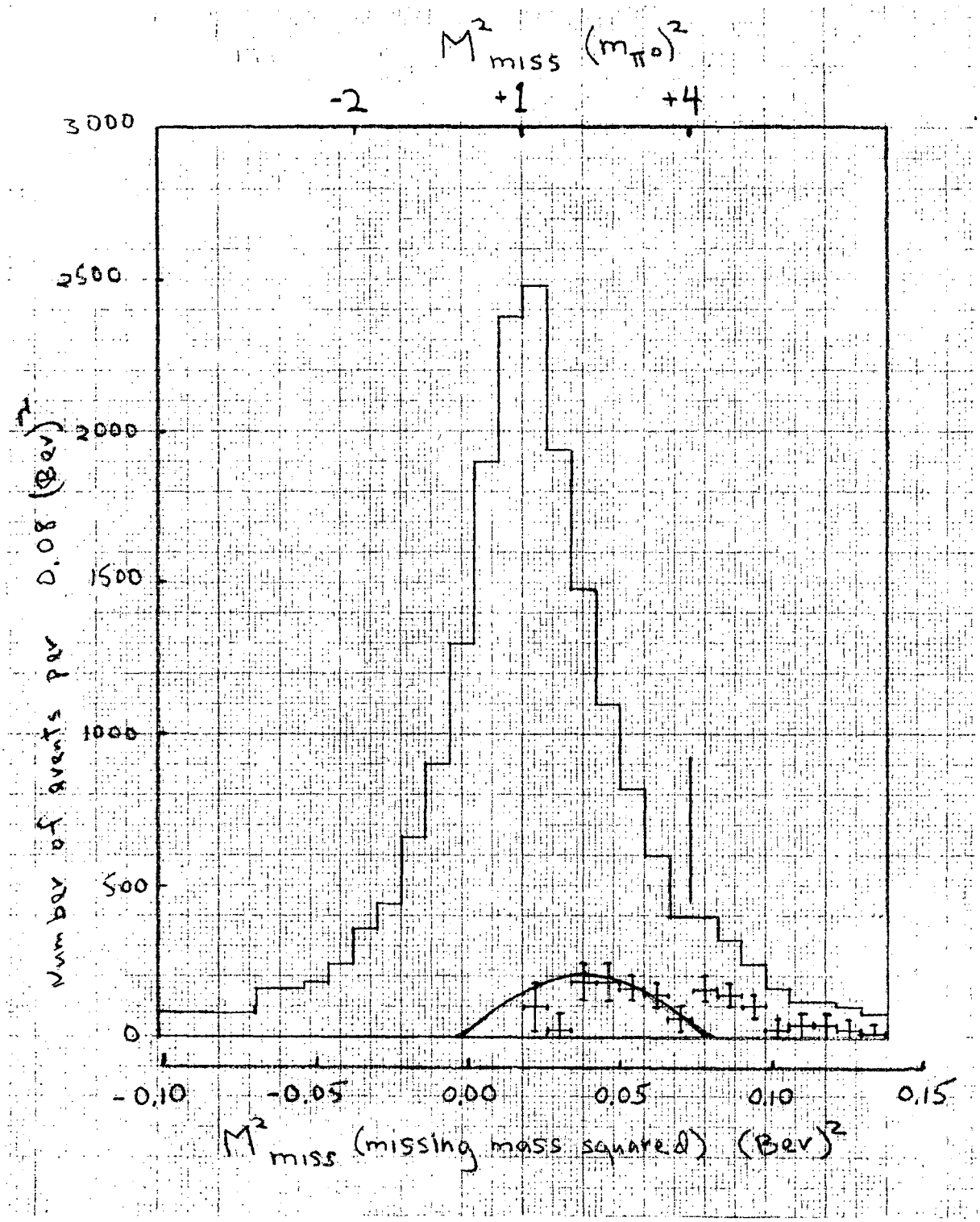

Fig. 7. Histogram of M^2_{miss} for preliminary sample of $\Lambda\pi^+\pi^0\pi^-$. The data points with error bars at the bottom measure the asymmetry of the peak, providing an index of contamination (see text).

this contamination from real $\Lambda\pi^+\pi^o\pi^-$, so it remains in the sample.

The amount of residual contamination ranges from 1 ± 3 o/o at 2.1 BeV/c up to 6 ± 2 o/o at the upper momenta, and is determined in the following manner: The smooth curve toward the bottom of Figure 7 has the shape of the expected distribution of M^2_{miss} for $\Sigma^o\pi^+\pi^o\pi^-$ events which fit $\Lambda\pi^+\pi^o\pi^-$.[5] This curve is normalized to the subtracted data points in the region $2m^2_{\pi^o} \leq M^2_{miss} \leq 4m^2_{\pi^o}$, and is then taken to represent the true number of contaminating events. The probable systematic error in this method of estimating the contamination is taken as approximately 25 o/o, and this is added in quadrature to the statistical errors to yield the quoted errors.

Other Checks

A qualitative check on this whole separation procedure can be obtained by a glance back at Figures 2, 3, and 4, which summarize the results of all separations made in terms of all the variables used. Nothing untoward is observed.

A more quantitative check is obtained by looking at the decay of the supposed Σ^o in the $\Sigma^o\pi^+\pi^-$ sample. The decay of the Σ^o should be isotropic in its own rest frame, where we use the following coordinate system; $\hat{x} = \hat{P}_{K^-}$; $\hat{z} = \widehat{P_{K^-} \times P_{\text{target proton}}}$; $\hat{y} = \hat{z} \times \hat{x}$. The distributions of the direction cosines of the decay γ rays from all Σ^o's in the final separated $\Sigma^o\pi^+\pi^-$ sample are found in Figures 8(g), 8(h), and 8(i), where they are seen to be reasonably flat.

The other histograms in Figure 8 show the distributions expected from possible contaminants in the $\Sigma^o\pi^+\pi^-$ sample. Figures 8(a),

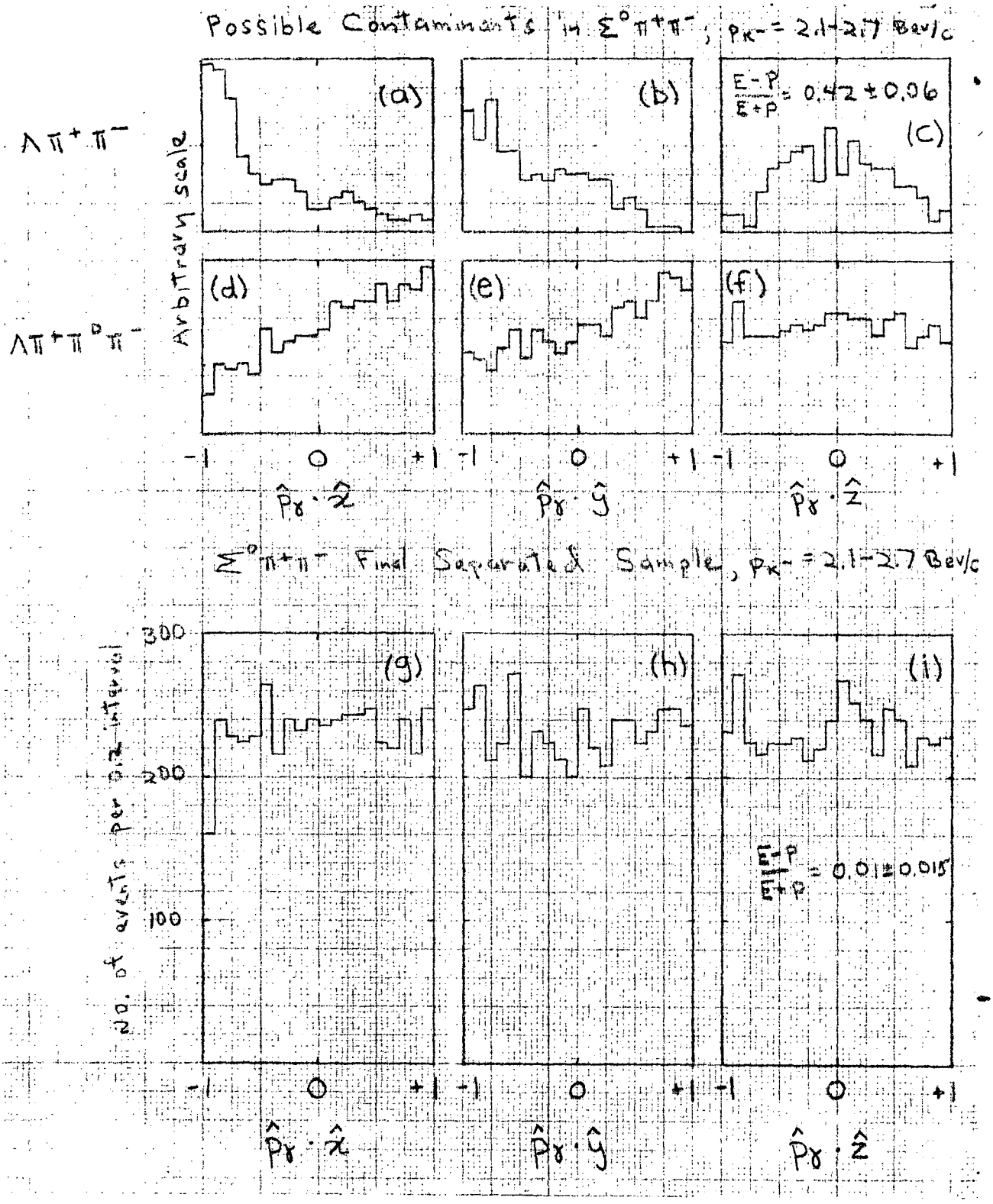

Fig. 8. (g), (h), and (i) are distributions of direction cosines for the decay of Σ° in the $\Sigma^\circ\pi^+\pi^-$ sample. (a), (b), (c), and (d), (e), (f), are the same distributions for possible contaminants in the $\Sigma^\circ\pi^+\pi^-$ sample (all distributions in the supposed Σ° rest frame).

8(b), and 8(c) display events which have been chosen as $\Lambda\pi^+\pi^-$ by the preceding separation, but which also have a good fit to $\Sigma^0\pi^+\pi^-$. (Data from fits of these events to the $\Sigma^0\pi^+\pi^-$ hypothesis is used.) Figures 8(d), 8(e), and 8(f) contain events whichhave been chosen as $\Sigma^0\pi^+\pi^-$, but also fit $\Lambda\pi^+\pi^0\pi^-$ well.

Little information can be gleaned from the $\hat{\gamma}\cdot\hat{x}$ and $\hat{\gamma}\cdot\hat{y}$ distributions, as the contaminations from $\Lambda\pi^+\pi^-$ and $\Lambda\pi^+\pi^0\pi^-$ have opposite effects which would tend to cancel each other. In looking at $\hat{\gamma}\cdot\hat{z}$ however, we find that the $\Lambda\pi^+\pi^-\pi^0$ contaminating component is essentially flat, while the $\Lambda\pi^+\pi^-$ contaminating component is strongly clustered about $\hat{\gamma}\cdot\hat{z}=0$. Polar-equatorial ratios for the $\hat{\gamma}\cdot\hat{z}$ distributions are calculated for the sample of supposed $\Sigma^0\pi^+\pi^-$, and for the $\Lambda\pi^+\pi^-$ contaminating component. The conclusion is that the number of $\Lambda\pi^+\pi^-$ lost to $\Sigma\pi^+\pi^-$ in this fashion amounts to $2\frac{1}{2} \pm 4$ °/o of the $\Lambda\pi^+\pi^-$ final state. Propagated through to the separation of $\Sigma^0\pi^+\pi^-$ from $\Lambda\pi^+\pi^-\pi^0$, this error indicates an error of $1 \pm 1\frac{1}{2}$ °/o of the $\Lambda\pi^+\pi^-\pi^0$ final state.

D. Ingredients of Cross Section Calculations

Our calculations of cross sections proceed directly from scan information:

$$\sigma_R = \frac{\text{Number of type-R reactions in scan volume}}{\text{Total } K^- \text{ path length in scan volume}}$$

Results for the denominator of this expression have already been presented in Table I; numerators pertaining to the reactions $K^-p \to \Lambda\pi^+\pi^-$ and $K^-p \to \Lambda\pi^+\pi^0\pi^-$ are calculated, respectively, from the ingredients listed in Tables III and IV. The first entry in each table is the number

Table III. $K^- p \rightarrow \Lambda \pi^+ \pi^-$ cross section ingredients.

Cross section ingredients	$\bar{P}_{k^-}$ = 2.1 (BeV/c)	Error (%)	$\bar{P}_{k^-}$=2.47 (BeV/c)	Error (%)	$\bar{P}_{k^-}$ = 2.6 (BeV/c)	Error (%)
32's found on scan no. 1	30331	½ %	9256	1 %	64830	½ %
Effective scan efficiency	0.976	3½	0.976	3½	0.976	3½
π contamination	0.997	0	0.994	0	0.980	½
Fraction fitting $\Lambda\pi^+\pi^-$	0.225	2	0.160	3	0.139	1½
Neutral decay	1.5		1.5		1.5	
Short length and escape vee loss	1.07	1	1.10	1	1.085	1
Separation contamination and loss	1.01	3	1.01	3	1.01	3
Resultant $\sigma_{\Lambda\pi^+\pi^-}$	1.62 mb	7	1.17 mb	8	0.98mb	7

Table IV. $K^- p \rightarrow \Lambda\pi^+\pi^o\pi^-$ cross section ingredients.

Cross section ingredients	$\overline{P}_{K^-}$ = 2.1 (BeV/c)	Error (%)	$\overline{P}_{K^-}$ = 2.47 (BeV/c)	Error (%)	$\overline{P}_{K^-}$ = 2.6 (BeV/c)	Error (%)
32's found on scan no.1	30331	½ %	9256	1 %	64830	½ %
Effective scan efficiency	0.976	3½	0.976	3½	0.976	3½
π contamination	0.997	0	0.994	0	0.980	½
Fraction fitting $\Lambda\pi^+\pi^o\pi^-$	0.331	1	0.331	2	0.302	1
Neutral decay	1.5		1.5		1.5	
Short length and escape vee loss	1.05	1	1.06	1	1.07	1
Contamination:[a] $\Lambda\pi^+\pi^-\pi^o\pi^o$	0.99	1	0.96	1	0.96	1
Contamination:[b] $\Sigma^o\pi^+\pi^o\pi^-$	0.99	3	0.95	4	0.94	2
Resultant $\sigma_{\Lambda\pi^+\pi^o\pi^-}$	2.26 mb	7	2.11 mb	8	1.86 mb	7

a. Essentially none of this $\Lambda\pi^+\pi^-\pi^o\pi^o$ contamination is present in the sample used for analysis.

b. Essentially all of this $\Sigma^o\pi^+\pi^o\pi^-$ contamination remains in the sample used for analysis.

of events found on the first scan, of the topology with two prongs and a vee. The error on this quantity is just the statistical counting error, the square root of the number.

The subsequent entries in Tables III and IV are the factors by which the first scan results must be multiplied in order to estimate the true frequency of the particular reaction in question. The scanning efficiency was determined by looking for conflicts between the first and second scans for a portion of the film, and examining the events in question on the scan table. The conclusion was that more events which were not "real 32's" (events where the vee was an electron-positron pair, etc.) were inserted than real 32's were missed. Thus we must multiply by a number less than one, 0.976, with an error which is mainly statistical on the samples used for this study.

The π-induced contribution to the 32's is estimated from the π contamination in the beam (Table I) and the known cross sections at these beam energies for $\pi^- p$ yielding a two prong plus vee topology.[21] The errors on these small corrections are negligible.

The next factor is the fraction of 32's which fit the $\Lambda\pi^+\pi^-(\pi^0)$ hypothesis. This should really be the fraction of events which would fit the hypothesis if all events had been fitted. In reality, about 80 °/o of the 32's have been successfully fitted, so that an extrapolation must be made for the remaining 20 °/o. Using the fraction determined from the events which did have a successful fit is not legitimate, as those events which did not fit will have a higher concentration of relatively difficult-to-fit reactions. It was indeed found that events which passed on the second measurement, after having failed once, had significantly different

fractions of the various hypotheses. However, third and fourth measurements were not significantly different from second measurements with respect to the hypotheses in question, so the fraction estimated for the whole sample was composed of a weighted average of the fractions for first measurements and for second or greater measurements. The fraction of events which passed on the first measurement (neglecting events which failed because of operator error and such) ranged from 79 °/o at 2.1 BeV/c to 70 °/o at the upper momenta, so that at 2.1 BeV/c, for instance, we have

$$\left(\frac{\#\ \Lambda\pi^+\pi^-(\pi^o)}{\#\ \text{ET } 32}\right)_{\text{final}} = 0.79\left(\frac{\#\ \Lambda\pi^+\pi^-(\pi^o)}{\#\ \text{ET } 32}\right)_{\substack{\text{passing}\\ \text{1st meas.}}} + 0.21\left(\frac{\#\ \Lambda\pi^+\pi^-(\pi^o)}{\#\ \text{ET } 32}\right)_{\substack{\text{passing}\\ \text{2nd}\\ \text{meas.}}}$$

As the extrapolation involved is small, the errors on the result are mainly statistical.

The next number is the correction for the events which are not seen as 32's because the lambda decays by the neutral mode, $\Lambda \rightarrow n\pi^o$. This number is taken to be exactly 1.5, consistent both with experiment and the $\Delta I = \frac{1}{2}$ rule for weak decays. The next correction, for short length scanning losses of lambda decays, as well as escape losses, was made on the basis of the weights assigned to the events (see Appendix B). Thus,

$$\frac{\text{real number of } \Lambda\pi^+\pi^-(\pi^o)}{\text{number found}} =$$

$$\frac{\text{real number of } \Lambda\pi^+\pi^-(\pi^o)}{\text{number retained after cutoffs}} \times \frac{\text{number retained after cutoffs}}{\text{number found}}$$

= average weight x retention fraction.

Typical average weights were around 1.18, indicating a moderate extrapolation; typical retention fractions were around 0.90, indicating

moderate loss of statistics; and the resultant products then ran around 1.06, as in the Table. The error reflects the error in weighting due to error in momentum measurement, as well as a small statistical error.

The next entries in the Table correct for separation errors. Our separation procedure indicates that we wind up with no $\Lambda\pi^+\pi^-$ lost or gained, (except for those with a confidence level less than $\frac{1}{2}$ %), within $\pm$ 5 %. Our check of the Σ^o decay distribution indicates a loss to the $\Sigma^o\pi^+\pi^-$ sample of ($2\frac{1}{2} \pm 4$) % of the $\Lambda\pi^+\pi^-$ sample, at most. We deduce a correction factor of 1.01 $\pm$ 0.03 to the number of $\Lambda\pi^+\pi^-$. When this correction is propagated through the separation procedure, it yields a negligible correction to the number of $\Lambda\pi^+\pi^o\pi^-$, and carries an error contribution of $\pm$ $1\frac{1}{2}$ %.

There are two more entries in the $\Lambda\pi^+\pi^o\pi^-$ table to account for the two sources of residual contamination in the sample. (The sample used here for estimating true numbers of events differs from the sample used for subsequent analysis, in that events with $M^2_{miss} > 4M^2_{\pi o}$ have here not been cut out, in order that we may estimate the contamination explicitly.) The contamination due to $K^-p \rightarrow \Lambda\pi^+\pi^- + n\pi^o$, $n \geq 2$, essentially all of which has $M^2_{miss} \geq 4M^2_{\pi o}$, is estimated from the excess of events with $M^2_{miss} \geq 4M^2_{\pi o}$ over the number expected from symmetry of the M^2_{miss} distribution about $M^2_{\pi o}$. The error is statistical. The contamination due to $\Sigma^o\pi^+\pi^o\pi^-$ has been dealt with above.

The products of all of these factors, divided by the relevant K^- path lengths, yield the cross sections in the bottom rows of the Tables. The errors quoted here are the root mean squares of the percentage errors in the various factors, to which has been added just under two percent, to

cover the circumstance of our not being able to check in a completely convincing way the efficiency of the book-keeping system which kept track of the several hundred thousand events in this experiment through all their vicissitudes.

III. MAXIMUM LIKELIHOOD FITTING METHOD

A. Finding Amounts, Masses, and Widths of Resonances

In both $K^- p \to \Lambda \pi^+ \pi^0 \pi^-$ and $K^- p \to \Lambda \pi^+ \pi^-$, the reaction proceeds through several intermediate states involving one or two (in the four-body state) resonances. Parameters corresponding to amounts of the various resonant processes, as well as the masses and widths of the resonances, are all highly correlated. It thus becomes desirable to solve for many of these parameters simultaneously; this is quite feasible because of the large number of events we have. A useful vehicle for such a project is a maximum likelihood fit to a comprehensive model.

The Model and the Likelihood[6]

We proceed from the following general definition of the likelihood function:[7]

$$\mathcal{L}(\alpha) = \prod_{i=1}^{N} f(\alpha; x_i)$$

The likelihood function, $\mathcal{L}(\alpha)$, (where α represents the set of parameters for which we want to get best estimates) is the joint probability density of getting a particular experimental result, $x_1, \ldots, x_N$, assuming that $f(\alpha; x)$ is the true normalized distribution function:

$$\int f(\alpha; x)\, dx = 1$$

In our particular case, the experimental result consists of a set of events, so that the index i runs over all the N events in the experiment, and x_i is the set of variables characterizing the final state of the i-th event. Therefore we may factor

$$f(\alpha; x) = |M(\alpha; x)|^2 \rho(x),$$

where M (α; x) is the transition matrix element to the final state x, depending on the parameters α, and ρ (x) is the phase space factor appropriate to the final state and the variables x.

We make the simplifying assumption that M is the resultant of a set of non-interfering transition processes characterized by M_j, j=1 to N_p, so that

$$|M(\alpha;x)|^2 = \sum_{j=1}^{N_p} \alpha_j |M_j(\alpha_j';x)|^2$$

We demand that $\int |M_j|^2 \rho\, dx = 1$ so that α_j may be interpreted as the amount of the j-th process, and we insure over-all normalization by setting $\alpha_{N_p} = 1 - \sum_{j=1}^{N_p-1} \alpha_j$ so that

$$\int f(\alpha;x)\, dx = \int |M|^2 \rho\, dx$$

$$= \int \sum_{j=1}^{N_p} \alpha_j |M_j|^2 \rho\, dx$$

$$= \sum_{j=1}^{N_p} \alpha_j \int |M_j|^2 \rho\, dx$$

$$= \sum_{j=1}^{N_p} \alpha_j = 1.$$

(This model of non-interfering resonant processes appears to yield a reasonable description of our data, except when applied to decay correlations in the presence of large backgrounds.)

For computational ease, we choose to maximize the logarithm of the likelihood. (The position of the maximum is not affected, as the logarithm is a monotonically increasing function.)

$$W(\alpha) \equiv \ln \mathcal{L}(\alpha)$$

$$= \sum_{i=1}^{N} \ln |M(\alpha; x_i)|^2 \rho(x_i)$$

$$= \sum_{i=1}^{N} \ln |M(\alpha; x_i)|^2 + \sum_{i=1}^{N} \ln \rho(x_i)$$

The second sum over events is not a function of the parameters , so we can just leave it out, and redefine

$$W(\alpha) \equiv \sum_{i=1}^{N} \ln |M(\alpha; x_i)|^2 .$$

For our specific model, we specify the further convention that $|M_{N_p}|^2 = 1$, that the last process in the list will be phase space. We then have, more explicitly,

$$W(\alpha) = \sum_{i=1}^{N} \ln \left[\sum_{j=1}^{N_p - 1} \alpha_j |M_j(\alpha'_j; x_i)|^2 + \left(1 - \sum_{j=1}^{N_p - 1} \alpha_j\right) \right],$$

where

$\alpha \equiv \{\alpha_j, \alpha'_j\}$;

α, the set of parameters being fitted, consists of the $N_p - 1$ amounts α_j, along with any variable parameters in the matrix elements α'_j.

The Forms of the Matrix Elements M_j

A matrix element M_j was taken to be a single resonance line shape, for the production of one resonance in a process, or a product of two resonance line shapes, specifically for the process $K^- p \to Y_1^*$ (1385) ρ (750). For copiously produced resonances known to be p-wave, form R_1 was used:[8]

$$R_1 \propto \frac{m_o \frac{\Gamma}{(p/m)}}{(m_o^2 - m^2)^2 + (m_o\Gamma)^2} \quad ; \quad \Gamma = \Gamma_o \left(\frac{p}{p_o}\right)^3 \frac{1 + \frac{p_o}{0.279}}{1 + \frac{p}{0.279}}$$

where m_o, Γ_o, and p_o are respectively the central mass, width, and decay momentum of the resonance, and Γ and p depend on the variable m. For less copiously produced resonances with appreciable real width, a simple Breit-Wigner shape is used:

$$R_2 \propto \frac{m_o \Gamma_o}{(m_o^2 - m^2) + (m_o \Gamma_o)^2}$$

For the ω and η resonances, where the real width is small compared to the experimental resolution, we use a gaussian line shape, R_3.

Fitting Program: Solutions, Errors

The program used in searching the space of parameters for the maximum of the likelihood is called FIT[9]. FIT assumes that the logarithm of the likelihood has a quadratic shape, which should be true in the neighborhood of the maximum; FIT then steps directly from its starting value to the point where it thinks the maximum should be. This procedure is especially apt for our situation, where we have a large number of events--good statistics. The rapid stepping towards a solution is necessary because we have large numbers of events to process; the procedure is feasible because the good statistics insure that the likelihood will be reasonably smooth and regular. A further

saving in computer time is effected by the use of an approximation (described in Appendix C) for second derivatives of the log of the likelihood.

FIT decides that it is at a maximum essentially when it finds all first derivatives to be small. (The test is actually done on a χ^2 function which is closely related to a sum of first derivatives.) The "answer" then includes, for our purposes, solutions and errors for the parameters, and a correlation matrix. Let us examine a hypothetical fit to two parameters to illustrate the significance of the answers which we get from the fit.

In Figure 9, the parameter space illustrated is the plane of the parameters x and y. Let (x_o, y_o) represent the point in the plane for which the likelihood is a maximum, so that the coordinates of that point, x_o and y_o, are the solutions for the parameters x and y. The errors δ_x and δ_y then define a rectangle, which circumscribes an ellipse, representing the locus of points at which the log of the likelihood is down from the maximum by $\frac{1}{2}$. These errors take into account correlations.

The correlation matrix for this solution would be

$$\begin{array}{c} \\ x \\ y \end{array} \begin{array}{c} \begin{array}{cc} x & y \end{array} \\ \begin{pmatrix} 1 & -C \\ -C & 1 \end{pmatrix} \end{array}$$

where C has the following definition (as illustrated in Figure 9): if one variable is moved one standard deviation from the solution, then the maximum in the other variable will be displaced a fraction of a standard deviation C in a direction indicated by the sign of C.

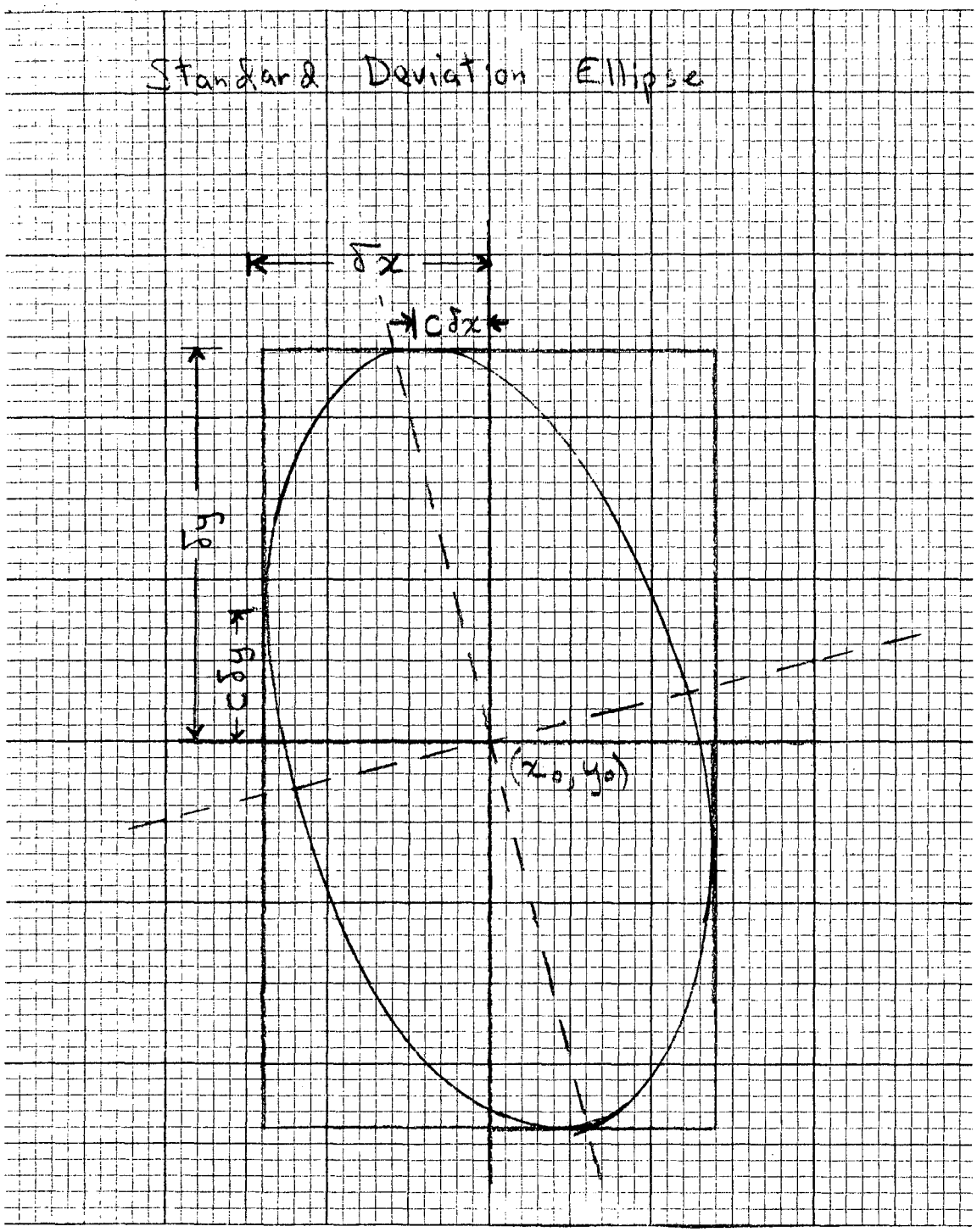

Fig. 9. Standard deviation ellipse, illustrating nature of errors quoted for maximum likelihood fits.

B. Fitting for Production Angular Distributions

Our method for measuring production angular distributions involves no further parameterization; we proceed rather by fitting amounts of resonant processes to subsamples of the data. To find the total amount of a given resonance produced in a given production angular interval, we choose a subsample of the events by imposing this production angle cut on the system of the decay products of the resonance. We then do a maximum likelihood fit, as described above, to determine the fraction of the subsample which proceeds by the resonant process in question. Multiplying this fraction by the number of events in the subsample then gives the number of resonant events in the angular interval. This procedure is possible because a production angle cut involves only the orientation of the final state with respect to the initial state, and does not fix any relationship among the final state particles themselves; the final state phase space which appears in the model is thus not altered.

C. Decay Angular Distributions

In order to facilitate the study of peripheral production mechanisms, we analyze decays of resonances in their own rest frames, using the relevant t-channel coordinate systems,[10] which emphasize the exchanged system. (This choice of coordinate system is illustrated for a particular case in Figure 9.1.) Decays of p-wave resonances are incorporated into the model by multiplying the squares of the matrix elements M_j^2 by a factor D for each decay, of the form

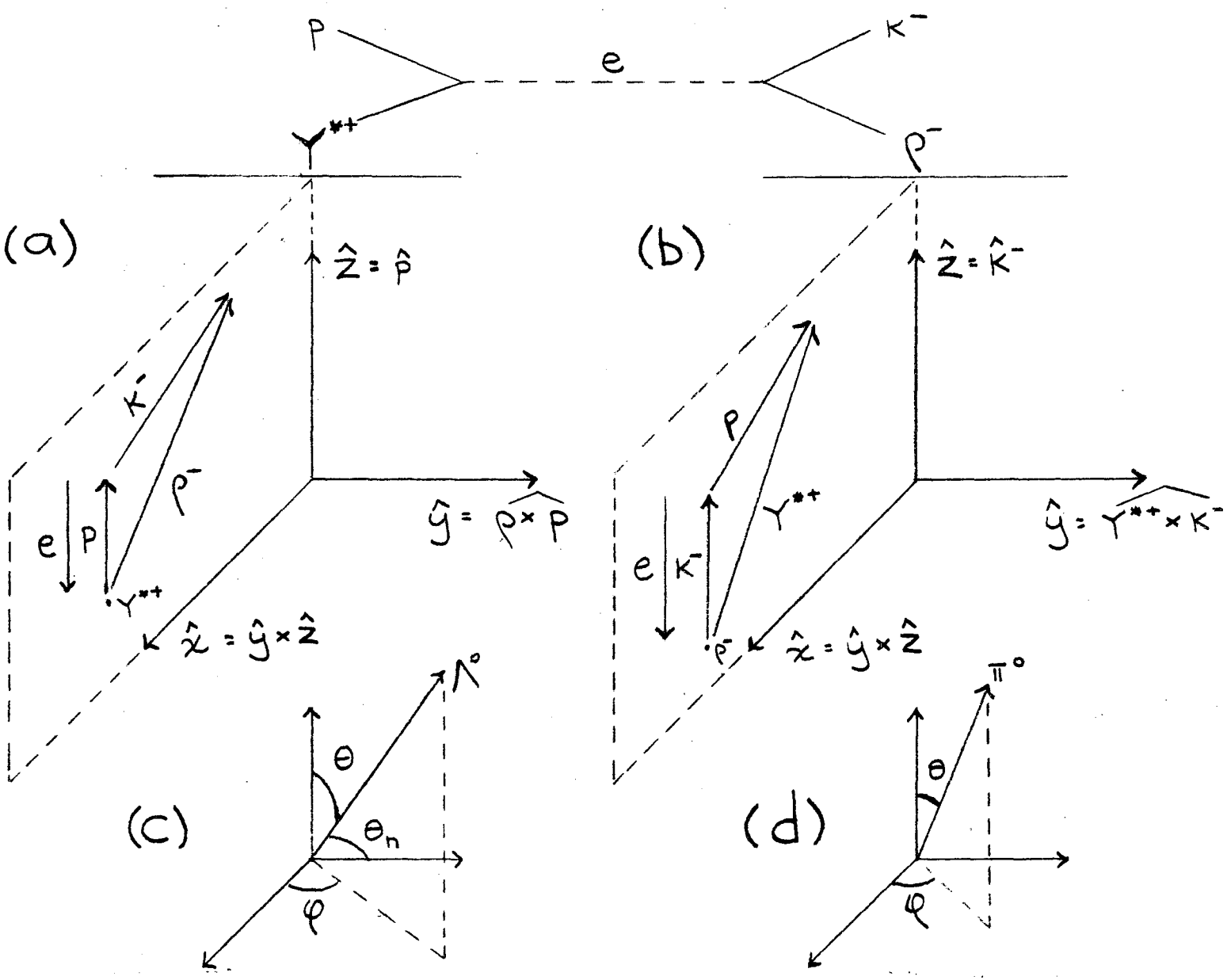

Fig. 9.1. Examples of t-channel coordinate systems. (a) and (b) illustrate the definition of the coordinate axes; (c) and (d) define the decay angles.

$$D = \sqrt{4\pi}\left(\frac{1}{\sqrt{4\pi}} + a Y_2^0(\theta,\varphi) + b\, \mathrm{Re}\, Y_2^1(\theta,\varphi) + c\, \mathrm{Re}\, Y_2^2(\theta,\varphi)\right)$$

The parameters a, b, and c then completely describe the parity conserving decay of a p-wave resonance, and the orthogonality of the spherical harmonics makes this an especially useful parameteriziation for the fit. These parameters are related to density matrix elements as follows:

$Y^*(\frac{3}{2}^+)$	$\rho(1^-)$
$\rho_{33} = \frac{1-\sqrt{5}\,a}{4}$	$\rho_{00} = \frac{1+\sqrt{5}\,a}{4}$
$\mathrm{Re}\,\rho_{31} = \frac{\sqrt{22.5}}{12} b$	$\mathrm{Re}\,\rho_{10} = \frac{\sqrt{15}}{12} b$
$\mathrm{Re}\,\rho_{3,-1} = -\frac{\sqrt{10}}{8} c$	$\rho_{1,-1} = -\frac{\sqrt{30}}{12} c$

IV. RESONANCE PRODUCTION IN $K^- p \to \Lambda\pi^+\pi^0\pi^-$

In this chapter we describe the application of the fitting procedures outlined in Chapter III to the $K^- p \to \Lambda\pi^+\pi^0\pi^-$ data sample.

A. The $K^- p \to \Lambda\pi^+\pi^0\pi^-$ Data Sample

The distribution of K^- beam momentum for the entire sample of 19,000 $K^- p \to \Lambda\pi^+\pi^0\pi^-$ events is shown in Figure 10; also shown is the choice of three subsamples, characterized respectively by average beam momenta of 2.1, 2.47, and 2.6 BeV/c. The $K^- p \to \Lambda\pi^+\pi^0\pi^-$ total cross section has been evaluated for these three beam-momentum samples, and these cross sections are presented, as a function of beam momentum, in Figure 11(a), along with the results of other experiments in this general region of K^- beam momentum. The trend of the cross section may be characterized as a rise from threshold followed by a gradual fall, and the slight scatter of points about this trend in the region of this experiment does not appear to indicate any strong influence of resonances in the s channel.

The dominant features of the $\Lambda\pi^+\pi^0\pi^-$ final state can be seen in the histograms and scatter plots of effective masses presented in Figures 12 through 21. It appears that the following resonant processes must be considered:

$$K^- p \to Y_1^*(1385)^+ \rho^- \qquad (1)$$

$$Y_1^*(1385)^0 \rho^0 \qquad (2)$$

$$Y_1^*(1385)^- \rho^+ \qquad (3)$$

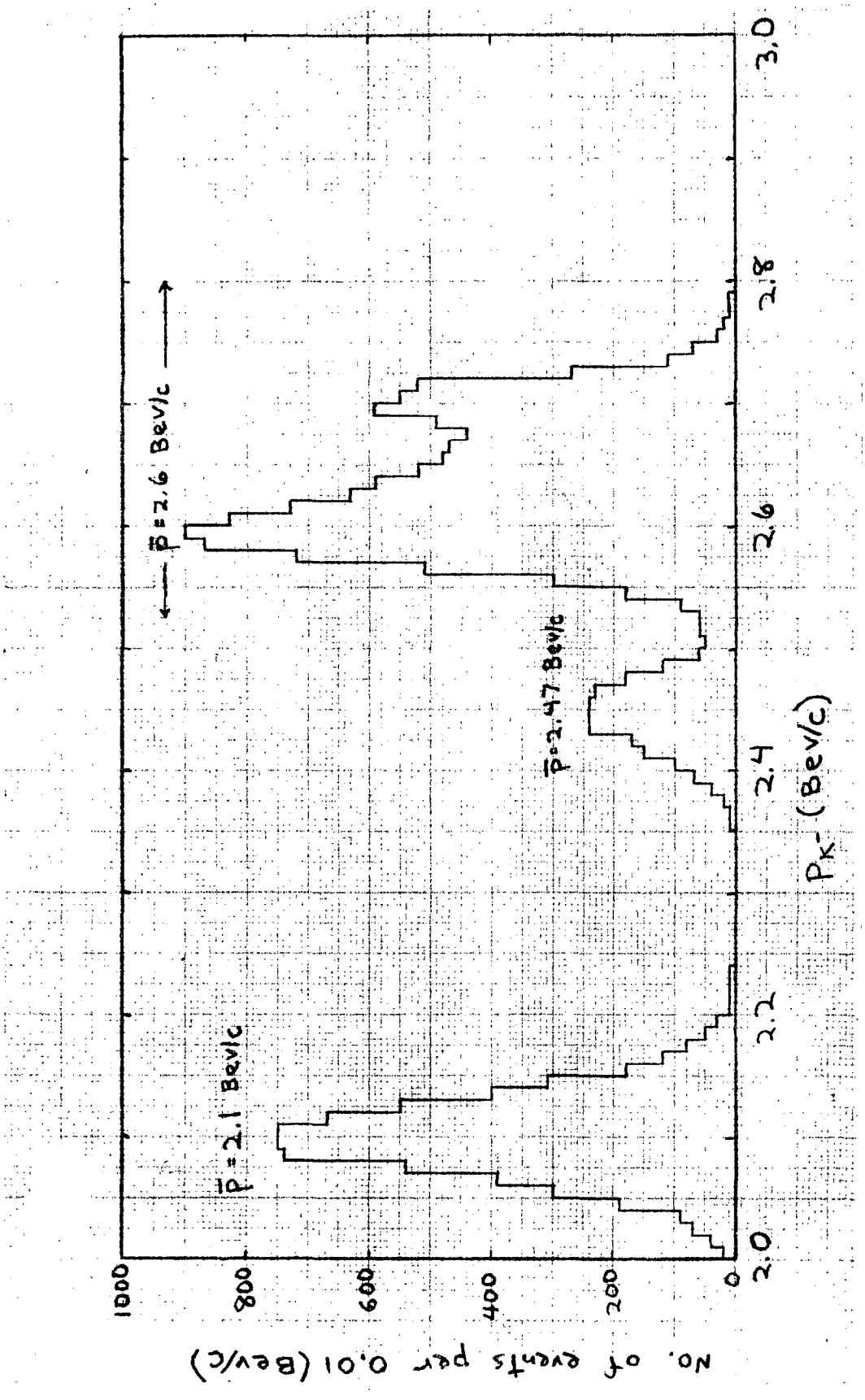

Fig. 10. Distribution of fitted beam momentum for $K^- p \rightarrow \Lambda \pi^+ \pi^0 \pi^-$ events.

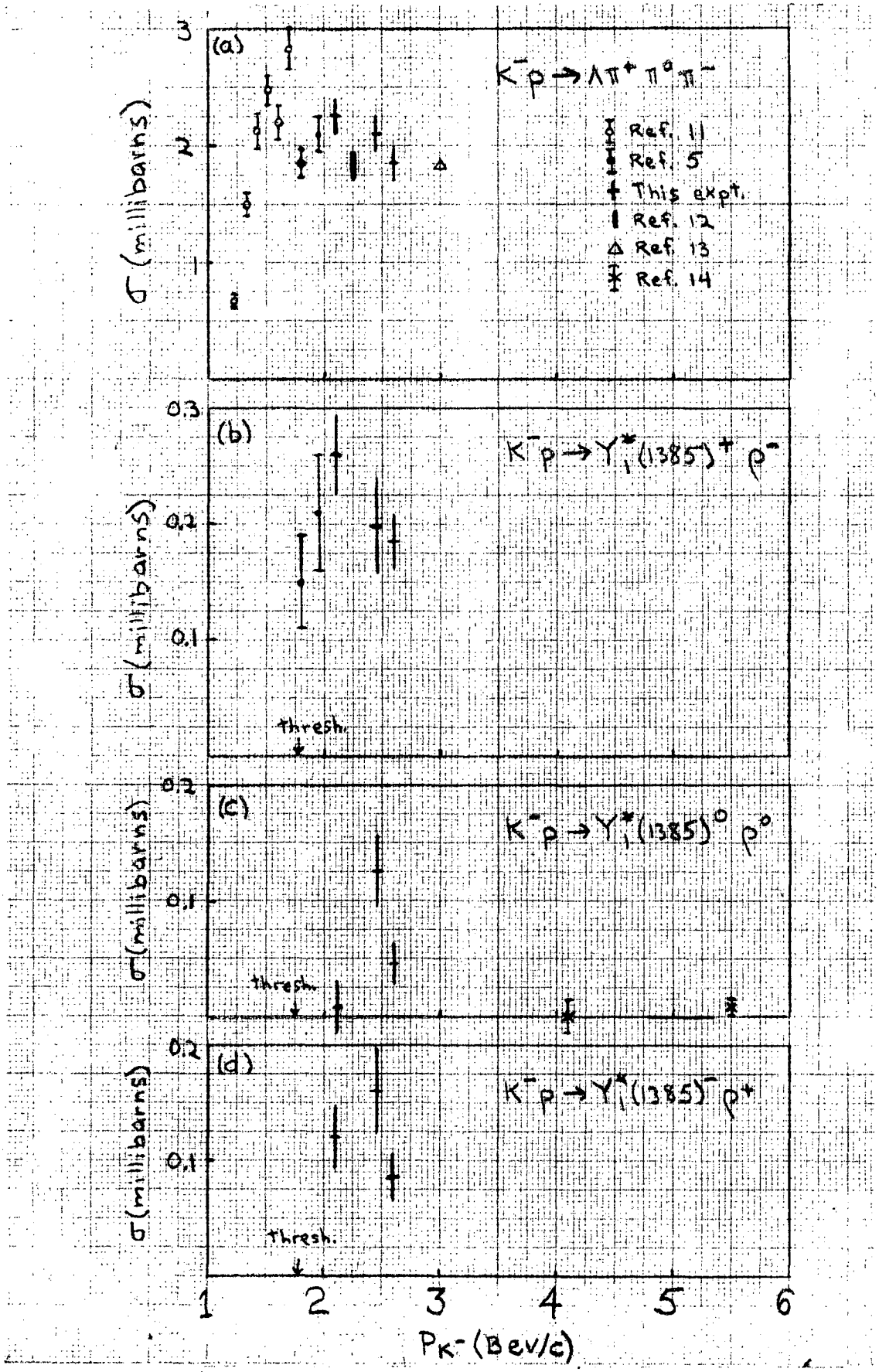

Fig. 11. Total cross sections as a function of incident beam momentum. for the $\Lambda\pi^+\pi^0\pi^-$ final state, and for contributing $Y^*\rho$ reactions.

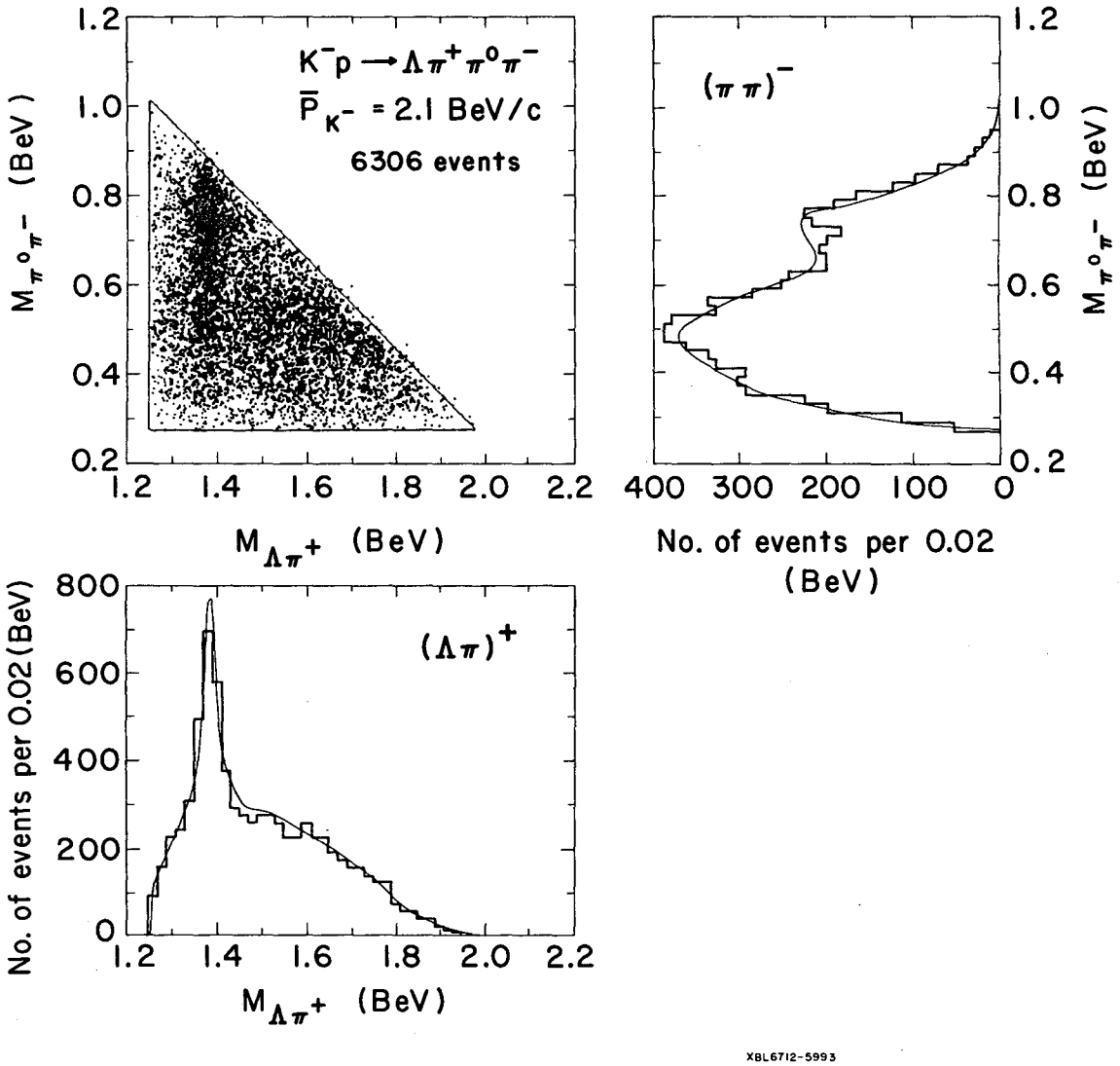

Fig. 12. Invariant mass distributions at 2.1 Bev/c (Part I). The smooth curves represent Monte Carlo calculations.

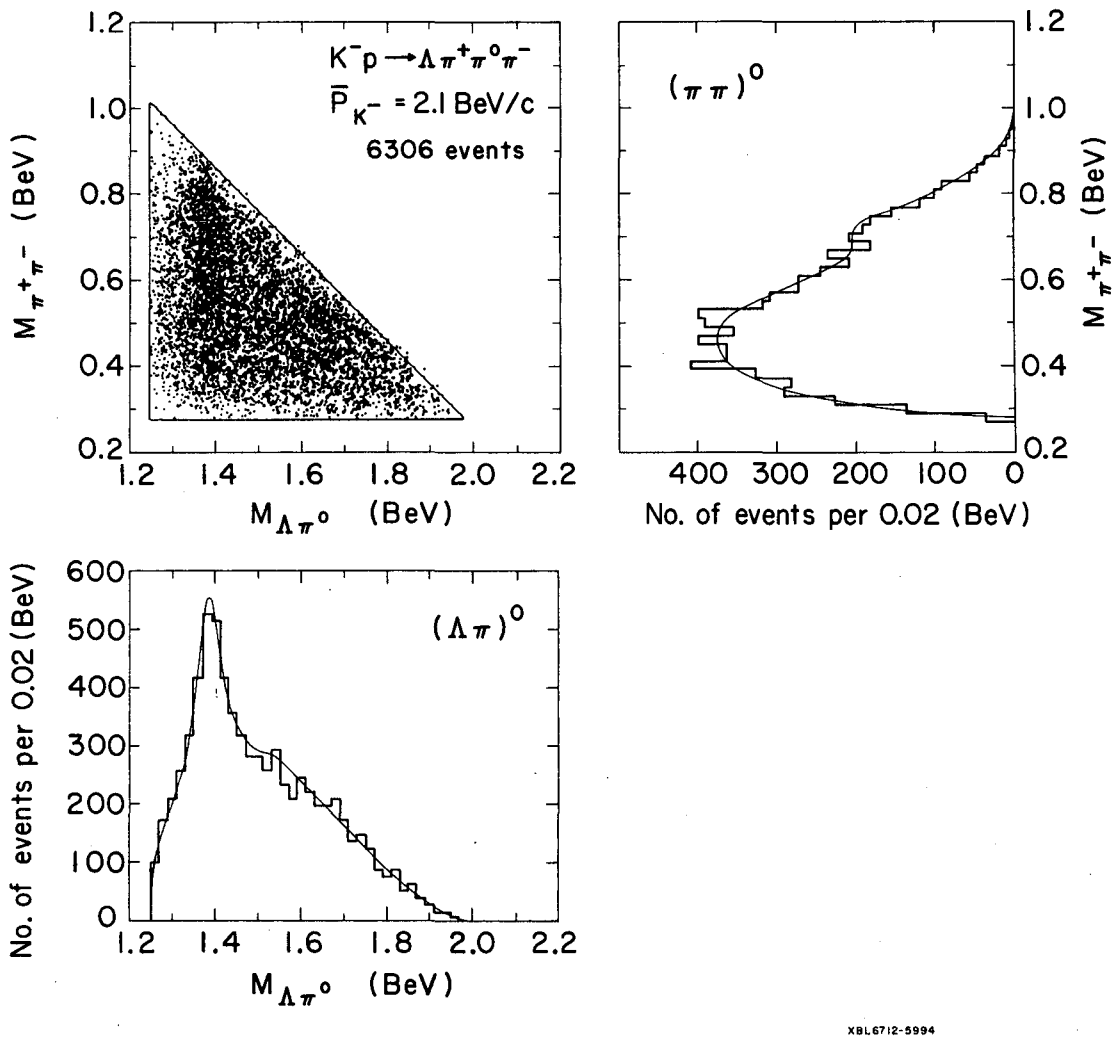

Fig. 13. Invariant mass distributions at 2.1 Bev/c (Part II). The smooth curves represent Monte Carlo calculations.

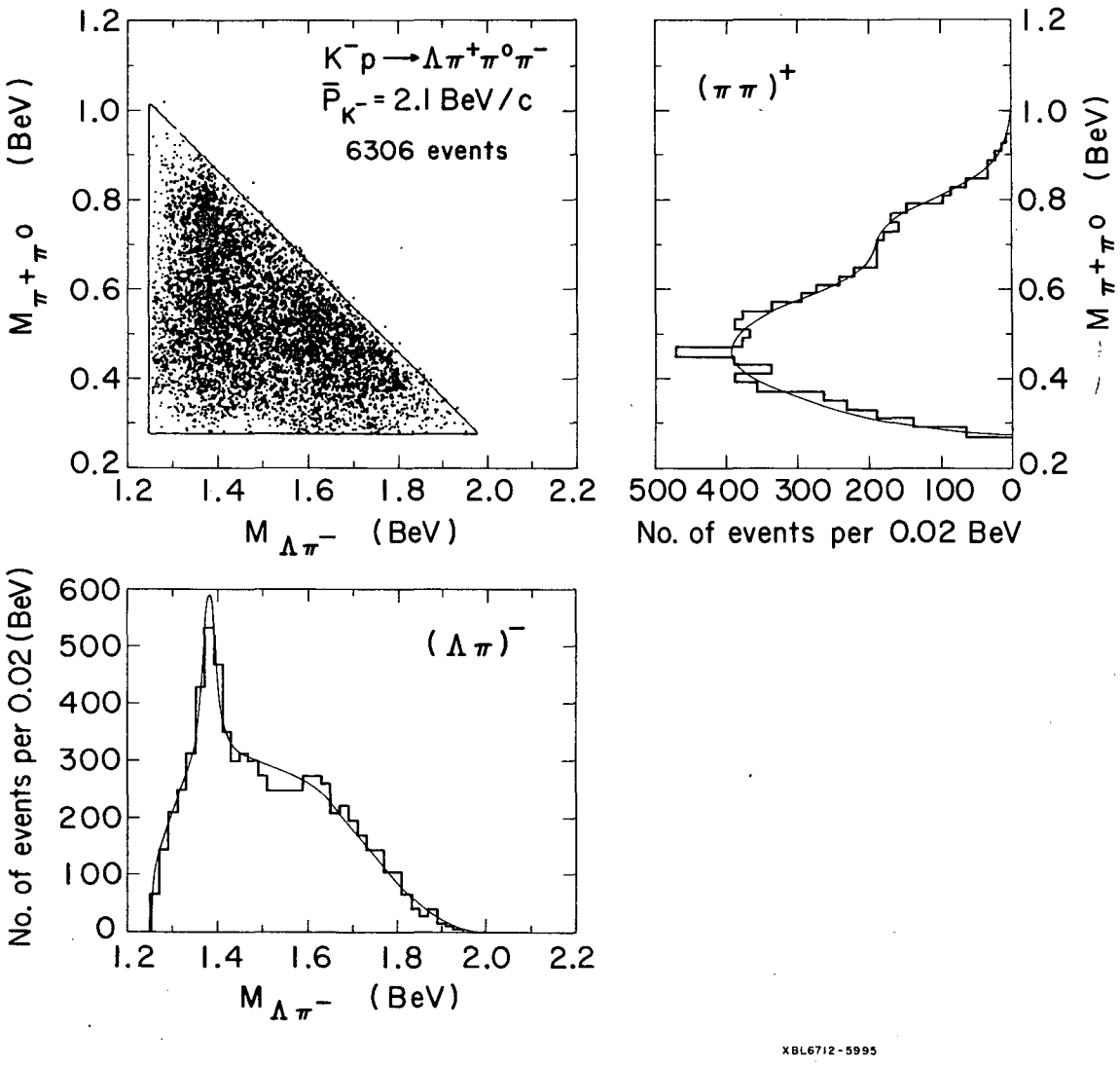

Fig. 14. Invariant mass distributions at 2.1 Bev/c (Part III). The smooth curves represent Monte Carlo calculations.

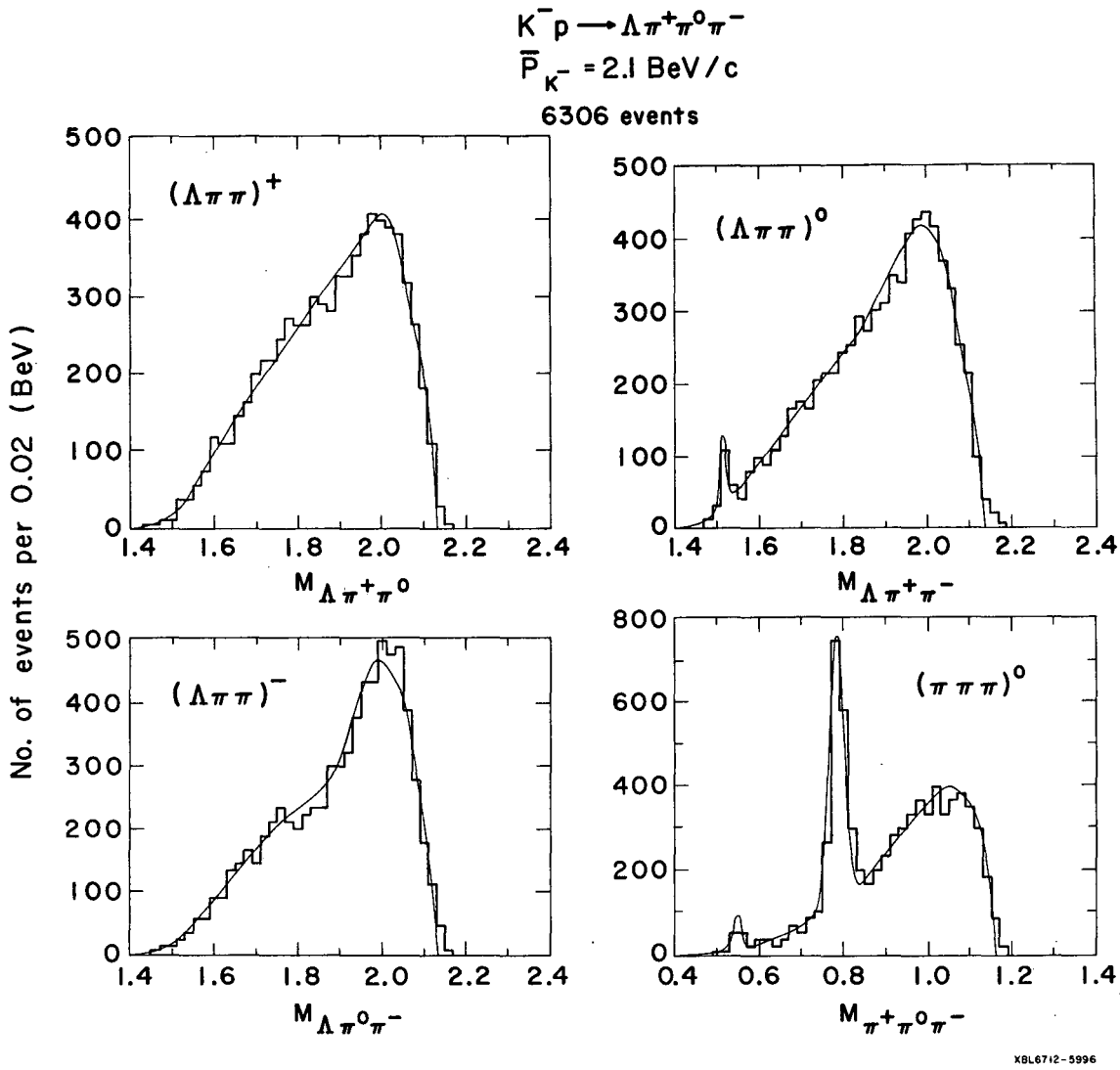

Fig. 15. Invariant mass distributions at 2.1 Bev/c (Part IV). The smooth curves represent Monte Carlo calculations.

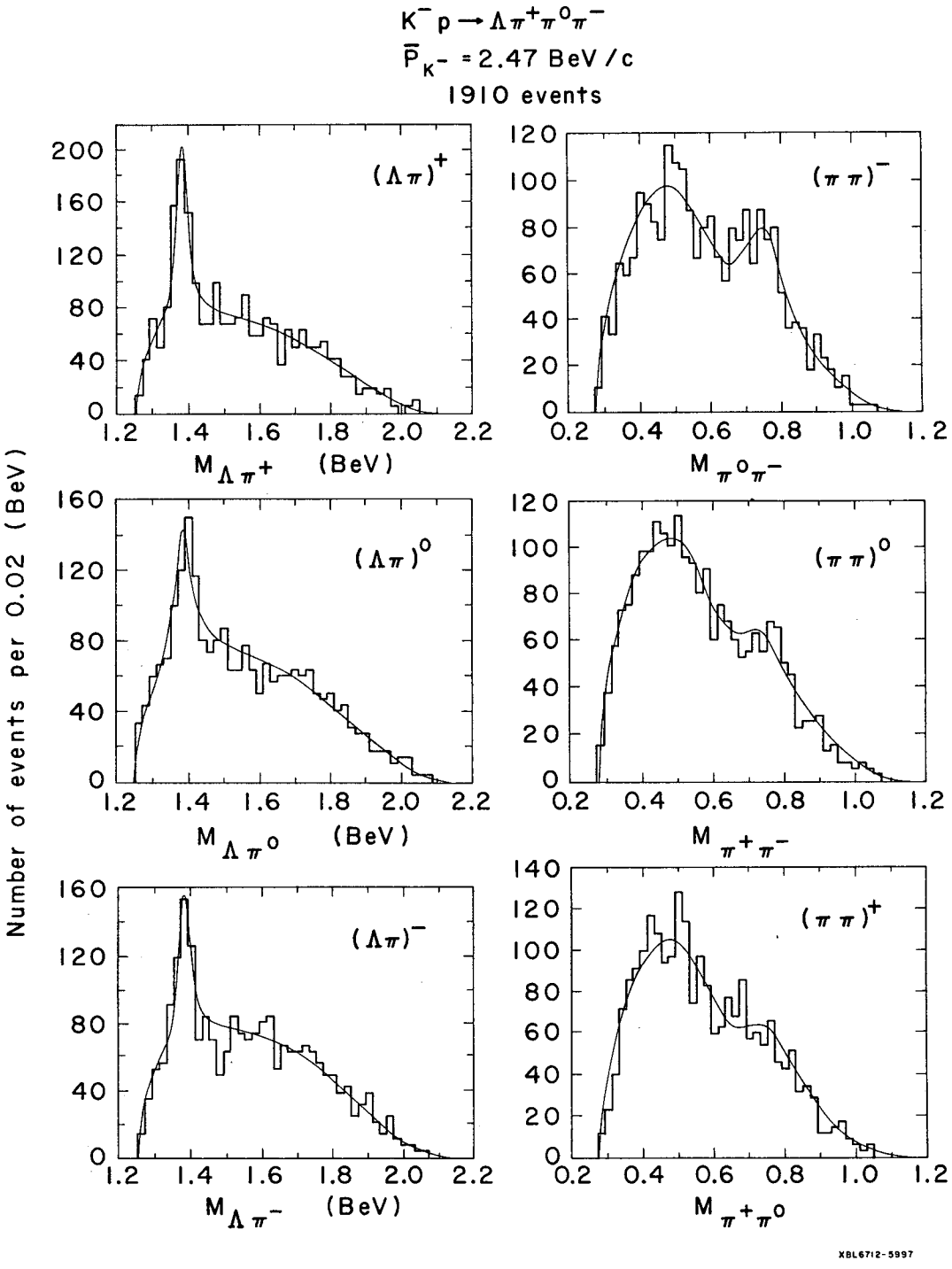

Fig. 16. Invariant mass distributions at 2.47 Bev/c (Part I). The smooth curves represent Monte Carlo calculations.

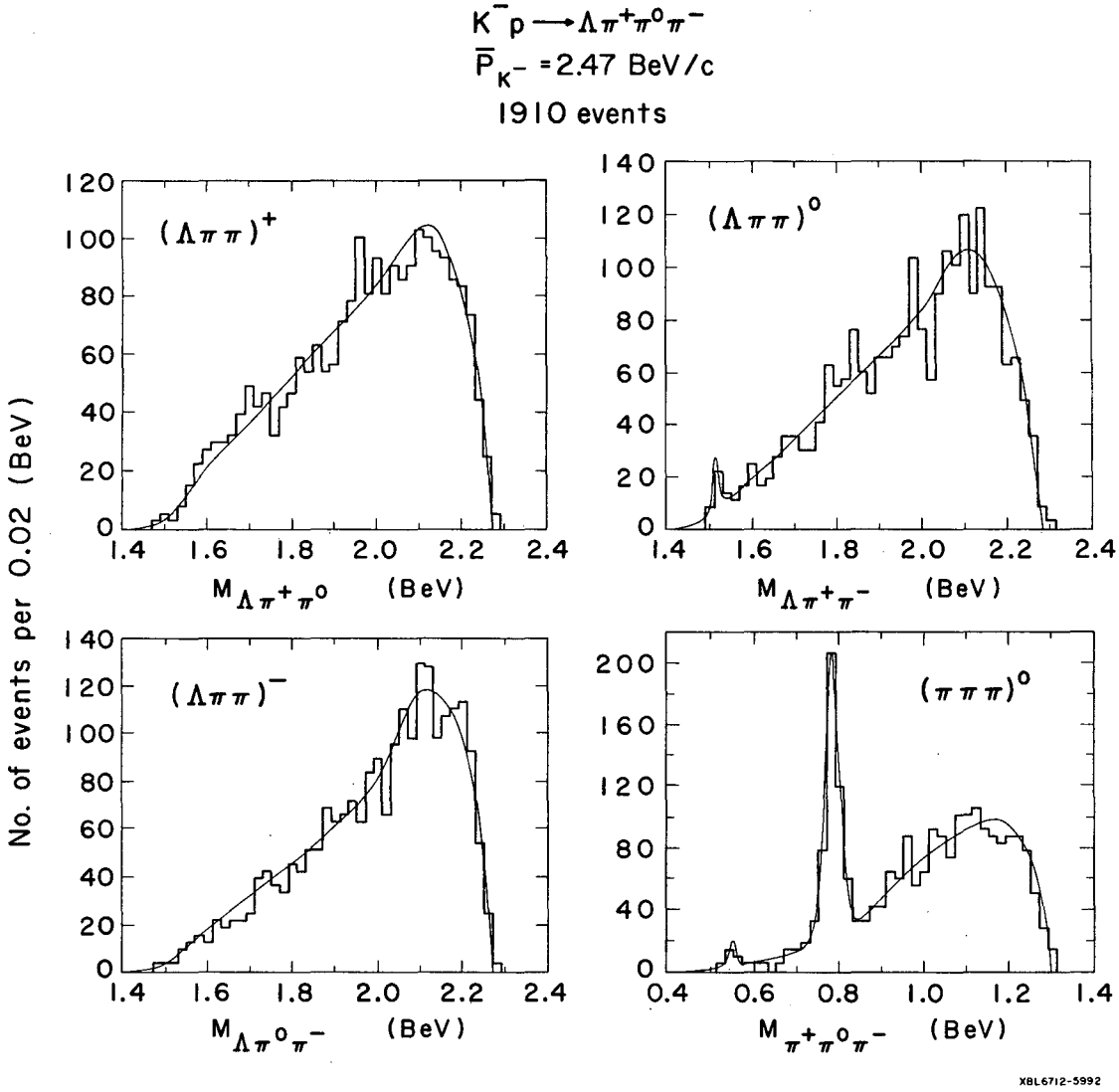

Fig. 17. Invariant mass distributions at 2.47 Bev/c (Part II). The smooth curves represent Monte Carlo calculations.

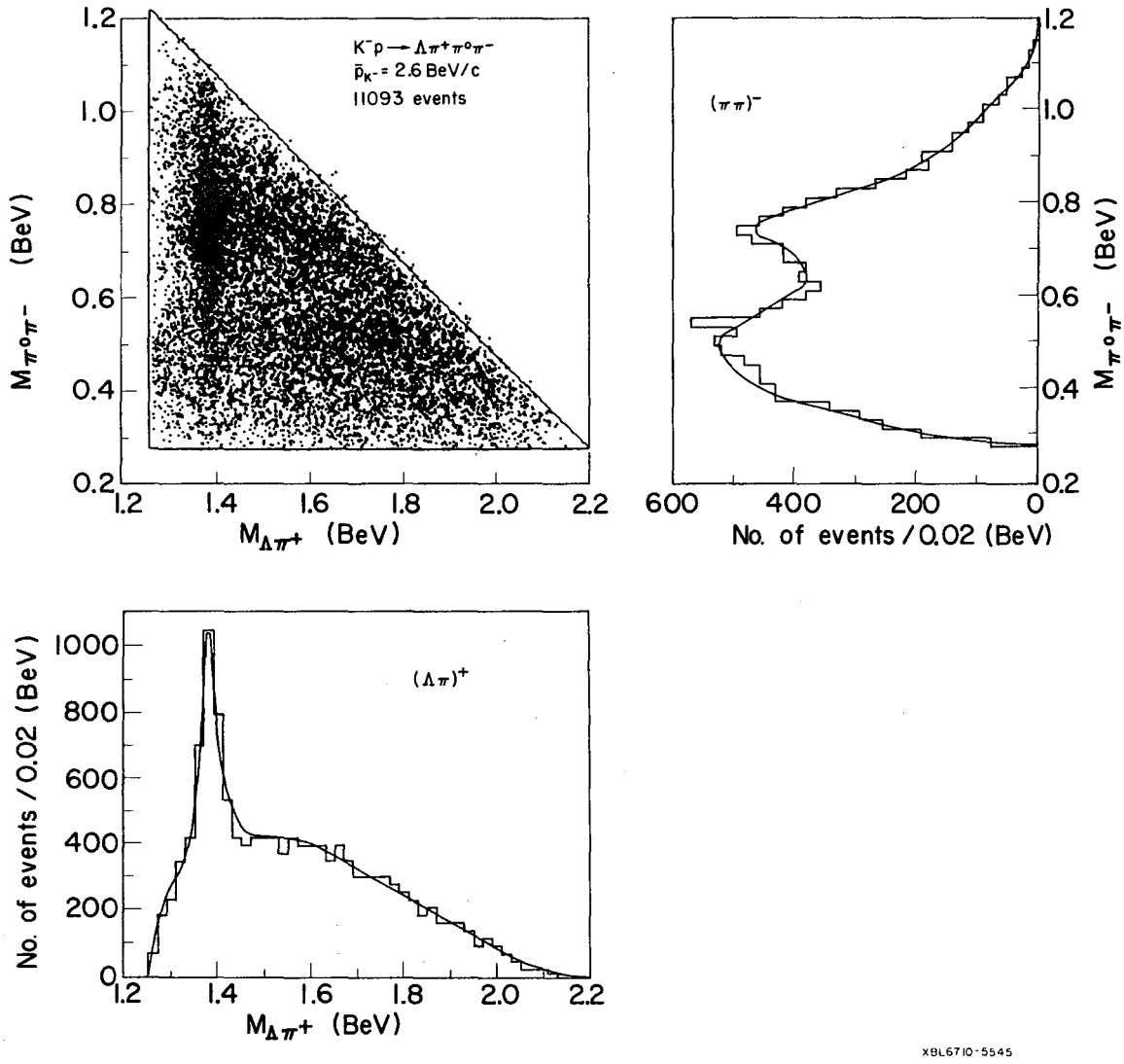

Fig. 18. Invariant mass distributions at 2.6 Bev/c (Part I). The smooth curves represent Monte Carlo calculations.

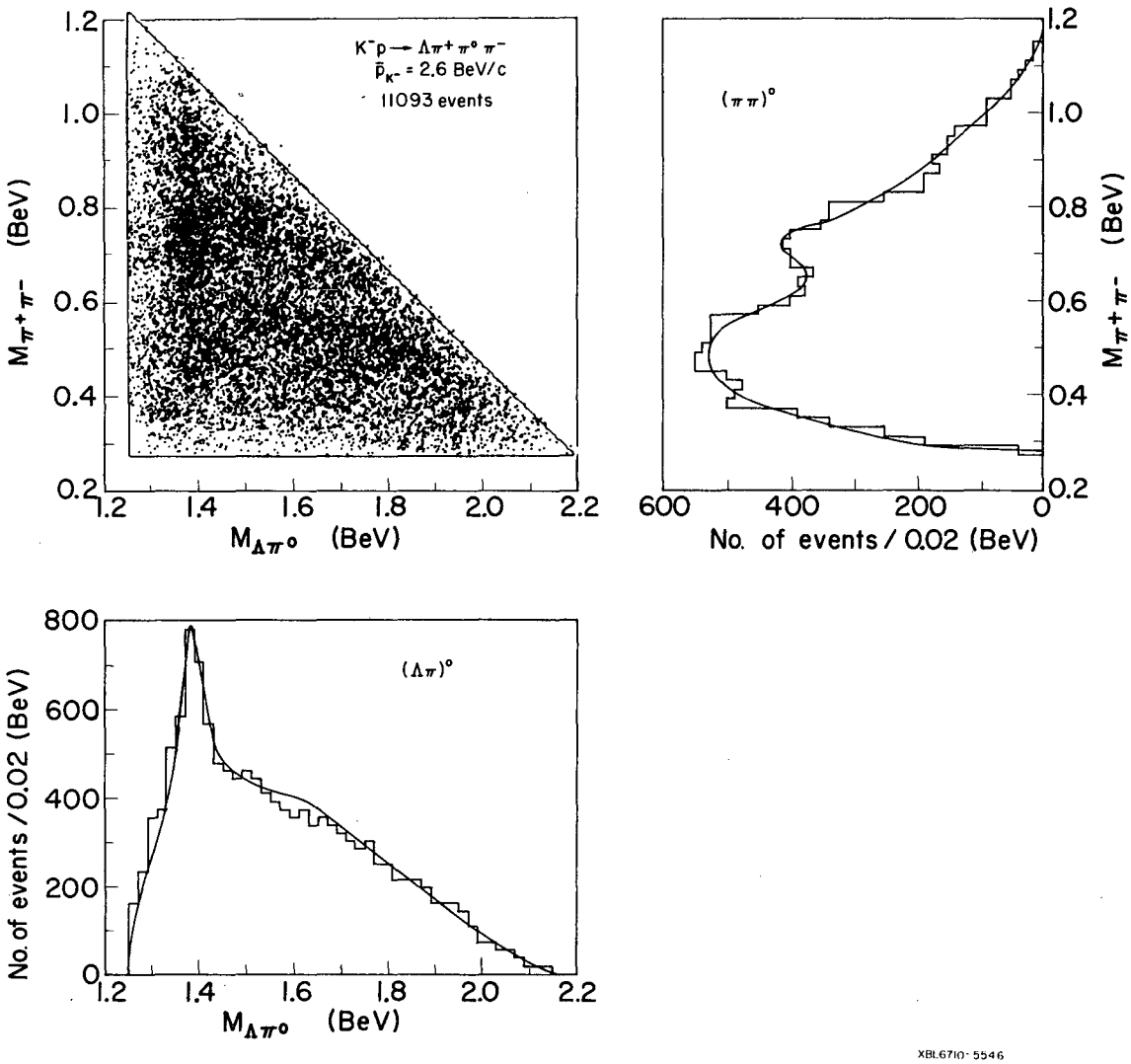

Fig. 19. Invariant mass distributions at 2.6 Bev/c (Part II). The smooth curves represent Monte Carlo calculations.

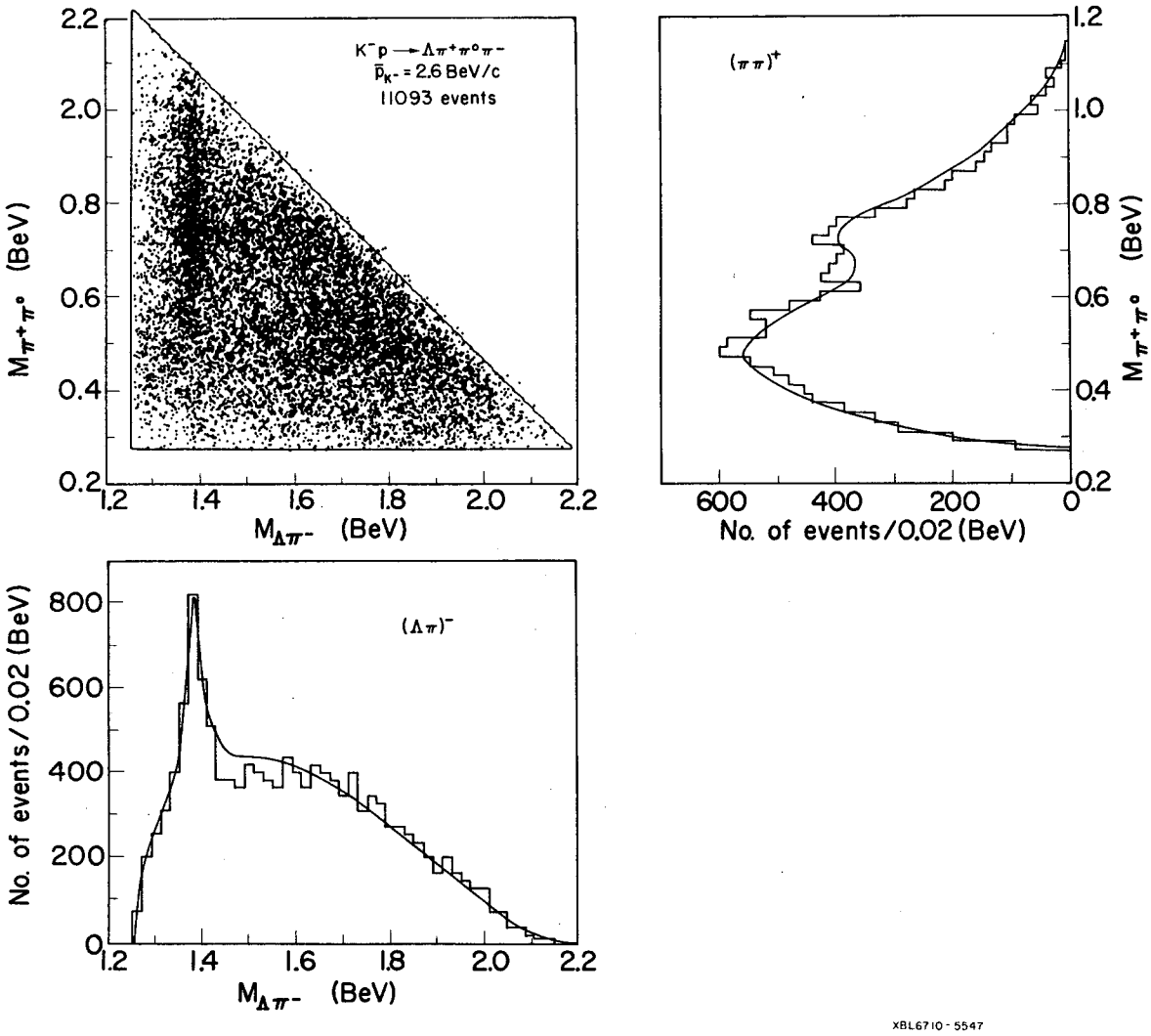

Fig. 20. Invariant mass distributions at 2.6 Bev/c (Part III). The smooth curves represent Monte Carlo calculations.

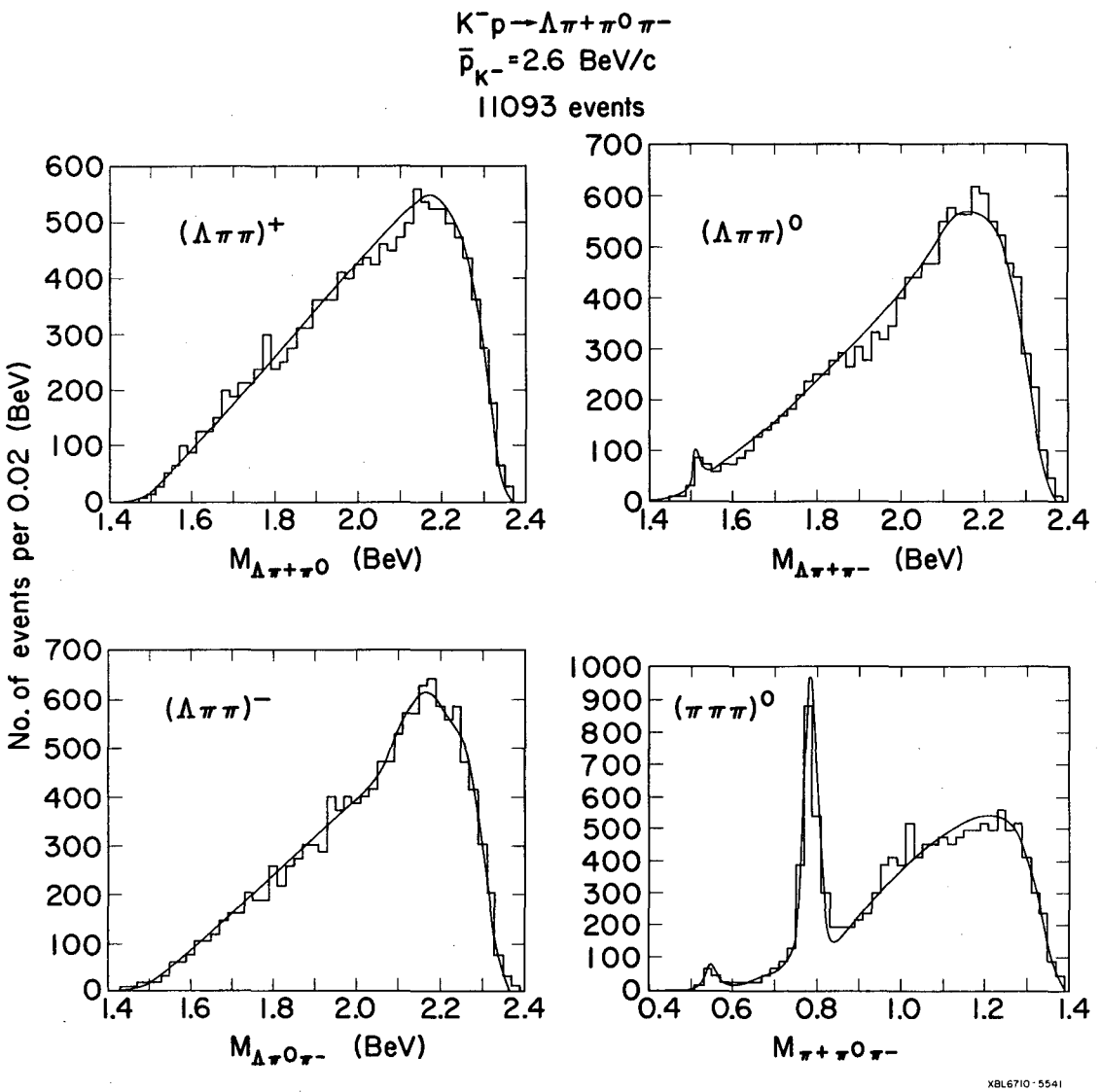

Fig. 21. Invariant mass distributions at 2.6 Bev/c (Part IV). The smooth curves represent Monte Carlo calculations.

$$Y_1^*(1385)^+ \pi^0\pi^- \quad (4)$$

$$Y_1^*(1385)^0 \pi^+\pi^- \quad (5)$$

$$Y_1^*(1385)^- \pi^+\pi^0 \quad (6)$$

$$\rho^+ \Lambda\pi^- \quad (7)$$

$$\rho^0 \Lambda\pi^0 \quad (8)$$

$$\rho^- \Lambda\pi^+ \quad (9)$$

$$\Lambda\omega \quad (10)$$

$$\Lambda\eta \quad (11)$$

$$Y_0^*(1520) \pi^0 \quad (12)$$

B. Cross Sections for the Resonant Processes

In order to obtain realistic fits to the amounts of these twelve different resonant processes, it is desirable to fit simultaneously the twelve amounts, as well as the masses and widths of the various resonances. However, due to computational difficulties involved in the simultaneous fitting of some thirty parameters, the problem is broken down as follows: Preliminary fits are made to smaller groups of parameters. Other parameters are held at estimated values while a given group is being fit, and, if inter-group correlations are relatively small, a few iterations of these preliminary fits yield stable solutions. The masses and widths emerging from this iteration procedure are then used as fixed values in a final fit in which the amounts of all the resonant processes are varied simultaneously.

Preliminary Fits for Resonance Masses and Widths

For this preliminary fitting, the variables have been divided into six groups, as shown in Table V. The resonance line shapes used are (see Chapter III): for Y_1^* (1385) and ρ, the p-wave Breit-Wigner R_1; for Y_0^* (1520), the simple Breit-Wigner R_2; and for ω and η, the Gaussian R_3 with respect to mass squared.

For this preliminary fitting involving masses and widths, a special division of the data sample into three subsamples was made, yielding the three sets of solutions shown in Table V. The first sample is the $\bar{p}_{K^-} = 2.1$ BeV/c sample, all of which was PACKAGE'ed with the correct magnetic field. (See Appendix A regarding measurement of the magnetic field in the bubble chamber.) The remaining sample, with $p_{K^-} > 2.3$ BeV/c, is divided into a portion PACKAGE'ed with the correct magnetic field, and a portion PACKAGE'ed with an incorrect magnetic field. Each of these three subsamples should now be relatively uniform with respect to the problem of fitting resonance masses and widths. In addition to the results of the fits in Table V, a typical correlation matrix for one of the fits is shown in Table VI. The significance of these results as measurements of physical quantities will be discussed in Chapter VI of this report. For purposes of subsequent analysis, the values in Table VII are taken as simple but adequate parametrizations for the whole data sample.

Fits for Cross Sections

Masses and widths having been set, we proceed to the final fits, in which the amounts of all the resonant processes (listed in

Table V (Part 1). Fits for resonance masses and widths.

Group	Parameter	Solutions: $\bar{P}_{K^-}$ = 2.1 BeV/c 6306 events (correct)[e]	Solutions: P_{K^-} > 2.3 BeV/c 4492 events (correct)[e]	Solutions: P_{K^-} > 2.3 BeV/c 8516 events (incorrect)[e]
Group I				
	$Y^{*+}\rho^-$ (o/o)[a]	12.4 ± 1.3	9.6 ± 1.1	8.8 ± 1.2
	$Y^{*+}\pi\pi$ (o/o)	5.9 ± 1.3	6.9 ± 1.1	6.2 ± 1.4
	$\rho^- \Lambda\pi$ (o/o)	0.9 ± 1.1	5.1 ± 1.2	5.2 ± 1.1
	$M_{Y^{*+}}$ (MeV)[b]	1385.9 ± 1.1	1382.8 ± 1.3	1381.7 ± 1.0
	$\Gamma_{Y^{*+}}$ (MeV)[c]	38.1 ± 3.1	37.4 ± 3.3	36.0 ± 2.4
	M_{ρ^-} (MeV)	789 ± 9	763 ± 5	756 ± 11
	Γ_{ρ^-} (MeV)	187 ± 33	125 ± 14	141 ± 40
Group II				
	$Y^{*o}\rho$ (o/o)	0.4 ± 1.0	No solution	3.2 ± 0.7
	$Y^{*o}\pi\pi$ (o/o)	15.6 ± 1.5		12.4 ± 1.1
	$\rho^o \Lambda\pi$ (o/o)	5.8 ± 1.2		2.2 ± 0.8
	$M_{Y^{*o}}$ (MeV)	1388.5 ± 2.6		1387.4 ± 2.8
	$\Gamma_{Y^{*o}}$ (MeV)	65.8 ± 8.5		84.4 ± 10.4
	M_{ρ^o} (MeV)	736 ± 9		750 ± 7
	Γ_{ρ^o} (MeV)	114 ± 27		90 ± 12
Group III				
	$Y^{*-}\rho^+$ (o/o)	5.3 ± 1.2	4.6 ± 1.0	4.0 ± 0.6
	$Y^{*-}\pi\pi$ (o/o)	6.1 ± 1.3	5.1 ± 1.1	4.5 ± 0.7
	$\rho^+ \Lambda\pi$ (o/o)	-0.3 ± 0.9	5.3 ± 1.4	3.5 ± 0.8

Table V(Part 2). Fits for resonance masses and widths.

Group	Parameter	Solutions: $\bar{P}_{K^-}$ = 2.1 BeV/c 6306 events (correct)[e]	P_{K^-} > 2.3 BeV/c 4492 events (correct)[e]	P_{K^-} > 2.3 BeV/c 8516 events (incorrect)[e]
Group III (cont.)				
	$M_{Y^{*-}}$ (MeV)	1384.6 ± 1.8	1382.1 ± 1.7	1382.0 ± 1.3
	$\Gamma_{Y^{*-}}$ (MeV)	41.7 ± 4.9	32.8 ± 4.0	31.1 ± 2.6
	M_{ρ^+} (MeV)	753 ± 9	746 ± 8	745 ± 4
	Γ_{ρ^+} (MeV)	117 ± 42	148 ± 37	124 ± 13
Group IV				
	$A\omega$ (%)	19.8 ± 0.6	15.0 ± 0.6	13.5 ± 0.4
	M_ω (MeV)	787.1 ± 0.7	784.4 ± 0.9	781.6 ± 0.6
	σ_ω (MeV)[d]	17.1 ± 0.7	18.8 ± 0.9	19.4 ± 0.7
Group V				
	$A\eta$ (%)	1.1 ± 0.2	0.7 ± 0.1	0.7 ± 0.1
	M_η (MeV)	550.8 ± 1.3	548.6 ± 1.2	544.0 ± 1.5
	σ_η (MeV)	8.4 ± 1.1	6.7 ± 0.9	10.2 ± 1.5
Group VI				
	$Y_o^*(1520)\pi$ (%)	2.1 ± 0.3	1.1 ± 0.2	0.8 ± 0.1
	$M_{Y_o^*(1520)}$ (MeV)	1516.7 ± 1.2	1517.3 ± 1.9	1515.2 ± 1.0
	$\Gamma_{Y_o^*(1520)}$ (MeV)	15.6 ± 2.8	13.9 ± 3.8	9.6 ± 2.0

a. This is the fraction of $K^-p \to \Lambda\pi^+\pi^0\pi^-$ which goes through $K^-p \to Y_1^*(1385)^+\rho^-$
b. This is the central mass for the Breit-Wigner line shape assigned to $Y_1^*(1385)^+$
c. This is the width for the Breit-Wigner line shaped assigned to $Y_1^*(1385)^+$
d. This is the standard deviation for the Gaussian shape assigned to ω
e. These comments refer to the magnetic field in the bubble chamber; see text and Appendix A.

Table VI. Correlation Matrix for Group I parameters at $\bar{P}_K$ = 2.1 BeV/c (6306 events).

	$Y^{*+}\rho^-$(%)	$Y^{*+}\pi\pi$(%)	$\rho^-\Lambda\pi$(%)	$M_{Y^{*+}}$(MeV)	$\Gamma_{Y^{*+}}$(MeV)	M_{ρ^-}(MeV)	Γ_{ρ^-}(MeV)
$Y^{*+}\rho^-$(%)	1.0	-.67	-.45	+.10	+.31	+.28	+.55
$Y^{*+}\pi\pi$(%)	-.67	1.0	+.08	+.05	+.13	-.30	-.55
$\rho^-\Lambda\pi$(%)	-.45	+.08	1.0	-.10	-.40	+.06	+.07
$M_{Y^{*+}}$ (MeV)	+.10	+.05	-.10	1.0	+.36	+.08	+.07
$\Gamma_{Y^{*+}}$ (MeV)	+.31	+.13	-.40	+.36	1.0	0.00	+.02
M_{ρ^-} (MeV)	+.28	-.30	+.06	+.08	0.00	1.0	+.72
Γ_{ρ^-} (MeV)	+.55	-.55	+.07	+.07	+.02	+.72	1.0

Table VII. Resonance masses and widths for further analysis.

Resonance	Mass (MeV)	Width (MeV)
$Y_1^*(1385)^{\pm}$	1384	37
$Y_1^*(1385)^{o}$	1388	70
$\rho^{\pm}$	760	140
ρ^{o}	740	100
ω	785	18 (σ)
η	549	9 (σ)
$Y_o^*(1520)$	1516	13

Table VIII) are allowed to vary simultaneously. The solutions are presented as percentages in Table VIII. The errors have been increased over the errors which come directly out of the fit, to reflect correlations with masses and widths, which can be estimated from the preliminary fits. A sample correlation matrix for a fit of all amounts is shown in Table IX. This table provides justification for the procedure of grouping variables used in the preliminary fits, as the inter-group correlations are seen to be small, order of 5 $^{o}/_{o}$.

In obtaining cross sections from fitted percentages, the contamination of the sample is taken into account. It is assumed that the contamination was fitted as "non-resonant $\Lambda\pi^{+}\pi^{o}\pi^{-}$". Thus, for example,

$$\sigma_{K^-p\to Y^{*+}\rho^-} = \frac{\text{fitted percentage of } Y^{*+}\rho^-}{\text{percentage of sample which is } \Lambda\pi^+\pi^o\pi^-} \times \sigma_{K^-p\to\Lambda\pi^+\pi^o\pi^-}$$

Also,

$$\sigma_{K^-p\to\Lambda\pi^+\pi^o\pi^-\ (\text{"non-resonant"})} = \sigma_{K^-p\to\Lambda\pi^+\pi^o\pi^-} - \sum \sigma_{K^-p\to \text{resonances}}$$

The cross sections thus obtained are presented in Table VIII, and the cross sections for $K^-p \to Y_1^{*}(1385)^{\pm,o}\rho^{\mp}$ are graphed as a function of beam momentum, along with the results of other experiments in this region, in Figures 8 (b), 8(c), and 8 (d). As in the case of the total $K^-p \to \Lambda\pi^+\pi^o\pi^-$ cross section, an unremarkable pattern of rise from threshold and subsequent fall is observed.

C. Monte Carlo Check on Solutions

Having found solutions for the variable parameters in our

Table VIII. Resonant amounts and cross sections in $K^- p \rightarrow \Lambda \pi^+ \pi^o \pi^-$.

Resonant Process	$\bar{P}_{k^-}$ = 2.1 BeV/c		$\bar{P}_{k^-}$ = 2.47 BeV/c		$\bar{P}_{k^-}$ = 2.6 BeV/c	
	Percentage	σ (mb)	Percentage	σ (mb)	Percentage	σ (mb)
$Y^{*+}\rho^-$	11.4±1.3	0.260±0.035	8.9±1.7	0.198±0.041	9.3±1.0	0.184±0.024
$Y^{*o}\rho^o$	0.3±1.0	0.007±0.023	5.6±1.4	0.124±0.032	2.3±0.9	0.046±0.018
$Y^{*-}\rho^+$	5.3±1.2	0.121±0.028	7.2±1.6	0.160±0.038	4.4±0.9	0.087±0.019
$Y^{*+}\pi^o\pi^-$	6.8±1.3	0.156±0.032	8.3±1.9	0.184±0.044	6.3±1.0	0.125±0.022
$Y^{*o}\pi^+\pi^-$	16.2±1.5	0.370±0.043	9.0±2.0	0.200±0.047	12.3±1.1	0.243±0.026
$Y^{*-}\pi^+\pi^-$	5.6±1.3	0.128±0.031	3.7±1.7	0.082±0.039	4.9±0.8	0.097±0.017
$\rho^+\Lambda\pi^-$	0.1±0.9	0.002±0.021	0.3±1.9	0.007±0.042	3.9±1.0	0.077±0.021
$\rho^o\Lambda\pi^o$	5.3±1.2	0.121±0.028	0.0±1.8	0.000±0.040	3.9±0.8	0.077±0.017
$\rho^-\Lambda\pi^+$	1.0±1.1	0.023±0.025	5.6±2.0	0.124±0.045	5.6±1.1	0.111±0.023
$\Lambda\omega$	19.9±0.6	0.454±0.034	17.2±1.0	0.382±0.038	13.6±0.5	0.269±0.021
$\Lambda\eta$	1.1±0.2	0.025±0.005	0.9±0.2	0.020±0.004	0.7±0.1	0.014±0.002
$Y_o^*(1520)\pi^o$	2.0±0.3	0.046±0.008	1.4±0.4	0.031±0.009	0.8±0.1	0.016±0.002
"Non-resonant" $\Lambda\pi^+\pi^o\pi^-$	25.0±3.7	0.547±0.099	31.9±5.5	0.598±0.124	32.0±2.9	0.514±0.070
TOTALS	100.0	2.260	100.0	2.110	100.0	1.860
$\Lambda\pi^+\pi^o\pi^-$ final state	99.±3.	2.26±0.16	95.±.4.	2.11±0.17	94.±2.	1.86±0.13

Table IX. Correlation Matrix for Amounts; $\bar{p}_K$- = 2.1 BeV/c (6306 events).

	$Y^{*+}\rho^-$	$Y^{*o}\rho^o$	$Y^{*-}\rho^+$	$Y^{*+}\pi\pi$	$Y^{*o}\pi\pi$	$Y^{*-}\pi\pi$	$\rho^+\Lambda\pi$	$\rho^o\Lambda\pi$	$\rho^-\Lambda\pi$	$\Lambda\omega$	$\Lambda\eta$	$Y_o^*(1520)\pi$
$Y^{*+}\rho^-$	1.00	+.01	-.00	-.61	-.05	-.05	-.02	-.02	-.51	-.06	-.01	+.01
$Y^{*o}\rho^o$	+.01	1.00	+.02	-.03	-.59	-.05	-.04	-.66	-.01	-.01	-.01	-.03
$Y^{*-}\rho^+$	-.00	+.02	1.00	-.04	-.05	-.62	-.53	-.04	-.02	-.03	-.01	+.03
$Y^{*+}\pi\pi$	-.61	-.03	-.04	1.00	+.04	+.06	+.01	+.01	+.22	-.05	-.02	-.04
$Y^{*o}\pi\pi$	-.05	-.59	-.05	+.04	1.00	+.07	+.02	+.25	-.02	-.09	-.02	+.04
$Y^{*-}\pi\pi$	-.05	-.05	-.62	+.06	+.07	1.00	+.23	+.04	-.01	-.06	-.01	-.05
$\rho^+\Lambda\pi$	-.02	-.04	-.53	+.01	+.02	+.23	1.00	+.11	+.08	+.08	+.04	-.06
$\rho^o\Lambda\pi$	-.02	-.66	-.04	+.01	+.25	+.04	+.11	1.00	+.07	+.05	+.03	+.03
$\rho^-\Lambda\pi$	-.51	-.01	-.02	+.22	-.02	-.01	+.08	+.07	1.00	+.07	+.03	-.06
$\Lambda\omega$	-.06	-.01	-.03	-.05	-.09	-.06	+.08	+.05	+.07	1.00	-.02	-.05
$\Lambda\eta$	-.01	-.01	-.01	-.02	-.02	-.01	+.04	+.03	+.03	-.02	1.00	-.01
$Y_o^*(1520)\pi$	+.01	-.03	+.03	-.04	+.04	-.05	-.06	+.03	-.06	-.05	-.01	1.00

simple model of non-interfering resonant processes, we are able to proceed with the following check on the appropriateness of the model and the relevance of the solutions: We can calculate, on the basis of the model with fitted parameters, various distributions, and then compare these calculations with the data. Monte Carlo calculations have been made, and the results for all invariant mass distributions are presented as the solid curves plotted over the data histograms in figures 12 through 21.

The solutions appear to account for the salient features of the data, within statistics (see Appendix B on weighting of events), except for the following cases: in the $\bar{P}_{K^-}$ = 2.6 BeV/c sample, in the $\pi^+\pi^o\pi^-$ mass distribution, there can be seen two effects which are not in the model. One corresponds to φ (1020); part of this effect is due to misinterpreted $K^-p \to \Lambda\varphi$, $\varphi \to K^+K^-$, and part may be real[3]. The other effect is misinterpreted $K^-p \to \Lambda\eta'(960)$, $\eta' \to \pi^+\pi^-\gamma$. Neither of these effects is adjudged to have significant influence on the fit. No other resonant states are seen. The somewhat strange shapes of the $\Lambda\pi\pi$ mass distributions are reasonably accounted for by the model. In the $\Lambda\pi^-$ mass distribution, a depression in the data is seen above the mass of the Y^*. It possibly can be explained by consideration of decay angular distributions of the ρ (see Section D of this chapter). However, for purposes of over-all fits of amounts, it was deemed imprudent to introduce even more variables to deal with relatively small effects. Some of the ρ peaks look a bit strange; we do not presume to unravel the ρ in this complex final state.

D. Production Angular Distributions

The fits documented in Tables X and XI yield production angular distributions with respect to the target proton direction in the reaction center of mass for $Y_1^*(1385)^{\pm}_{0} \rho^{0}$, $Y_1^*(1385)^{\pm}_{0} \pi\pi$, and $\rho^{\pm}_{0} \Lambda\pi$, according to the method of Chapter III, Section B. All amounts have been varied in these fits. The results for $Y^*\rho$ are presented graphically in Figures 22 and 23.

The most striking angular dependence is in the case of $K^-p \rightarrow Y^{*+}\rho^-$. The sharp forward peaking is suggestive of one meson exchange. The lightest mesons which have quantum numbers appropriate for t channel exchange are the K meson and the $K^*(890)$. These two production mechanisms can be distinguished through the influence of their angular momentum properties on the spin alignments, (hence decay angular distributions) of the Y^* and ρ. These are discussed in Section E of this chapter.

The peaked angular distribution also raises the question of the relevance of our method, which decouples effective masses from production angles, while a one meson exchange mechanism would predict a dependence on momentum transfer, which would entail some correlation of production angle with effective mass distributions. We offer the following mitigating circumstances: First, at these energies the correlation is not large. Second, peripheral phase space is important not for the resonant processes, but for the backgrounds, which are not peripheral in our case.

Table X. Fits for Production Angular Distributions $\bar{p}_K$- = 2.1 Bev/c

$\cos\theta^*(\Lambda\pi^+,p)$[b]	Number of Weighted Events [a]	$Y^{*+}\rho^-$ (%)	$Y^{*+}\pi^o\pi^-$ (%)	$\bar{\rho}\Lambda\pi^+$ (%)
1.0 to .67	1342	17.8±2.4	10.7±2.6	3.6±2.2
.67 to .33	1203	15.5±2.5	8.0±2.6	5.2±2.5
.33 to .00	1066	6.9±2.1	5.1±2.2	1.6±2.5
.00 to -.33	1106	7.2±2.5	5.8±2.6	0.0±2.2
-.33 to -.67	1232	6.4±1.7	5.7±1.9	1.8±2.0
-.67 to -1.0	1316	9.6±2.2	7.5±2.4	0.0±2.2

$\cos\theta^*(\Lambda\pi^o,p)$	Number of Weighted Events	$Y^{*o}\rho^o$ (%)	$Y^{*o}\pi^+\pi^-$ (%)	$\rho^o\Lambda\pi^o$ (%)
1.0 to 0.5	1775	-2.7±1.8	24.6±2.4	14.3±2.1
0.5 to 0.0	1559	1.0±1.7	14.8±2.2	4.6±1.8
0.0 to -.5	1442	0.4±1.7	11.0±2.5	2.0±1.9
-.5 to -1.	1530	1.9±1.9	13.3±2.6	0.0±1.7

$\cos\theta^*(\Lambda\pi^-,p)$	Number of Weighted Events	$Y^{*-}\rho^+$ (%)	$Y^{*-}\pi^+\pi^o$ (%)	$\rho^+\Lambda\pi^-$ (%)
1.0 to 0.5	1842	3.3±1.6	9.6±2.0	2.0±1.8
0.5 to 0.0	1686	4.4±1.6	6.2±1.9	1.9±1.9
0.0 to -.5	1773	5.2±1.6	3.8±1.8	0.0±1.7
-.5 to -1.	1964	6.1±1.5	4.4±1.7	0.0±1.6

[a] The factor which relates cross section to number of resonant events for this sample is (0.315±0.022) microbarns/event.

[b] For $K^-p \rightarrow Y^*\rho$, $\cos\theta^*(\Lambda\pi,p) = 1.0$ corresponds to 4-momentum transfer $\Delta^2 = (p_{Y^*} - p_{proton})^2 = +.25$ (Bev/c)^2, while $\cos\theta^*_{(\Lambda\pi,p)} = -1.0$ corresponds to $\Delta^2 = +1.47$ (Bev/c)^2.

Table XI. Fits for Production Angular Distributions $\bar{p}_K$- = 2.6 Bev/c

cos θ ($\Lambda\pi^+$,p)(b)	Number of Weighted Events(a)	$Y^{*+}p^-$ (%)	$Y^{*+}\pi^o\pi^-$ (%)	$\rho^-\Lambda\pi^+$ (%)
1.0 to 0.8	2633	17.7±1.8	9.6±1.8	3.9±1.8
0.8 to 0.6	1901	14.2±1.6	4.9±1.6	8.0±1.9
0.6 to 0.4	1559	13.5±2.0	6.2±2.0	5.5±2.3
0.4 to 0.2	1430	10.0±2.3	4.8±2.4	6.2±2.9
0.2 to 0.0	1220	8.0±2.4	4.3±2.5	10.0±3.4
0.0 to -.2	1168	3.4±3.6	7.8±4.2	8.6±5.0
-.2 to -.4	1223	1.0±1.5	7.5±2.0	8.4±2.5
-.4 to -.6	1211	4.6±2.1	4.1±2.4	4.0±2.8
-.6 to -.8	1326	3.6±1.7	8.4±2.0	3.2±2.2
-.8 to -1.	1522	6.6±1.6	3.9±1.8	0.0±2.5

cos θ ($\Lambda\pi^o$,p)	Number of Weighted Events	$Y^{*o}p^o$ (%)	$Y^{*o}\pi^+\pi^-$ (%)	$\rho^o\Lambda\pi^o$ (%)
1.0 to 0.5	5273	2.9±0.9	11.5±1.3	7.0±1.2
0.5 to 0.0	3266	4.0±1.1	11.6±1.6	1.1±1.4
0.0 to -.5	3216	0.1±1.4	13.2±2.0	4.2±1.8
-.5 to -1.	3439	3.2±1.7	11.4±2.7	2.9±2.5

cos θ ($\Lambda\pi^-$,p)	Number of Weighted Events	$Y^{*-}p^+$ (%)	$Y^{*-}\pi^+\pi^o$ (%)	$\rho^+\Lambda\pi^-$ (%)
1.0 to 0.5	4508	1.3±0.9	8.5±1.1	6.5±1.3
0.5 to 0.0	3232	3.0±1.0	3.3±1.2	5.8±1.5
0.0 to -.5	3439	6.2±1.2	2.3±1.3	0.6±1.6
-.5 to -1.	4015	8.9±1.0	4.1±1.1	0.0±1.2

[a] The factor which relates cross section to number of resonant events for this sample is (0.132±0.010) microbarns/event.

[b] For $K^-p \rightarrow Y^*\rho$, $\cos\theta_{(\Lambda\pi,p)} = 1.0$ corresponds to 4-momentum transfer $\Delta^2 = (p_{Y^*} - p_{\text{proton}})^2 = +.14$, while $\cos\theta\ (\Lambda\pi, p) = -1.0$ corresponds to $\Delta^2 = +2.48$

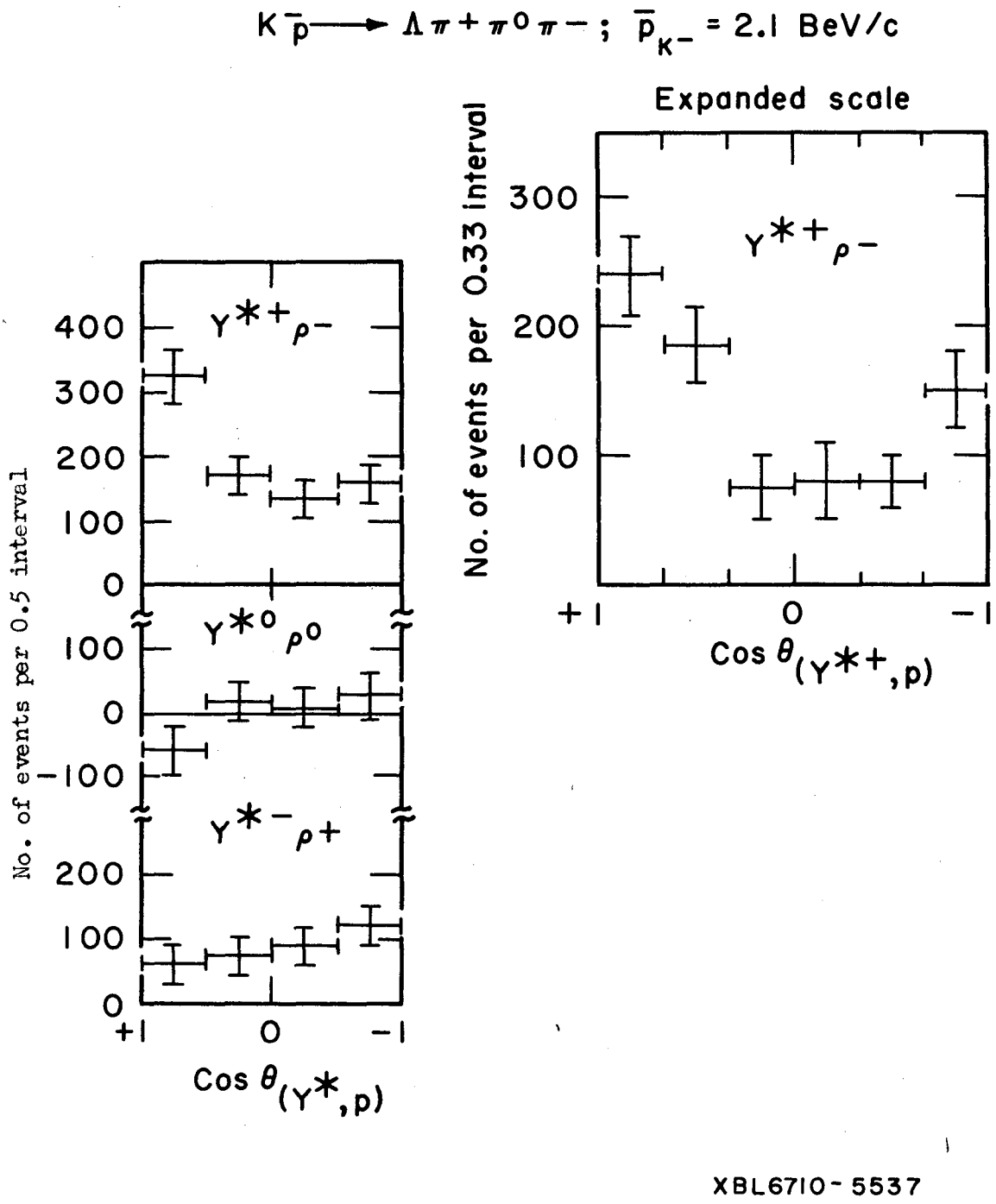

Fig. 22. Production angular distributions in the reaction center of mass, for $K^- p \to Y_1^{*}(1385)^{\pm} \rho^{\mp}$ at 2.1 Bev/c.

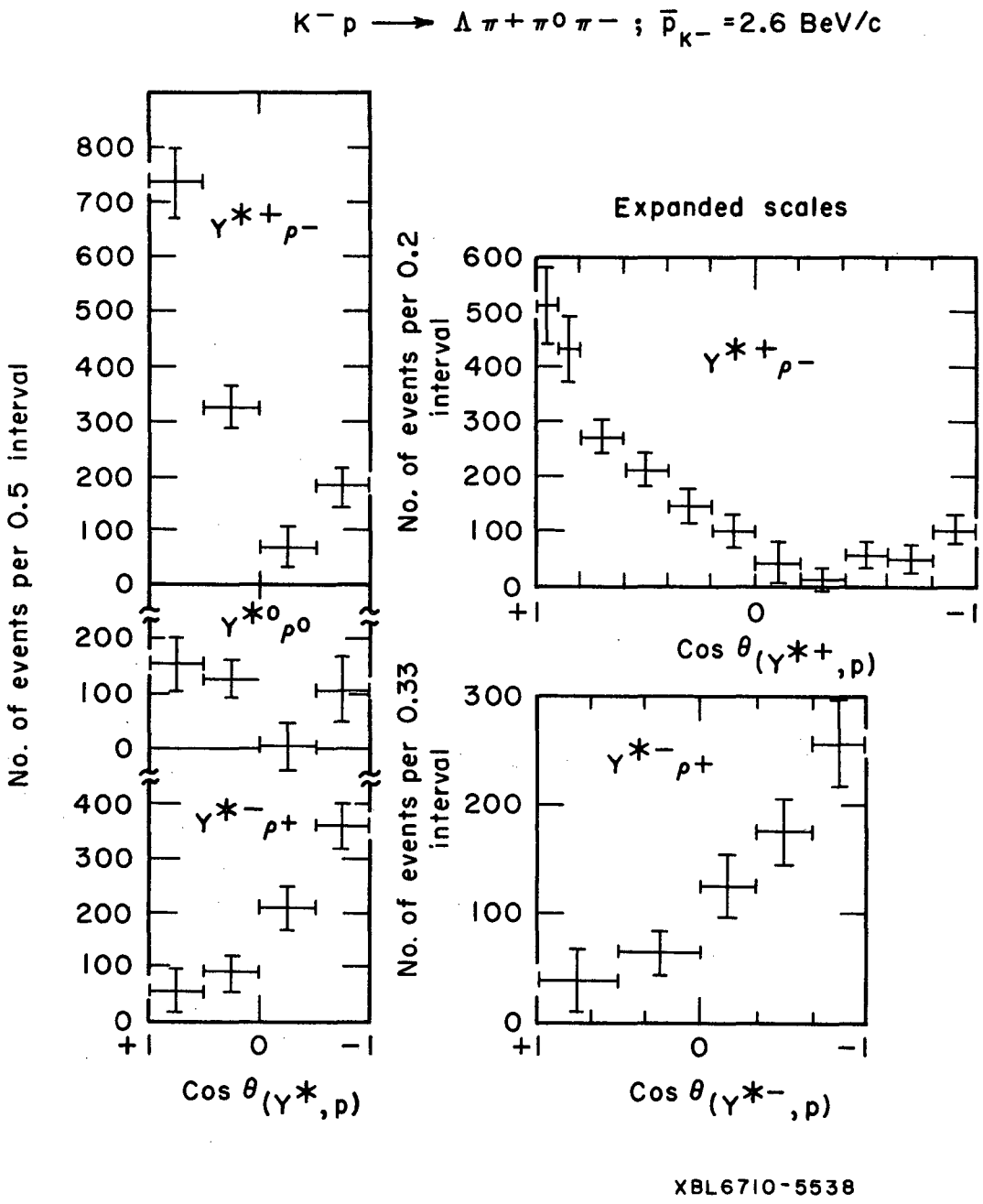

Fig. 23. Production angular distributions in the reaction center of mass, for $K^- p \rightarrow Y_1^*(1385)^{\pm} \rho^{\mp}$ at 2.6 Bev/c.

Relationships Among the Three Charge States of $Y^*\rho$

The production angular distributions of $Y_1^*(1385)^+\ \rho^-$, $Y_1^*(1385)^0\ \rho^0$, and $Y_1^*(1385)^-\ \rho^+$ are related by charge independence, in a manner depending on the specific model chosen to represent the production process. The following simple model is consistent with the observed distributions: $Y^{*+}\rho^-$ proceeds entirely through K and K^* exchange. The amplitude for $Y^{*0}\rho^0$ by this mechanism is then, by charge independence, one-half the $Y^{*+}\rho^-$ amplitude. We further assume that $Y^{*-}\rho^+$ goes entirely by nucleon exchange in the u-channel. ($N^*(1238)$ exchange is also allowed, but it requires an amplitude for $Y^{*+}\ \rho^-$ which is 3 times as large as the $Y^{*-}\rho^+$ amplitude. This allows only a small contribution, which we neglect in this simplified model.) The amplitude for $Y^{*0}\rho^0$ by this u-channel exchange is one-half the $Y^{*-}\rho^+$ amplitude. If we now add these t- and u-channels contributions to the $Y^{*0}\rho^0$ state, with the amplitudes 180^0 out of phase, we get production angular distributions which are consistent with the $Y^{*0}\rho^0$ data, both for $\bar{p}_{K^-} = 2.1$ and for $\bar{p}_K = 2.6$ BeV/c.

E. Decay angular distributions for $K^-p \rightarrow Y_1^*(1385)^+\ \rho^-$

Fits to decay angular distribtuions of $Y_1^*(1385)^+$ and ρ^- are made for data samples corresponding to three different intervals of production angle, and the resulting density matrix elements, in the t-channel coordinate system, are presented in Table XII, and in graphical form in Figures 24 and 25. (In these fits, fixed amounts appropriate to the individual samples are used.) The density matrix elements

Table XII. Density Matrix Elements.

$\bar{p}_{K^-}$ = 2.6 BeV/c

	Matrix Element[b]	$\cos\theta_{(Y^{*+},p)}$ 1.0 to .67[a]	.67 to .33	.33 to 0.0
Y^{*+}	ρ_{33}	-.03 ± .03	0.13 ± .05	0.07 ± .09
	Re ρ_{31}	-.05 ± .04	-.07 ± .05	-.09 ± .08
	Re $\rho_{3,-1}$	0.00 ± .03	0.13 ± .05	0.06 ± .08
ρ^-	ρ_{00}	0.71 ± .05	0.48 ± .06	0.47 ± .12
	Re ρ_{10}	-.26 ± .03	-.19 ± .04	-.26 ± .08
	$\rho_{1,-1}$	-.02 ± .03	-.06 ± .05	-.04 ± .08

$\bar{p}_{K^-}$ = 2.1 BeV/c

Y^{*+}	ρ_{33}	0.15 ± .06	0.17 ± .07	0.19 ± .11
	Re ρ_{31}	-.06 ± .06	-.08 ± .06	-.18 ± .12
	Re $\rho_{3,-1}$	-.01 ± .05	0.06 ± .06	0.00 ± .11
ρ^-	ρ_{00}	0.67 ± .07	0.33 ± .09	0.18 ± .12
	Re ρ_{10}	-.14 ± .05	-.08 ± .05	-.17 ± .10
	$\rho_{1,-1}$	-.09 ± .05	-.17 ± .07	-.36 ± .18

a. The intervals in Δ^2 $(\text{BeV/c})^2$ corresponding to the above intervals in $\cos\theta_{(Y^{*+},p)}$ are

for $\bar{p}_{K^-}$ = 2.6 BeV/c : 0.14 to 0.53, 0.53 to 0.92, 0.92 to 1.31

for $\bar{p}_{K^-}$ = 2.1 BeV/c : 0.25 to 0.45, 0.45 to 0.65, 0.65 to 0.85

b. Density matrix elements are evaluated in the t-channel coordinate system, see Ref. 10.

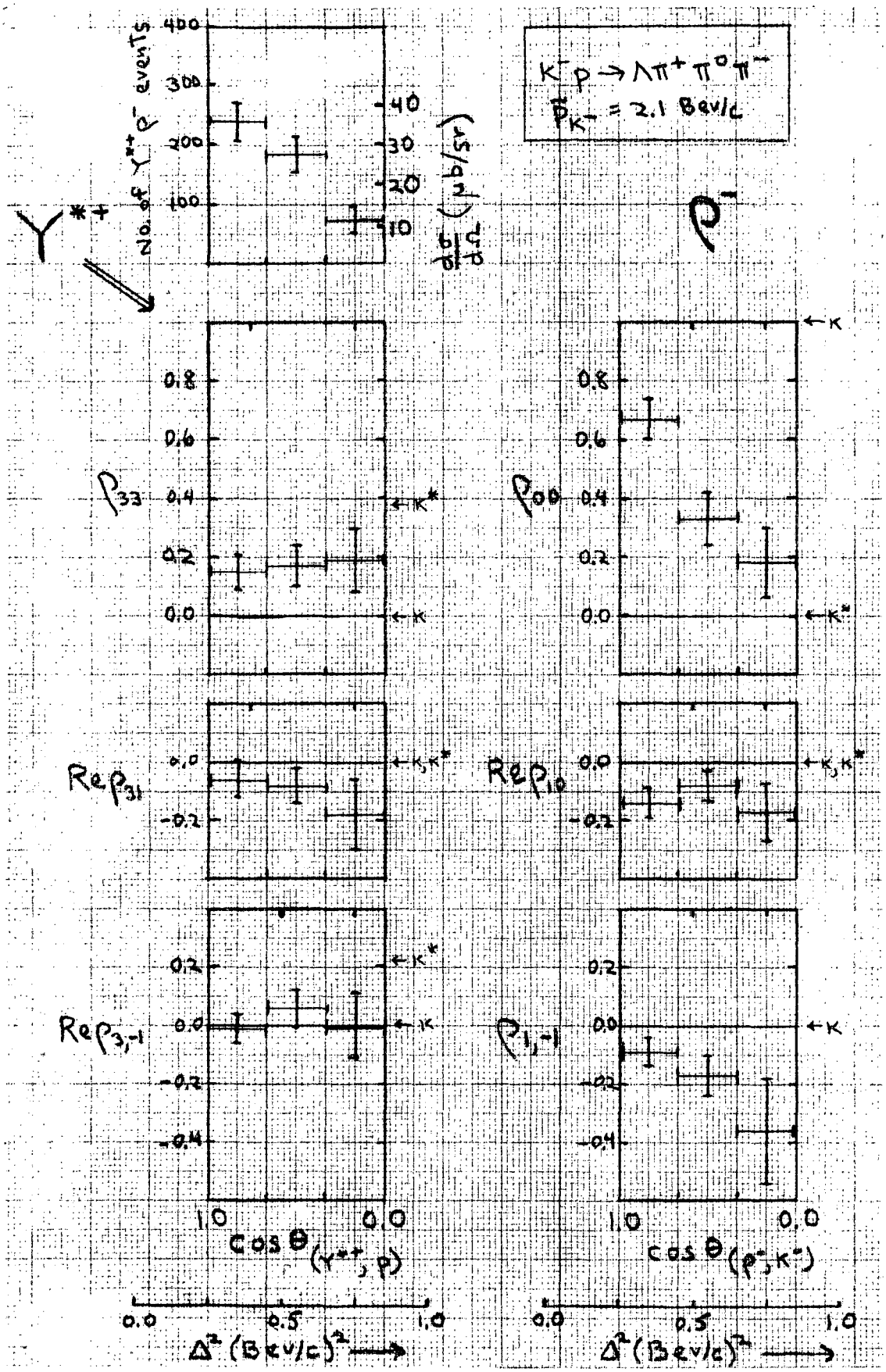

Fig. 24. Spin-density-matrix elements as a function of production angle for $K^- p \to Y_1^*(1385)^+ \rho^-$ at 2.1 Bev/c.

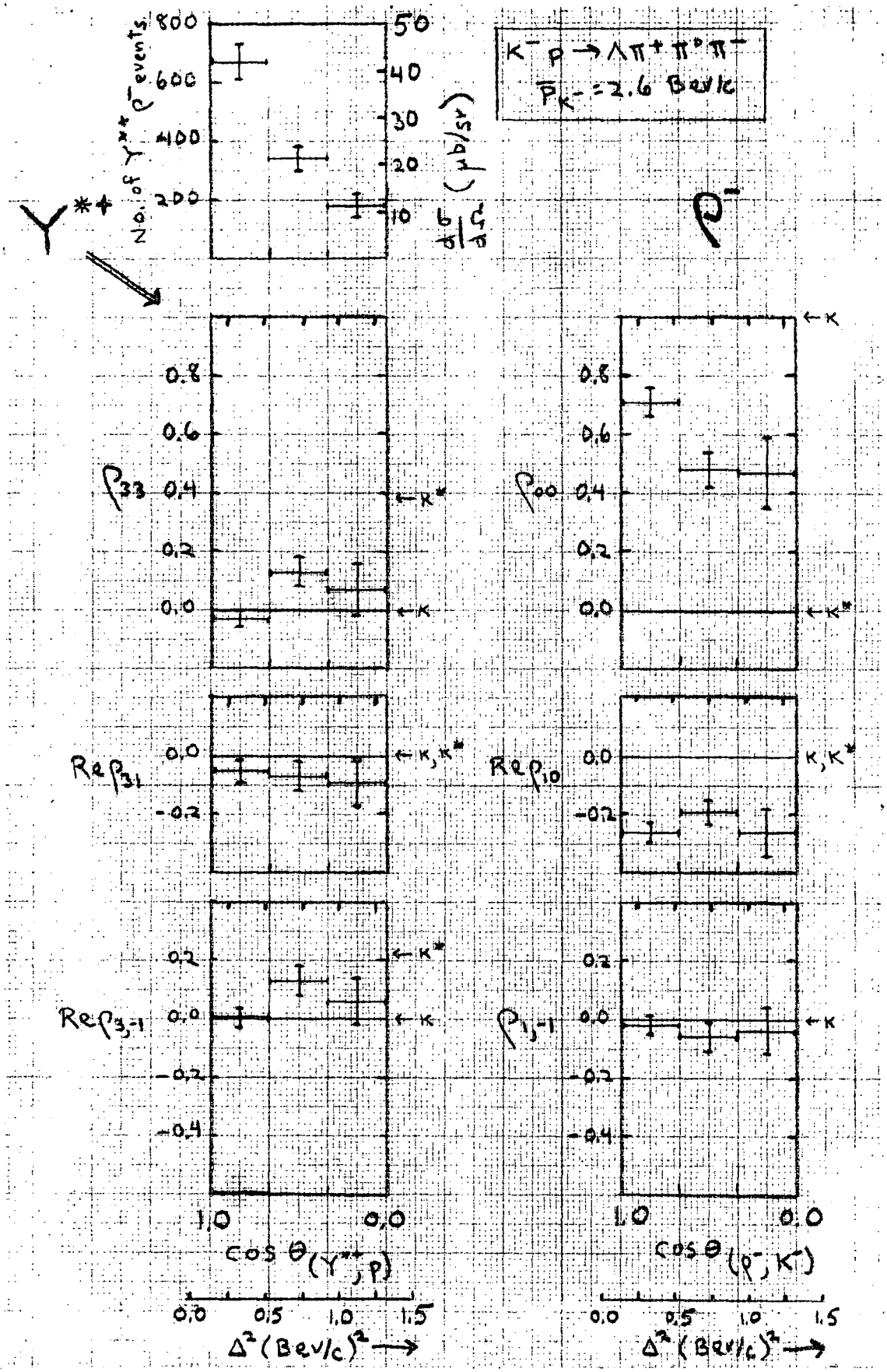

Fig. 25. Spin-density-matrix elements as a function of production angle for $K^- p \to Y_1^*(1385)^+ \rho^-$ at 2.6 Bev/c.

indicated at small momentum transfer are consistent with simple K meson exchange, which predicts the values indicated by the arrows in Figures 23 and 24; the trends toward larger momentum transfer are similar to those calculated on the basis of an absorption model with pseudoscalar exchange, for another $\frac{1+}{2} + 0^- \rightarrow \frac{3+}{2} + 1^-$ reaction.[10] On the other hand, any contribution of K^* exchange according to the Sakurai-Stodolsky model[15] (also indicated by arrows in Figures 23 and 24) would appear to be less significant. (See also the distributions of cos Θ in Figures 26 and 27, discussed below.)

Comparison of Fits with Subtracted Data

As a check on our solutions for density matrix elements, we present in Figures 26 and 27 comparisons between the model with fitted parameters (solid curves), and subtracted data points obtained by the procedures of Appendix D. (Θ and φ are the appropriate t-channel coordinates, while Θ_n is redundant and is the Y^* decay angle with respect to the production normal. Θ_n should have a striking $1 + 3\cos^2\Theta_n$ distribution for K^* exchange in the magnetic dipole coupling model.) The comparison appears to indicate that the model is qualitatively correct, but that significant systematic errors may be present in the numerical solutions, especially at large momentum transfer.

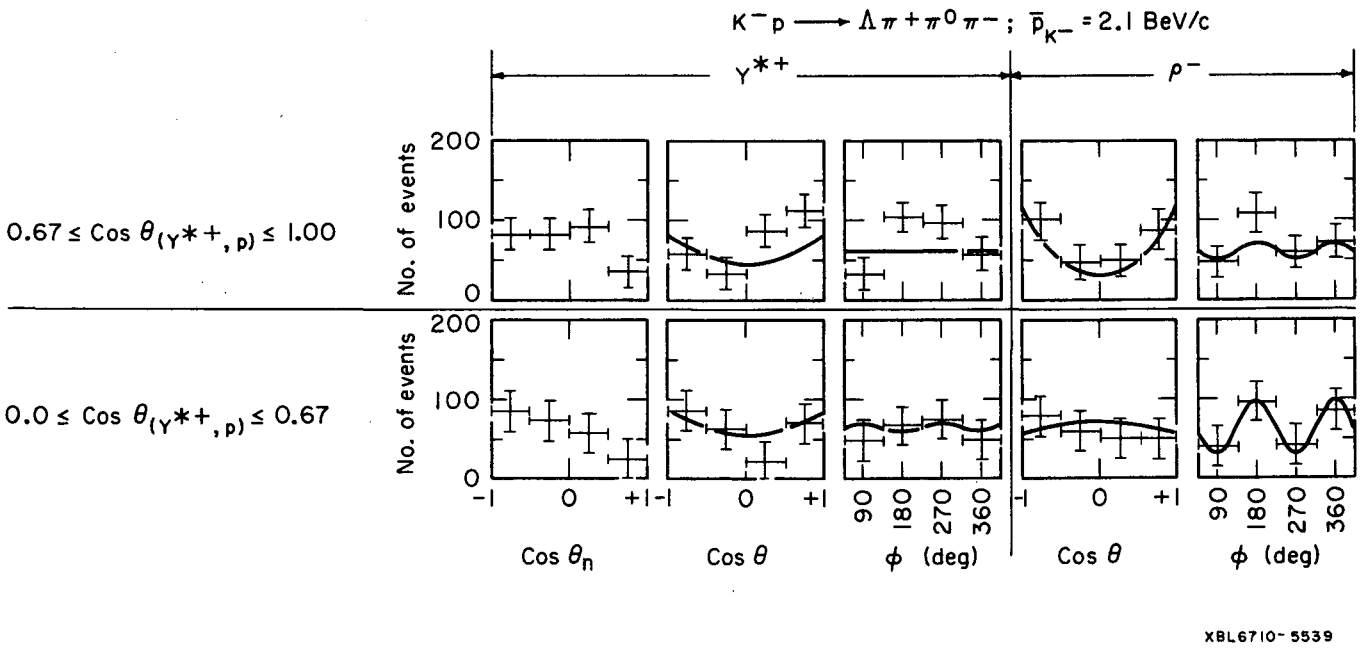

Fig. 26. Decay angular distributions for $Y_1^*(1385)^+$ and ρ^-: the smooth curves represent the spin-density-matrix elements in Fig. 24, while the corresponding data points are the results of a subtraction procedure (see Appendix D).

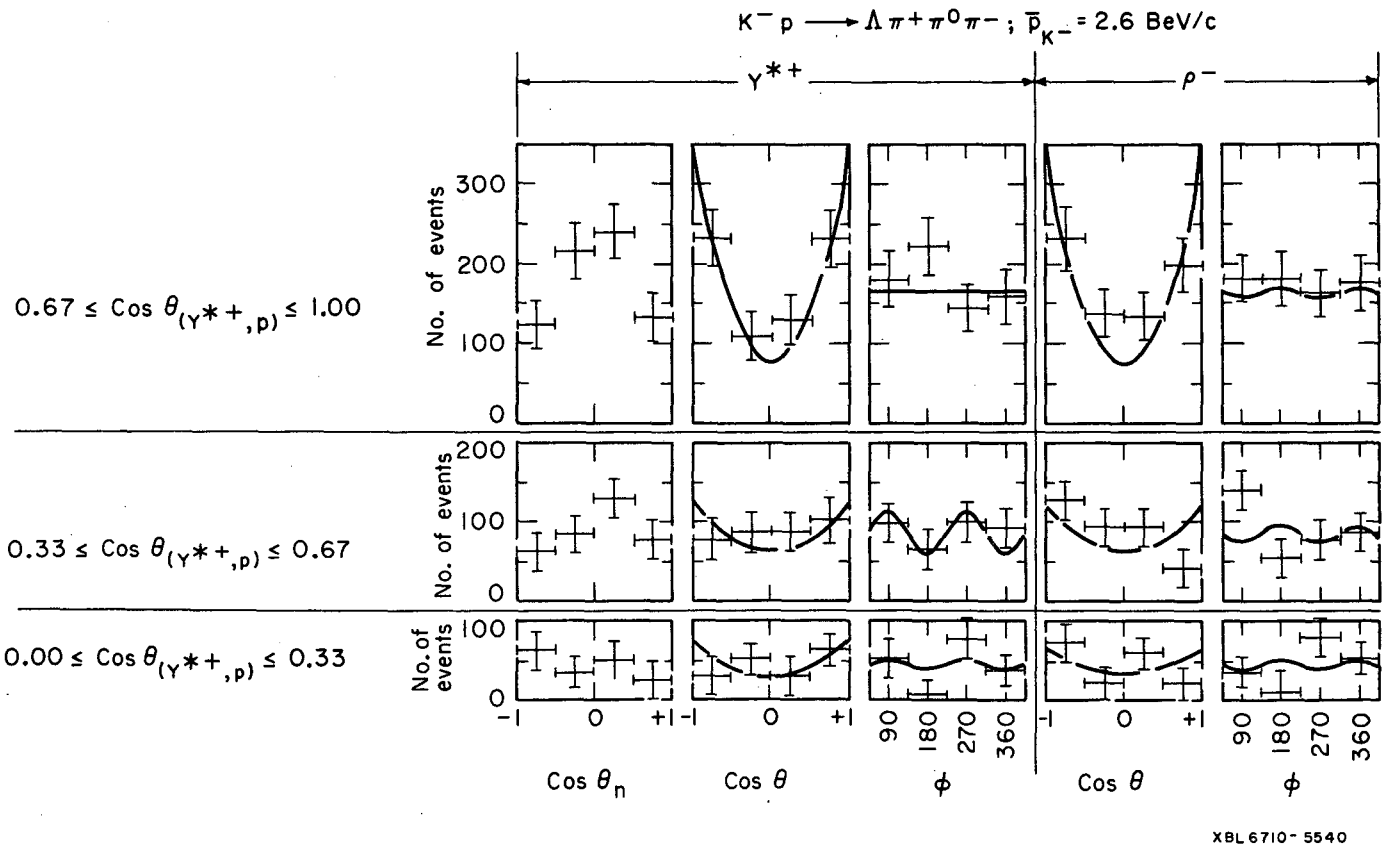

Fig. 27. Decay angular distributions for $Y_1^*(1385)^+$ and ρ^-: the smooth curves represent the spin-density-matrix elements in Fig. 25, while the corresponding data points are the results of a subtraction procedure (see Appendix D).

V. RESONANCE PRODUCTION IN $K^- p \rightarrow \Lambda \pi^+ \pi^-$

In this chapter, the fitting procedures of Chapter III are applied to the $K^- p \rightarrow \Lambda \pi^+ \pi^-$ data sample.

A. The $K^- p \rightarrow \Lambda \pi^+ \pi^-$ Data Sample

The distribution of K^- beam momentum, for the 11,000 $K^- p \rightarrow \Lambda \pi^+ \pi^-$ events in this data sample, is shown in Figure 28; also illustrated is the division into subsamples with $\bar{p}_{K^-}$ = 2.1, 2.47, and 2.6 Bev/c. A graph of the $K^- p \rightarrow \Lambda \pi^+ \pi^-$ cross section as a function of beam momentum is presented in Figure 29. No strong s-channel effects are apparent. (See discussion of partial cross sections below.)

Dalitz plots and projections for the $\Lambda \pi^+ \pi^-$ final state are presented in Figures 30, 32, and 33. The dominant resonant enhancements correspond to $Y_1^*(1385)^+$, $Y_1^*(1385)^-$, and ρ^o. Broad enhancements are seen in both the $\Lambda \pi^+$ and $\Lambda \pi^-$ mass squared spectra in the region of 2.5-3.5 Bev^2. Possible contributors to these enhancements are the well-known $Y_1^*(1660)$ and $Y_1^*(1770)$, as well as the more recently reported $Y_1^*(1680)$.[22] Parametrization of these various enhancements is described below.

B. Cross Sections for the Resonant Processes

Due to the high degree of correlation between the parameters describing the various resonant contributions to the $\Lambda \pi^+ \pi^-$ final state, the first fits yielding useful results, shown in Table XIII, involve simultaneous variation of some 18 parameters. (The correlation matrix for one of these fits, Table XIV, shows the necessity for this.)

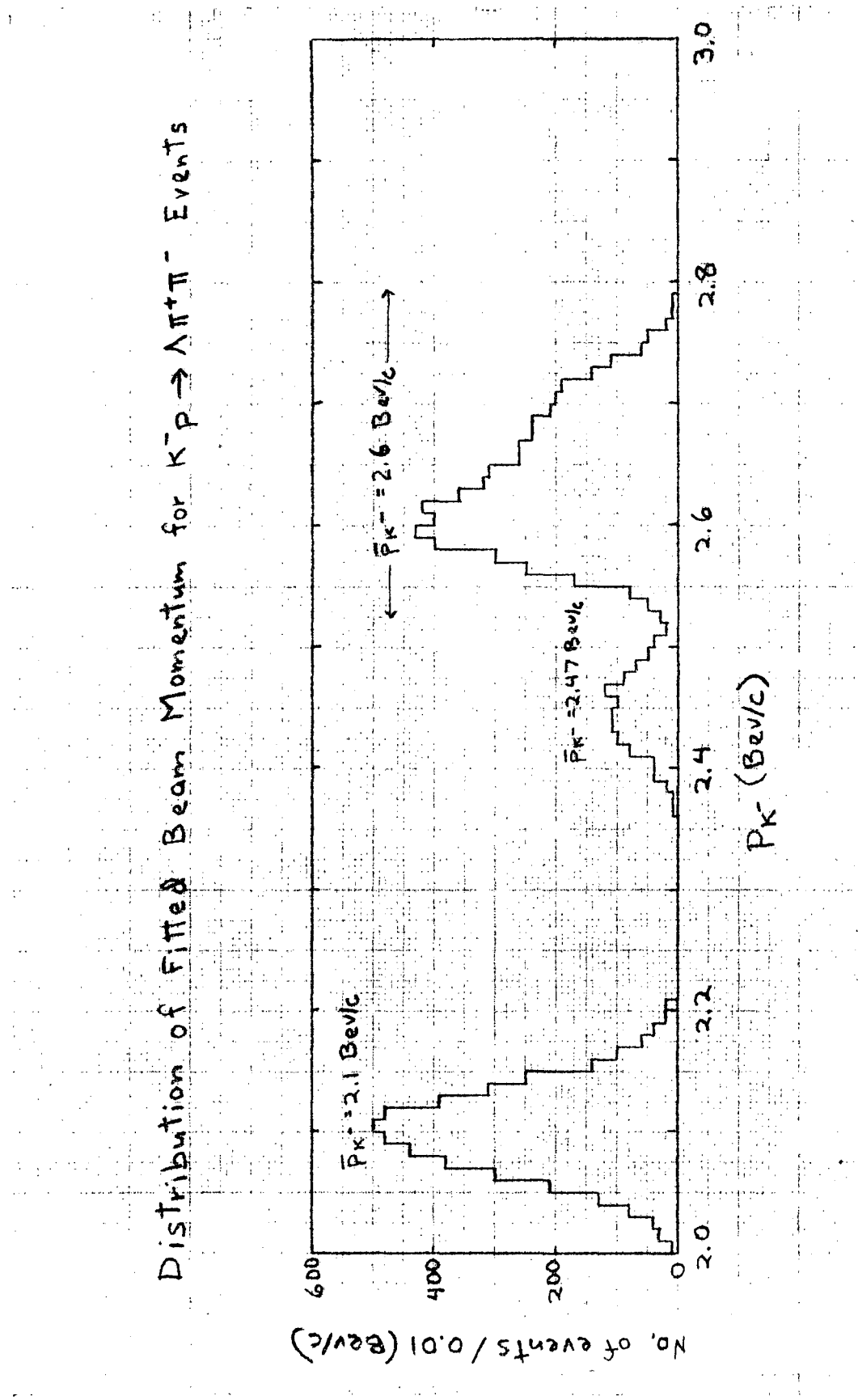

Fig. 23. Distribution of fitted beam momentum for $K^-p \to \Lambda\pi^+\pi^-$ events.

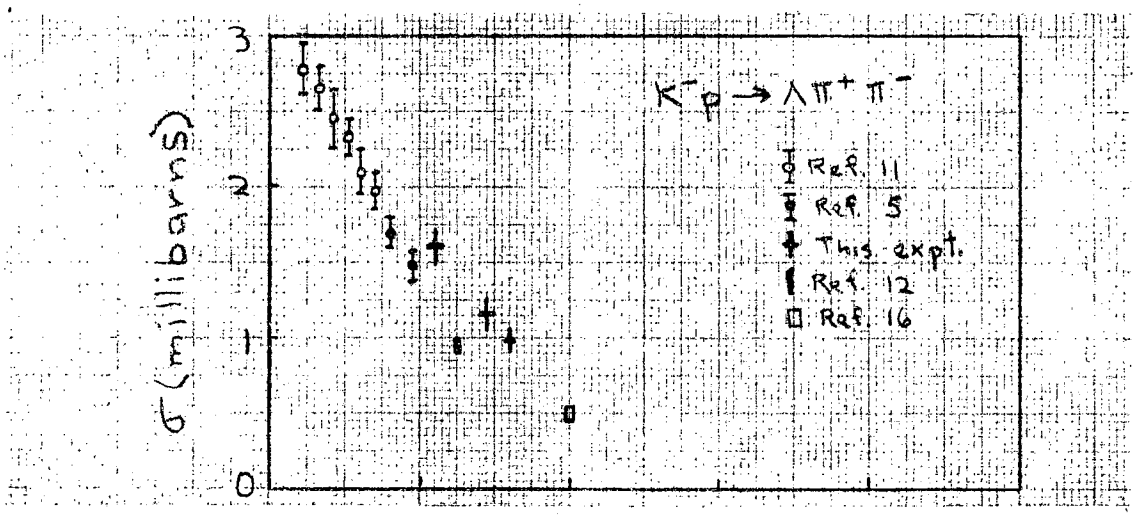

Fig. 29. Total cross section as a function of incident beam momentum for $K^- p \to \Lambda \pi^+ \pi^-$.

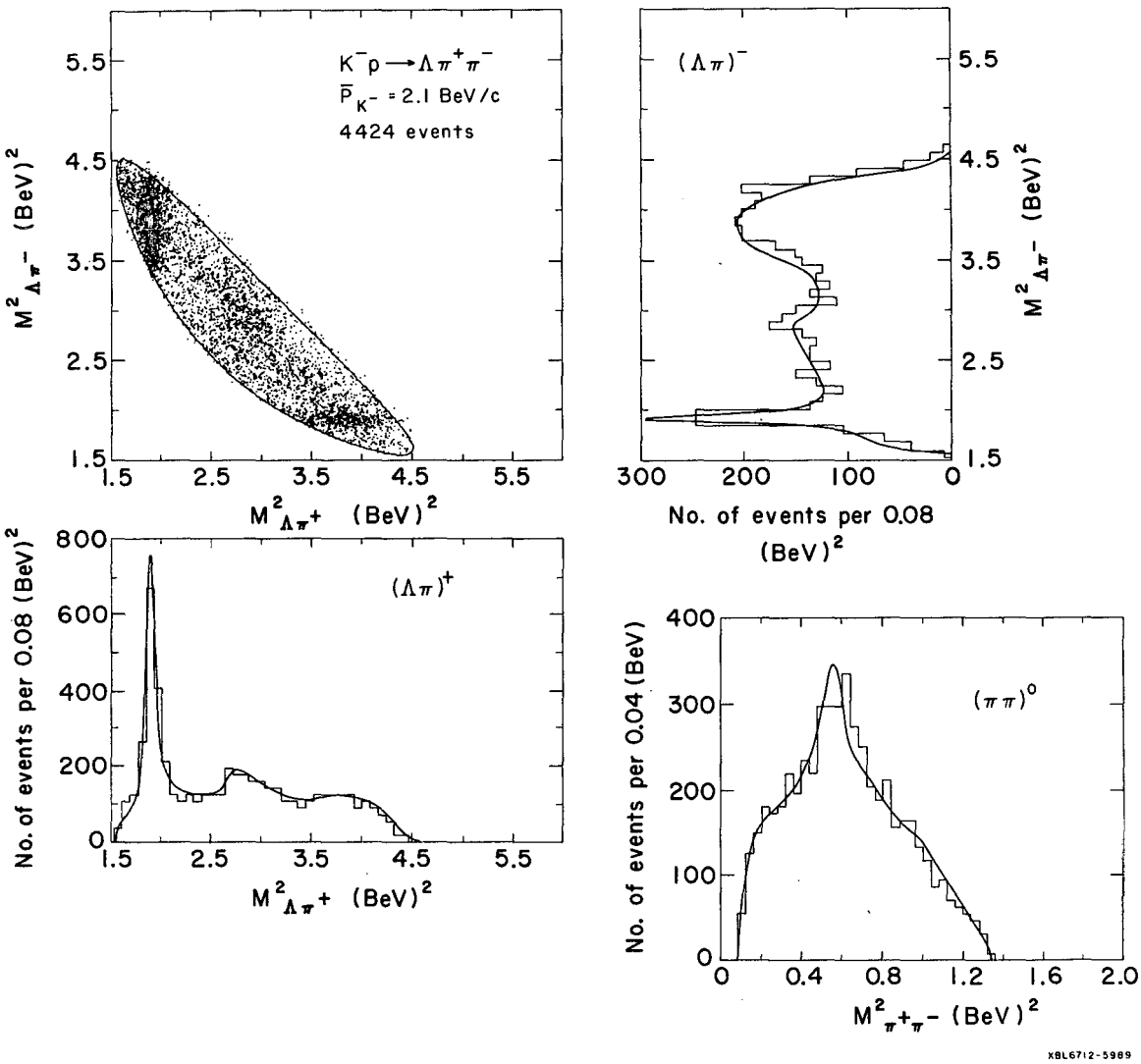

Fig. 30. Dalitz plot and projections for the reaction $K^- p \rightarrow \Lambda \pi^+ \pi^-$ at 2.1 Bev/c. The smooth curves represent Monte Carlo calculations.

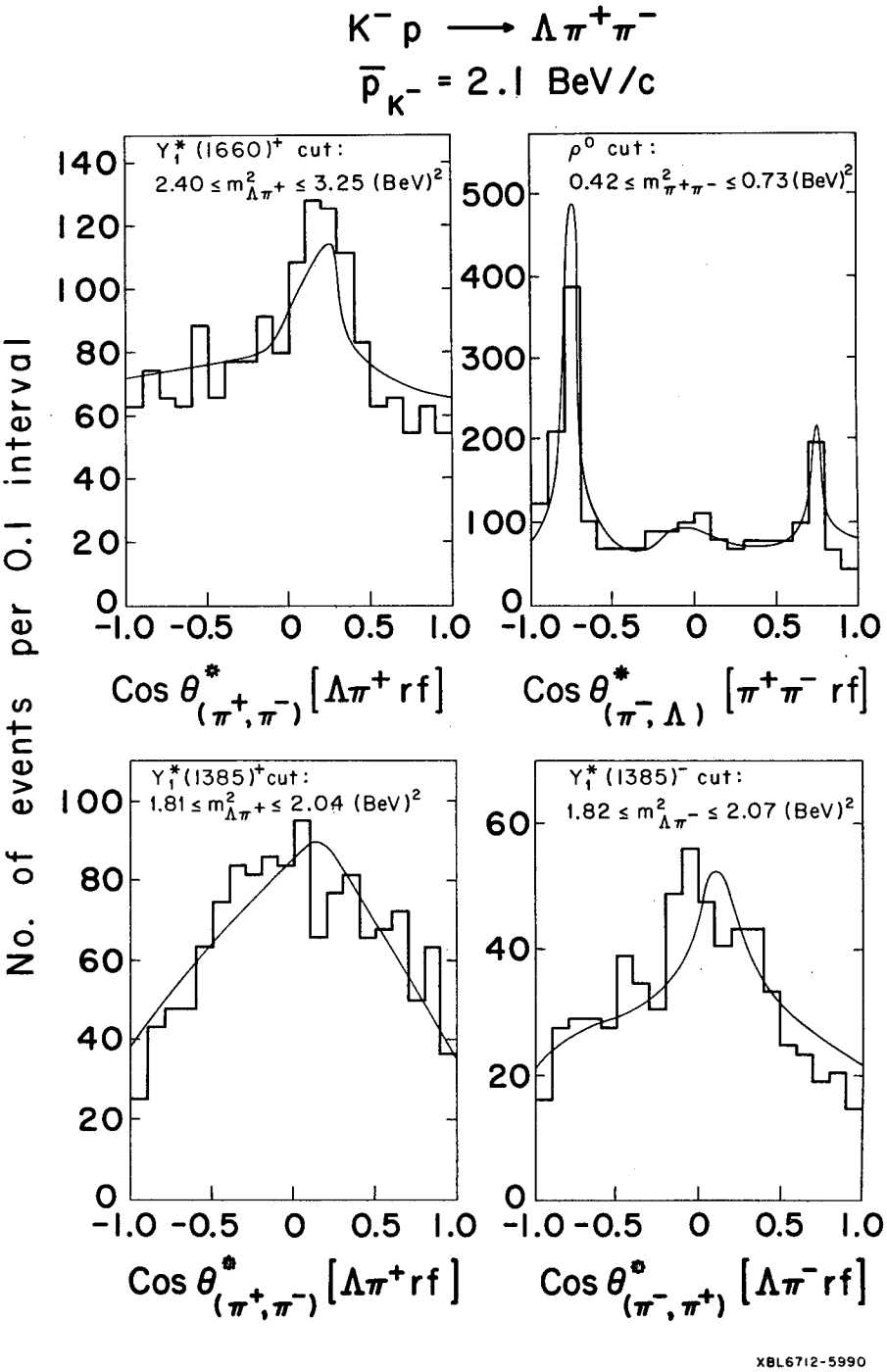

Fig. 31. Decay angular distributions relevant to $\Lambda\pi^+\pi^-$ Dalitz plot at 2.1 Bev/c. The smooth curves represent Monte Carlo calculations.

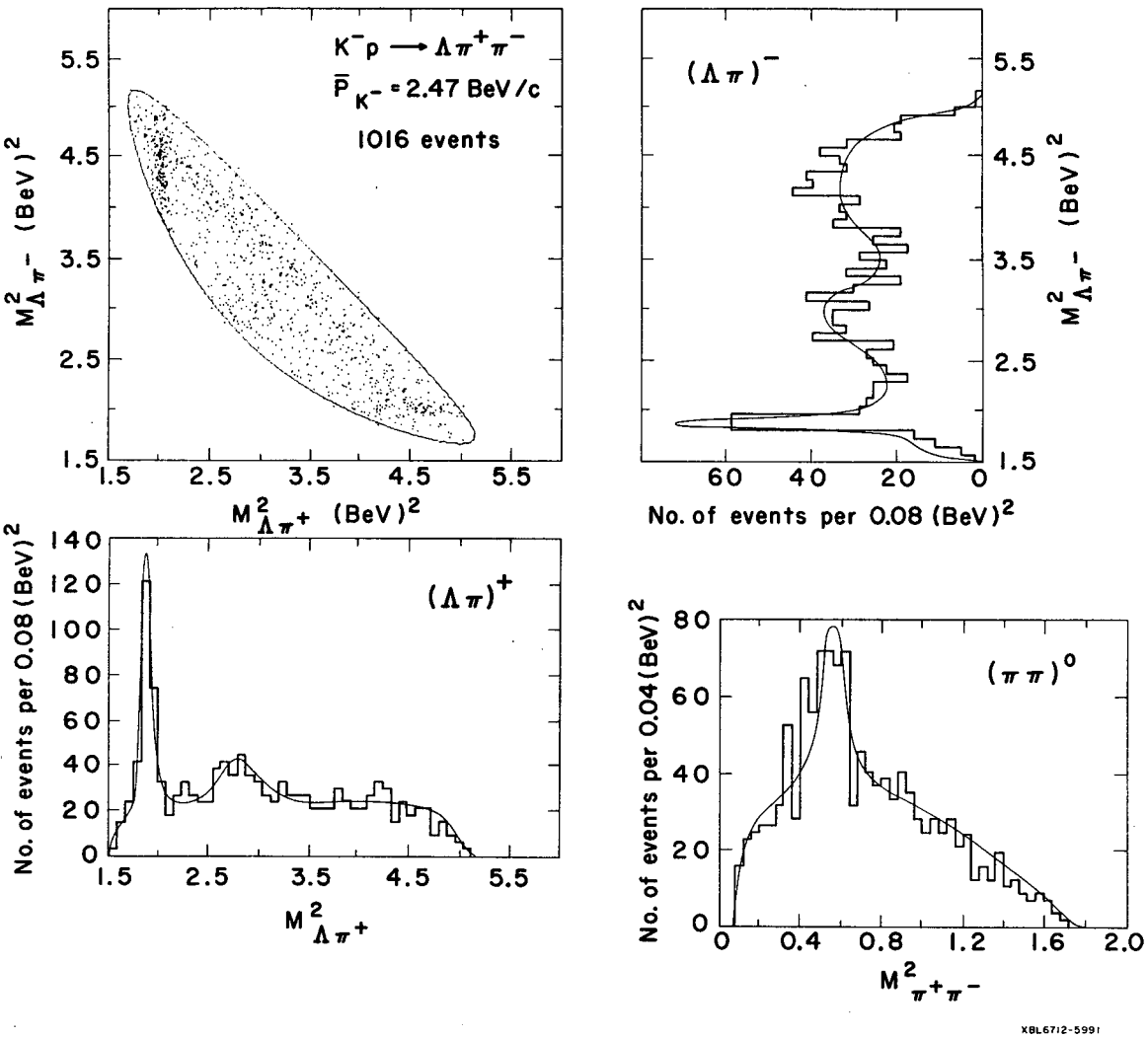

Fig. 32. Dalitz plot and projections for the reaction $K^- p \rightarrow \Lambda \pi^+ \pi^-$ at 2.47 Bev/c. The smooth curves represent Monte Carlo calculations.

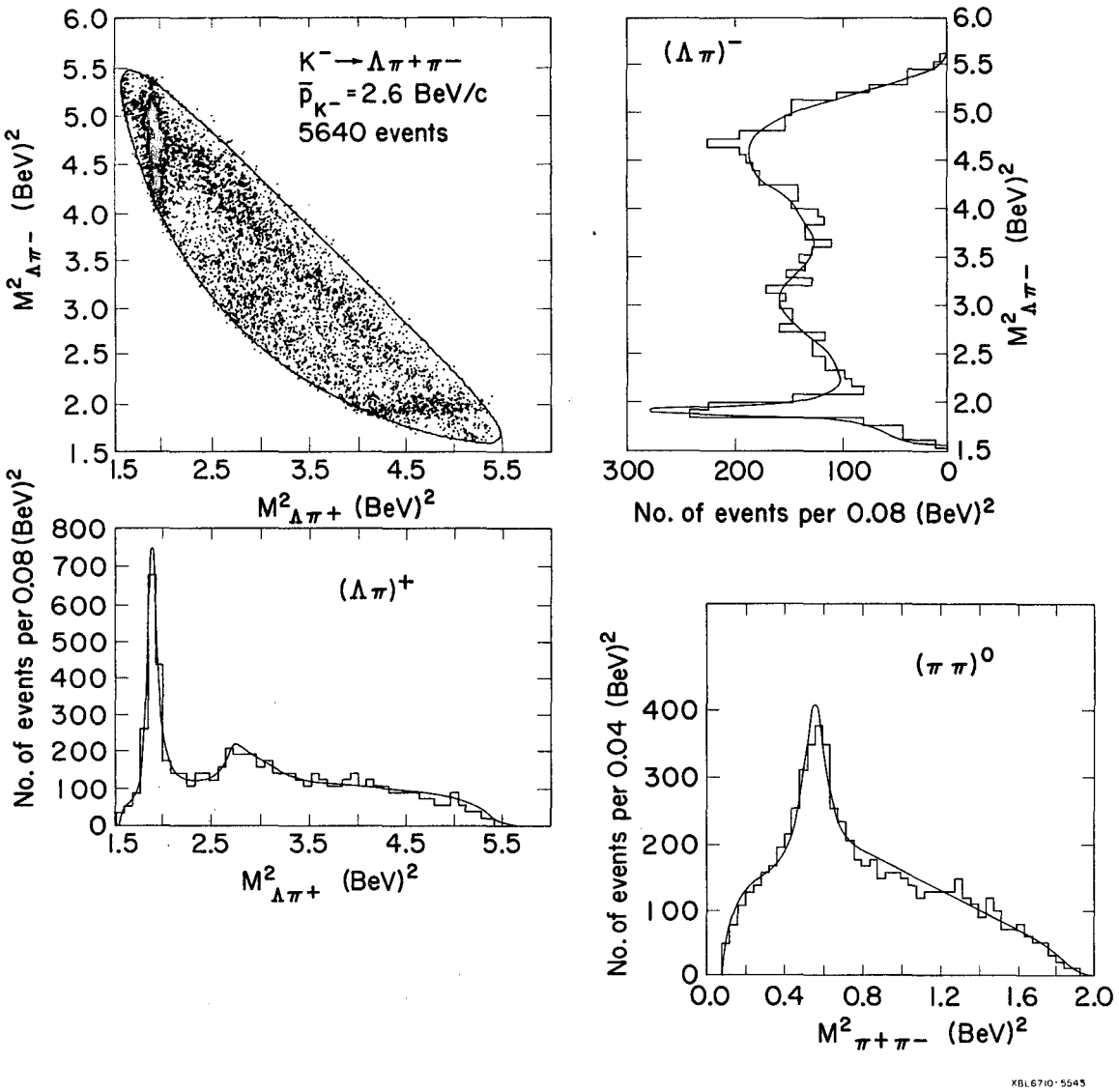

Fig. 33. Dalitz plot and projections for the reaction $K^-p \rightarrow \Lambda\pi^+\pi^-$ at 2.6 Bev/c. The smooth curves represent Monte Carlo calculations.

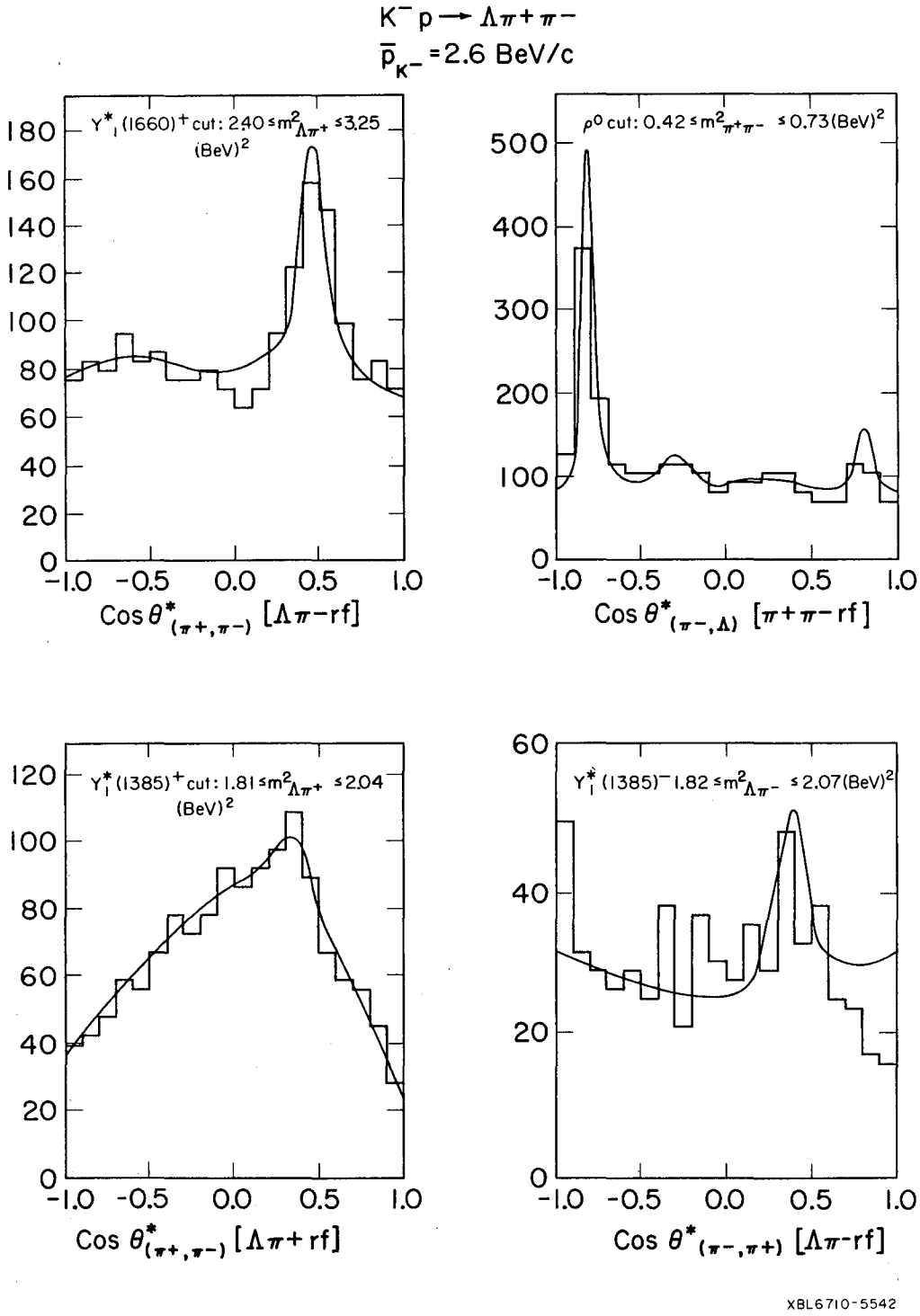

Fig. 34. Decay angular distributions relevant to $\Lambda\pi^+\pi^-$ Dalitz plot at 2.6 Bev/c. The smooth curves represent Monte Carlo calculations.

Table XIII. Fits for resonant amounts, masses, and widths in $K^-p \to \Lambda\pi^+\pi^-$

		Solutions		
	Parameters	$\bar{p}_{K^-}$ = 2.1 4424 events	$\bar{p}_{K^-}$ = 2.47 1016 events	$\bar{p}_{K^-}$ = 2.6 5640 events
Amounts:	$Y_1^*(1385)^+$	28.5±1.0	19.8±1.5	23.8±0.8
	$Y_1^*(1385)^-$	8.3±0.7	10.1±1.3	8.4±0.7
	$\Lambda^\circ\rho^\circ$	15.9±1.2	21.4±2.2	20.5±1.2
	$Y_1^*(1677)^+$	9.0±1.3	9.4±2.1	12.6±1.1
	$Y_1^*(1677)^-$	1.9±1.0	3.6±1.9	3.2±1.0
	$Y_1^*(1770)^+$	2.3±1.2	1.1±1.8	2.3±1.0
	$Y_1^*(1770)^-$	0[a]	5.1±1.8	2.2±0.8
$Y_1^*(1385)^+$:	m_o	1384.4±0.3	c	1384.0±0.9
	Γ^o	39.8±2.5		38.3±2.0
	d	-0.22±0.03		-0.26±0.03
$Y_1^*(1385)^-$:	m_o	1390.7±1.9		1393.5±1.7
	Γ^o	34.7±3.4		44.4±4.8
	d	-0.16±0.07		+0.18±0.06
ρ°:	m_o	767.1±6.7		751.6±3.1
	Γ^o	105.5[b]		105.5±8.2
	d	+0.33±0.06		+0.05±0.04
$Y_1^*(1677)$:	m_o	1681.0±8.2		1673.9±7.3
	Γ^o	94.9±12.2		140. ±25. [d]

a. The fit found negative values for this parameter, so it was fixed at zero.

b. No fit could be achieved for this parameter, so it was set to the solution found for $\bar{p}_{K^-}$ = 2.6 Bev/c.

c. These parameters were fixed for this small sample, at values obtained from interpolation between the 2.1 and 2.6 solutions.

d. The likelihood has no maximum as a function of this parameter in the region of relevance. The value and error quoted correspond to the center and width of a broad plateau (almost a saddle point).

Table XIV. Correlation Matrix for $\bar{p}_K$ = 2.6 Bev/c Fit.[a] Part I

	$1385^+ \pi^-$	$1385^- \pi^+$	$\Lambda^o \rho^o$	$1677^+ \pi^-$	$1677^- \pi^+$	$1770^+ \pi^-$
$1385^+ \pi^-$	1.00	+.18	-.13	-.01	+.19	+.09
$1385^- \pi^+$	+.18	1.00	-.01	+.13	+.13	+.13
$\Lambda^o \rho^o$	-.13	-.01	1.00	+.04	+.05	+.07
$1677^+ \pi^-$	-.01	+.13	+.04	1.00	+.18	-.40
$1677^- \pi^+$	+.19	+.13	+.05	+.18	1.00	-.05
$1770^+ \pi^-$	+.09	+.13	+.07	-.40	-.05	1.00
$1770^- \pi^+$	+.08	+.15	+.04	-.11	-.25	+.10
1385^+ m_o	+.11	+.04	+.02	+.00	+.04	+.02
1385^+ Γ	+.46	+.17	-.04	+.01	+.15	+.06
1385^+ d	+.07	+.06	+.15	+.03	+.07	+.05
1385^- m_o	+.05	+.17	+.03	+.04	+.02	+.03
1385^- Γ	+.17	+.56	+.04	+.10	+.06	+.10
1385^- d	-.08	-.17	+.19	-.02	-.01	-.01
ρ° m_o	-.06	-.05	+.15	-.01	-.04	-.01
ρ° Γ	-.03	-.01	+.61	+.04	+.02	+.05
ρ° d	-.09	-.14	+.07	+.11	+.02	+.11
1677 m_o	-.03	-.13	-.07	+.26	-.04	-.60
1677 Γ	+.04	+.09	+.01	+.59	+.13	-.27

[a] Correlations of the width of $Y_1^*(1677)$ are taken from the $\bar{p}_{K^-}$ = 2.1 Bev/c solution.

Table XIV. Correlation Matrix for $\bar{p}_{K^-}$ = 2.6 Bev/c Fit. Part II

		1770^-	1385^+			1385^-	
		π^+	m_o	Γ	d	m_o	Γ
$1385^+\pi^-$		+.08	-.09	+.46	+.07	+.05	+.17
$1385^-\pi^+$		+.15	+.04	+.17	+.06	+.17	+.56
$\Lambda^o\rho^o$		+.04	+.02	-.04	+.15	+.03	+.04
$1677^+\pi^-$		-.11	+.00	+.01	+.03	+.04	+.10
$1677^-\pi^+$		-.25	+.04	+.15	+.07	+.02	+.06
$1770^+\pi^-$		+.10	+.02	+.06	+.05	+.03	+.10
$1770^-\pi^+$		1.00	+.02	+.06	+.04	+.05	+.11
	m_o	+.02	1.00	+.26	+.02	+.01	+.03
1385^+	Γ	+.06	+.26	1.00	+.03	+.04	+.13
	d	+.04	+.02	+.03	1.00	+.02	+.04
	m_o	+.05	+.01	+.04	+.02	1.00	+.24
1385^-	Γ	+.11	+.03	+.13	+.04	+.24	1.00
	d	+.00	-.00	-.06	+.02	+.01	-.21
	m_o	+.00	-.02	-.04	+.06	+.00	-.04
ρ^o	Γ	+.04	+.01	-.02	+.09	+.02	+.01
	d	+.13	+.04	-.05	+.03	-.00	-.09
	m_o	-.24	+.00	-.00	-.03	-.03	-.10
1677	Γ	-.23	+.00	+.01	+.02	+.01	+.10

Table XIV. Correlation Matrix for $\bar{p}_K$- = 2.6 BeV/c Fit. Part III

		1385^-	ρ^o			1677	
		d	m_o	Γ	d	m_o	Γ
$1385^+\pi^-$		-.08	-.06	-.03	-.09	-.03	+.04
$1385^-\pi^+$		-.17	-.05	-.01	-.14	-.13	+.09
$\Lambda^o\rho^o$		+.19	+.15	+.61	+.07	-.07	+.01
$1677^+\pi^-$		-.02	-.01	+.04	+.11	+.26	+.59
$1677^-\pi^+$		-.01	-.04	+.02	+.02	-.04	+.13
$1770^+\pi^-$		-.02	-.01	+.05	+.11	-.60	-.27
$1770^-\pi^+$		+.00	+.00	+.04	+.13	-.24	-.23
1385^+	m_o	-.00	-.02	+.01	+.04	+.00	+.00
	Γ	-.06	-.04	-.02	-.05	-.00	+.01
	d	+.02	+.06	+.09	+.03	-.03	+.02
1385^-	m_o	+.01	+.00	+.02	-.00	-.03	+.01
	Γ	-.21	-.04	+.01	-.09	-.10	+.10
	d	1.00	+.11	+.15	+.17	+.01	+.02
ρ^o	m_o	+.11	1.00	+.21	+.01	+.01	+.01
	Γ	+.15	+.21	1.00	+.07	-.04	+.11
	d	+.17	+.01	+.07	1.00	-.04	+.12
1677	m_o	+.01	+.01	-.04	-.03	1.00	+.14
	Γ	+.02	+.01	+.11	+.12	+.14	1.00

The fit involves the amounts of the seven resonant processes listed, with the following parametrizations of the resonances themselves:

The $Y_1^*(1385)^+$ is assigned a p-wave Breit-Wigner resonance form R_1 (see Chapter III) with variable mass and width; likewise $Y_1^*(1385)^-$ and ρ^o. What is designated here as $Y_1^*(1677)$, is taken as a useful parametrization of the enhancements in this region, including $Y_1^*(1660)$ and $Y_1^*(1680)$, in terms of one simple Breit-Wigner (form R_2) with variable mass and width. (The physical significance of this parametrization is not clear, and the crossing of the positive and negative charge states on the Dalitz plot makes it difficult to further unravel these enhancements here.) The $Y_1^*(1770)$ is assigned a simple Breit-Wigner (form R_2) with the mass fixed at 1770 Mev and the width at 90 Mev.

Also parametrized in these fits are decay angular distributions of $Y_1^*(1385)^{\pm}$ and ρ^o. (More complete studies of the decay of $Y_1^*(1385)^+$ are undertaken in Section D of this chapter; here we are only interested in parametrizing variations in density along the resonance bands on the Dalitz plot.) The decay angular distributions were given the following forms, with variable parameters d (the angles used are defined and illustrated in Figure 35);

$$Y_1^*(1385)^+ : \frac{1}{\sqrt{4\pi}} + d\,Y_2^o(\cos\theta^*_{(\pi^+,\pi^-)}\,[\Lambda\pi^+ rf])$$

$$Y_1^*(1385)^- : \frac{1}{\sqrt{4\pi}} + d\,Y_2^o(\cos\theta^*_{(\pi^-,\pi^+)}\,[\Lambda\pi^- rf])$$

$$\rho^o : \frac{1}{\sqrt{4\pi}} + d\,Y_2^o(\cos\theta^*_{(\pi^-,\Lambda)}\,[\pi^+\pi^- rf])$$

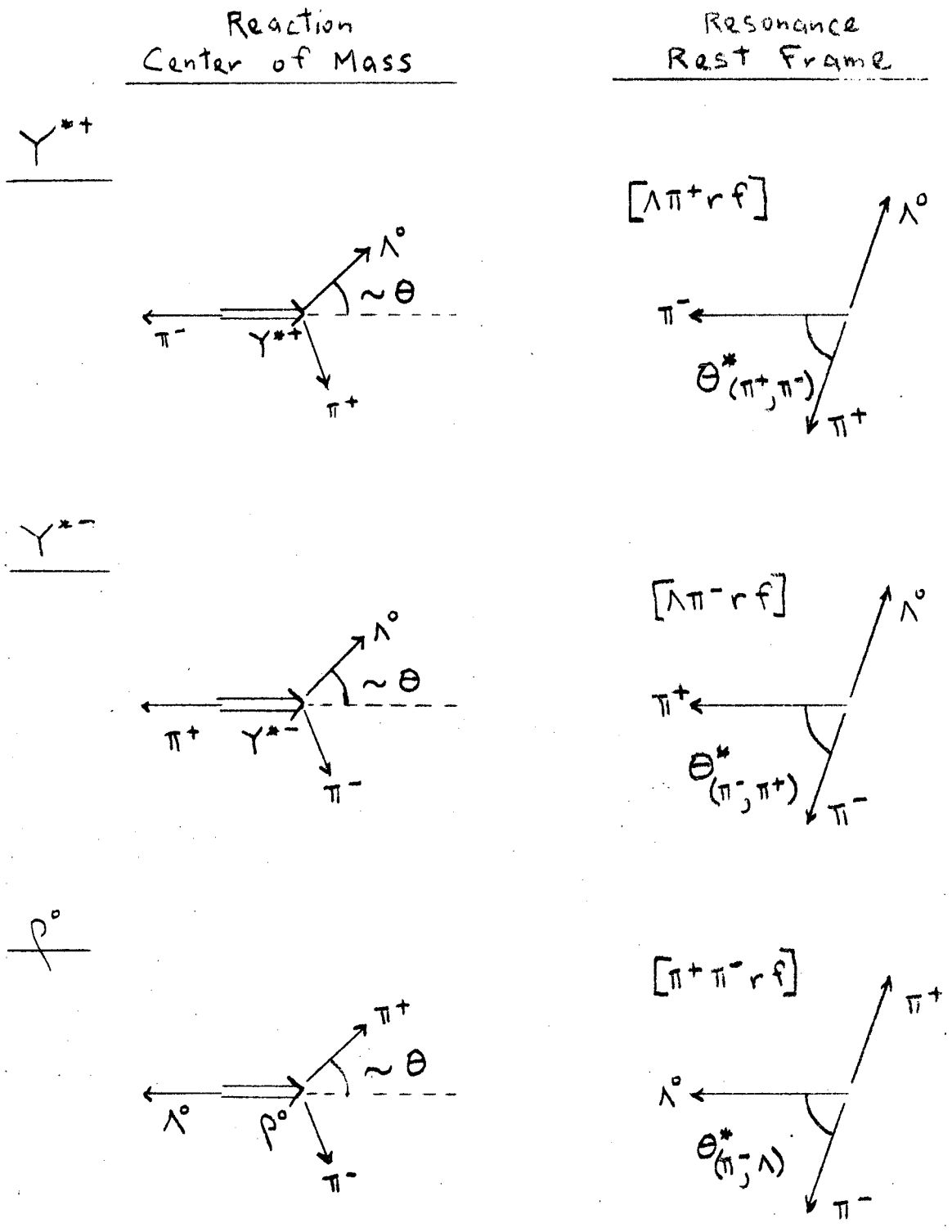

Fig. 35. Coordinate systems for resonance decay angular distributions relevant to $\Lambda\pi^+\pi^-$ Dalitz plot.

The solutions for amounts in Table XIII are converted directly into the cross sections presented in Table XV. Graphs of cross section versus beam momentum are presented in Figure 36, for $K^- p \rightarrow Y_1^*(1385)^{\pm} \pi^{\mp}$, and $K^- p \rightarrow \Lambda^o \rho^o$. The only deviation from smooth behavior of these cross sections (in the region of this experiment) which seems to be a candidate for interpretation in terms of an s-channel resonance is in Figure 36(a): an apparent shoulder in the falling $K^- p \rightarrow Y^{*+} \pi^-$ cross section in the region of $p_{K^-} = 2.1$ Bev/c, which corresponds to a center of mass energy of 2.27 Bev, close to the $Y_1^*(2250)$.[17] However, isotopic spin conservation would require an equally large bump in the $K^- p \rightarrow Y^{*-} \pi^+$ cross section, which is not observed. Thus we cannot assert an effect in our data.

The solutions for masses and widths (Table XIII) were similar enough at 2.1 and 2.6 Bev/c so that averaging appeared reasonable for subsequent analysis of production and decay angular distributions. The averaged and rounded values are presented in column A of Table XVI. In column B are recorded the values which were used for final analysis of the $\Lambda\pi^+\pi^o\pi^-$ state. Column C gives the numbers which are then used in subsequent analysis of this $\Lambda\pi^+\pi^-$ state; these are taken exactly equal to the numbers used previously in the $\Lambda\pi^+\pi^o\pi^-$ state, in the cases where agreement is good.

Monte Carlo Check

Monte Carlo calculations based on the above fits are compared with the data in Figures 30 through 34. Effective mass squared distributions as well as decay angular distributions are tested in

Table XV. Resonant amounts and cross sections in $K^- p \rightarrow \Lambda \pi^+ \pi^-$.

	$\bar{P}_{K^-}$ = 2.1 BeV/c		$\bar{P}_{K^-}$ = 2.47 BeV/c		$\bar{P}_{K^-}$ = 2.6 BeV/c	
Resonant Process	Percentage	σ (mb)	Percentage	σ (mb)	Percentage	σ (mb)
$Y_1^*(1385)^+\pi^-$	28.5±1.0	0.462±0.036	19.8±1.5	0.232±0.026	23.8±0.8	0.233±0.018
$Y_1^*(1385)^-\pi^+$	8.3±0.7	0.135±0.015	10.1±1.3	0.118±0.018	8.4±0.7	0.082±0.009
$\Lambda^0 \rho^0$	15.9±1.2	0.258±0.026	21.4±2.2	0.250±0.032	20.5±1.2	0.201±0.019
"$Y_1^*(1677)^+$"π^-	9.0±1.3	0.146±0.023	9.4±2.1	0.110±0.026	12.6±1.1	0.124±0.015
"$Y_1^*(1677)^-$"π^+	1.9±1.0	0.030±0.017	3.6±1.9	0.042±0.022	3.2±1.0	0.031±0.011
$Y_1^*(1770)^+\pi^-$	2.3±1.0	0.037±0.017	1.1±1.8	0.013±0.021	2.3±1.0	0.023±0.010
$Y_1^*(1770)^-\pi^+$	0.	0.	5.1±1.8	0.060±0.022	2.2±0.8	0.021±0.010
"Non-resonant" $\Lambda\pi^+\pi^-$	34.1±2.6	0.552±0.056	29.5±4.8	0.345±0.062	27.0±2.5	0.265±0.031
Totals	100.0	1.620±0.112	100.0	1.170±0.093	100.0	0.980±0.068

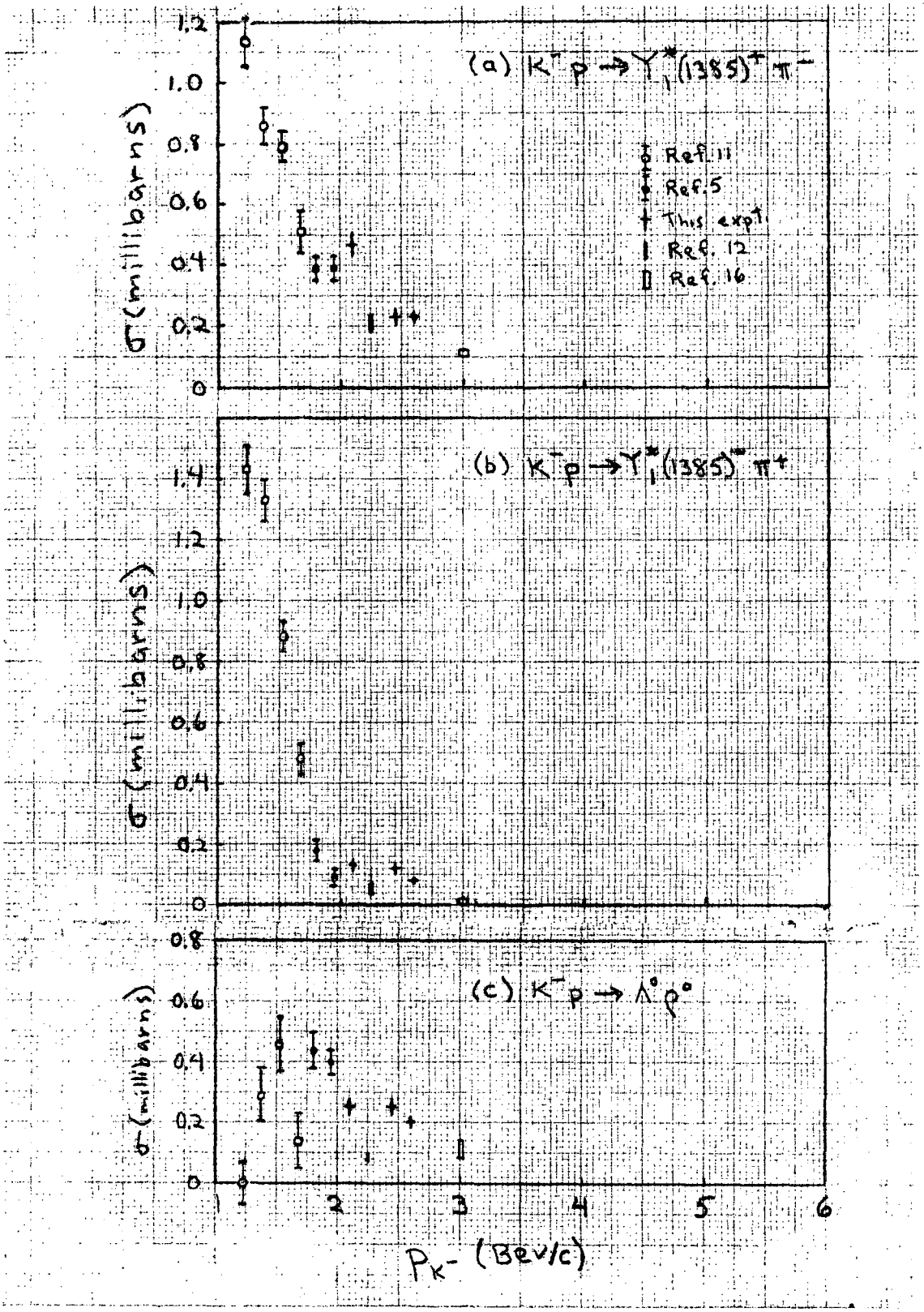

Fig. 36. Cross sections as a function of incident beam momentum for $K^- p \to Y_1^*(1385)^{\pm} \pi^{\mp}$ and $K^- p \to \Lambda^0 \rho^0$.

Table XVI. Resonance masses and widths for further analysis.

		A	B	C[a]
		$\Lambda\pi^+\pi^-$ solution (Mev)	$\Lambda\pi^+\pi^o\pi^-$ parametrization (MeV)	$\Lambda\pi^+\pi^-$ parametrization (MeV)
$Y_1^*(1385)^+$	M_o	1384±1	1384	1384
	Γ	39±2	37	37
$Y_1^*(1385)^-$	M_o	1392±2	1384	1392
	Γ	38±4	37	37
ρ^o	M_o	754±3	740	754
	Γ	105±9	100	100
$Y_1^*(1677)$	M_o	1677±7		1677
	Γ	104±12		104

a. These are the values used in further analysis of the $\Lambda\pi^+\pi^-$ state.

this way. We find that the effective mass squared distributions appear to be reasonably well accounted for, and the decay distributions indicate no substantial difficulties in the parametrization.

C. Production Angular Distributions

Production angular distributions for $K^- p \rightarrow Y_1^*(1385)^{\pm} \pi^{\mp}$ and $K^- p \rightarrow \Lambda^o \rho^o$ are obtained by the method outlined in Chapter III, Section B. All amounts are varied in the fits. The results are found in Tables XVII, XVIII, and XIX, and Figures 37 and 38. The only peripheral process with enough statistics to bear further analysis of decay distributions is $K^- p \rightarrow Y_1^*(1385)^+ \pi^-$, which is discussed in detail in the next section.

D. Peripheral Production and Decay of $Y_1^*(1385)^+$

The analysis is carried out in substantially the same manner as in Chapter IV, Section D, above, except for the following material differences: All amounts are allowed to vary along with the parameters describing the Y^{*+} decay correlations; this must be done because amounts and decay correlations are more strongly correlated here than in the four-body final state. The amount of background under the Y^{*+} peak is small here, ranging from a minimum of $0 \pm 8\%$ in the most forward bin to a maximum of $23 \pm 8\%$ in the bin with largest momentum transfer. Therefore, the results of the fits are compared directly with the unsubtracted data. The results and comparisons are presented in Tables XX and XXI, and Figures 39-44. No very serious discrepancies between the fits and the data are seen, so that the results may be used without much reservation. In Figure 39, the data at $\bar{p}_{K^-} = 2.1$ Bev/c

Table XVII. Fits for the Production Angular Distribution of $\bar{K}^- p \rightarrow Y_1^*(1385)^+ \pi^-$

	$\bar{p}_{K^-}$ = 2.1 BeV/c		$\bar{p}_{K^-}$ = 2.6 BeV/c	
$\cos\theta_{(Y^{*+},p)}$	Number of weighted events	Fraction of $Y^{*+}\pi^-$ (%)	Number of weighted events	Fraction of $Y^{*+}\pi^-$ (%)
1.0 to 0.8	1059	57.1 ± 2.2	1504	53.0 ± 1.9
0.8 to 0.6	773	40.1 ± 2.6	980	43.3 ± 2.1
0.6 to 0.4	546	25.2 ± 3.5	668	20.9 ± 2.1
0.4 to 0.2	484	30.2 ± 3.1	546	4.4 ± 1.8
0.2 to 0.0	506	20.2 ± 2.3	489	3.4 ± 1.5
0.0 to -.2	381	16.5 ± 3.8	447	4.8 ± 2.3
-.2 to -.4	327	15.7 ± 3.0	488	8.3 ± 2.2
-.4 to -.6	336	9.2 ± 2.6	471	10.8 ± 2.3
-.6 to -.8	357	8.8 ± 2.4	371	13.9 ± 2.6
-.8 to -1.	507	2.8 ± 1.8	549	0.7 ± 1.4
	5278		6509	

The factor which relates cross section to number of events is

(0.307 ± 0.021) microbarns/event for sample at 2.1 BeV/c,

(0.150 ± 0.010) microbarns/event for sample at 2.6 BeV/c.

At 2.1 BeV/c, $\cos\theta_{(Y^{*+},p)} = 1.0$ corresponds to $\Delta^2 = (p_{Y^{*+}} - p_p)^2 = -.04(\text{BeV/c})^2$,

$\cos\theta_{(Y^{*+},p)} = -1.0$ corresponds to $\Delta^2 = (p_{Y^{*+}} - p_p)^2 = 2.39(\text{BeV/c})^2$.

At 2.6 BeV/c, $\cos\theta_{(Y^{*+},p)} = 1.0$ corresponds to $\Delta^2 = (p_{Y^{*+}} - p_p)^2 = -.05(\text{BeV/c})^2$,

$\cos\theta_{(Y^{*+},p)} = -1.0$ corresponds to $\Delta^2 = (p_{Y^{*+}} - p_p)^2 = 3.28(\text{BeV/c})^2$.

Table XVIII. Fits for the Production Angular Distribution of $K^- p \rightarrow Y_1^*(1385)^- \pi^+$

	$\bar{p}_{K^-}$ = 2.1 BeV/c		$\bar{p}_{K^-}$ = 2.6 BeV/c	
$\cos \theta_{(Y^{*-}, p)}$	Number of weighted events	Fraction of $Y^{*-}\pi^+$ (%)	Number of weighted events	Fraction of $Y^{*-}\pi^+$ (%)
1.0 to 0.8	516	22.5 ± 7.2	597	23.1 ± 2.7
0.8 to 0.6	451	10.5 ± 2.4	535	5.4 ± 2.1
0.6 to 0.4	416	-0.7 ± 1.4	508	5.6 ± 1.7
0.4 to 0.2	456	9.4 ± 2.3	572	5.2 ± 1.5
0.2 to 0.0	532	3.2 ± 1.7	577	3.9 ± 1.6
0.0 to -.2	551	5.6 ± 2.0	629	7.8 ± 1.5
-.2 to -.4	535	6.6 ± 2.0	707	2.9 ± 1.2
-.4 to -.6	535	5.4 ± 1.6	745	4.7 ± 1.2
-.6 to -.8	590	12.5 ± 1.9	714	5.5 ± 1.5
-.8 to -1.	695	10.7 ± 1.8	925	13.8 ± 2.4
	5278		6509	

The factor which relates cross section to number of events is

(0.307 ± 0.021) microbarns/event for sample at 2.1 BeV/c

(0.150 ± 0.010) microbarns/event for sample at 2.6 BeV/c

At 2.1 BeV/c $\cos \theta_{(Y^{*-}, p)} = 1.0$ corresponds to $\Delta^2 = (p_{Y^{*-}} - p_p)^2 = -.04 (\text{BeV/c})^2$

$\cos \theta_{(Y^{*-}, p)} = -1.0$ corresponds to $\Delta^2 = (p_{Y^{*-}} - p_p)^2 = 2.39 (\text{BeV/c})^2$

At 2.6 BeV/c $\cos \theta_{(Y^{*-}, p)} = 1.0$ corresponds to $\Delta^2 = (p_{Y^{*-}} - p_p)^2 = -.05 (\text{BeV/c})^2$

$\cos \theta_{(Y^{*-}, p)} = -1.0$ corresponds to $\Delta^2 = (p_{Y^{*-}} - p_p)^2 = 3.28 (\text{BeV/c})^2$

Table XIX. Fits for the Production Angular Distribution of $K^- p \rightarrow \Lambda^o \rho^o$

	$\bar{p}_{K^-}$ = 2.1 BeV/c		$\bar{p}_{K^-}$ = 2.6 BeV/c	
$\cos \theta_{(\rho^o, p)}$	Number of weighted events	Fraction of $\Lambda^o \rho^o$ (%)	Number of weighted events	Fraction of $\Lambda^o \rho^o$ (%)
1.0 to 0.8	490	22.6 ± 3.6	536	28.6 ± 5.4
0.8 to 0.6	381	17.0 ± 4.3	433	11.8 ± 3.5
0.6 to 0.4	334	18.0 ± 4.4	498	17.3 ± 3.5
0.4 to 0.2	368	12.5 ± 4.3	471	24.9 ± 3.6
0.2 to 0.0	380	18.5 ± 4.3	540	20.8 ± 3.4
0.0 to -.2	451	21.4 ± 4.1	515	20.0 ± 3.3
-.2 to -.4	507	18.5 ± 4.5	502	14.3 ± 3.2
-.4 to -.6	528	18.2 ± 4.4	636	12.5 ± 3.0
-.6 to -.8	781	11.6 ± 2.9	855	11.4 ± 2.6
-.8 to -1.	1059	5.9 ± 2.5	1524	26.2 ± 2.0
	5278		6509	

The factor which relates cross section to number of events is

(0.307 ± 0.021) microbarns/event for sample at 2.1 BeV/c,

(0.150 ± 0.010) microbarns/event for sample at 2.6 BeV/c.

At 2.1 BeV/c, $\cos \theta_{(\rho^o, p)}$ = 1.0 corresponds to $\Delta^2 = (p_{\rho^o} - p_{K^-})^2 = 2.25 (\text{BeV/c})^2$,

$\cos \theta_{(\rho^o, p)}$ = -1.0 corresponds to $\Delta^2 = (p_{\rho^o} - p_{K^-})^2 = 0.06 (\text{BeV/c})^2$.

At 2.6 BeV/c, $\cos \theta_{(\rho^o, p)}$ = 1.0 corresponds to $\Delta^2 = (p_{\rho^o} - p_{K^-})^2 = 3.20 (\text{BeV/c})^2$,

$\cos \theta_{(\rho^o, p)}$ = -1.0 corresponds to $\Delta^2 = (p_{\rho^o} - p_{K^-})^2 = 0.04 (\text{BeV/c})^2$.

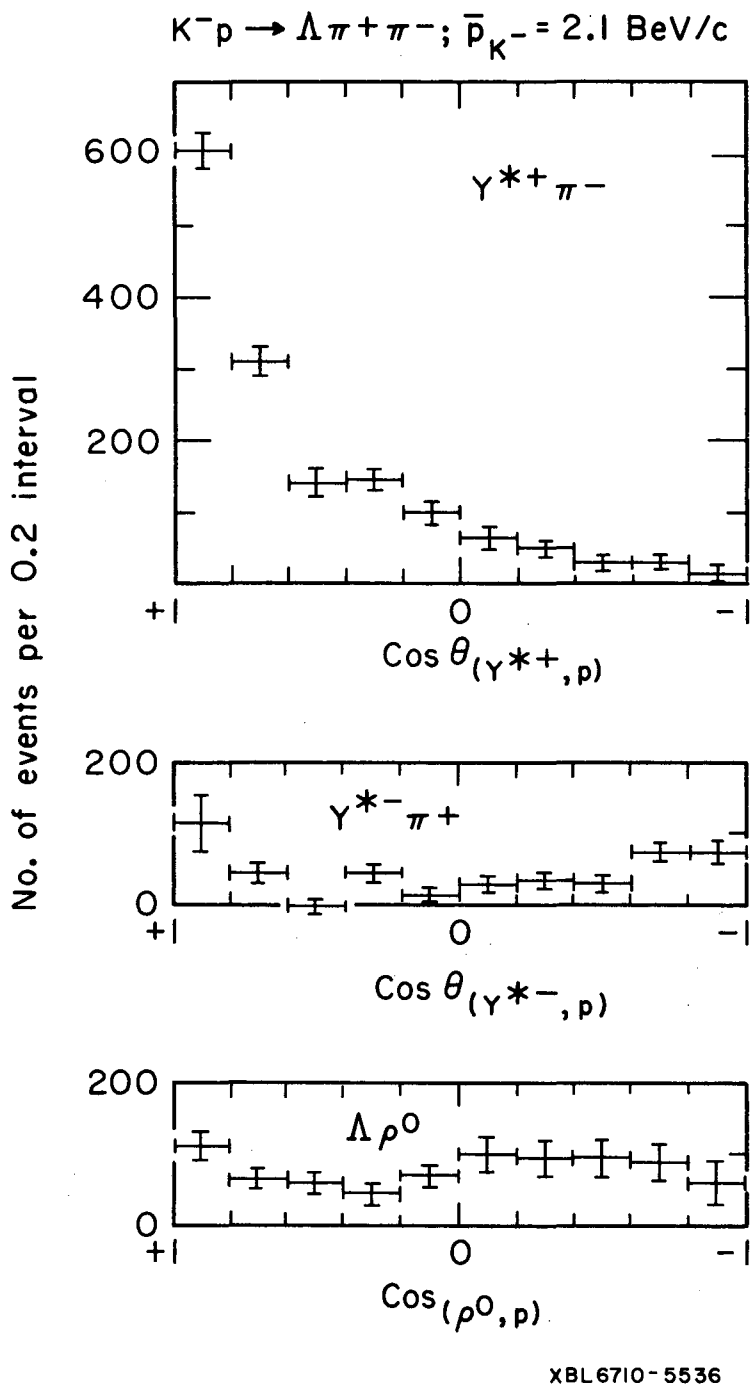

Fig. 37. Production angular distributions, in the reaction center of mass, for $K^- p \rightarrow Y_1^{*}(1385)^{\pm} \pi^{\mp}$ and $K^- p \rightarrow \Lambda^0 \rho^0$ at 2.1 Bev/c.

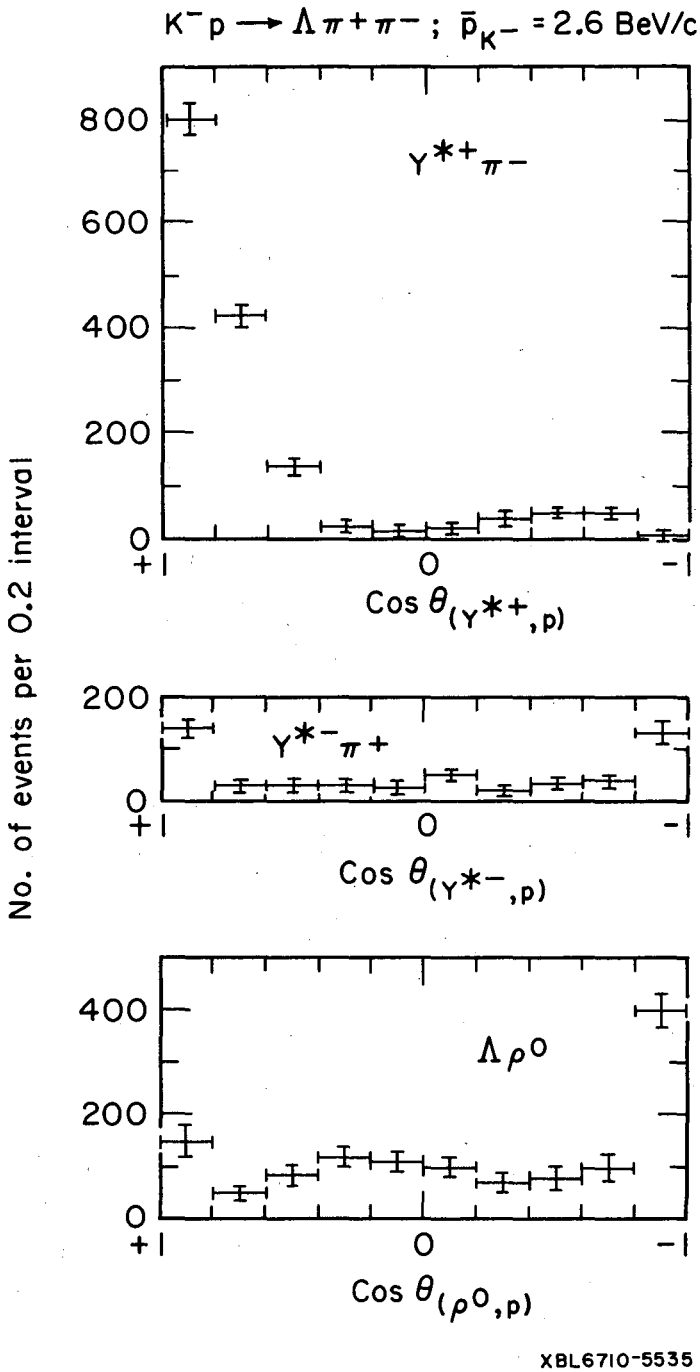

Fig. 38. Production angular distributions, in the reaction center of mass, for $K^- p \rightarrow Y_1^*(1385)^{\pm} \pi^{\mp}$ and $K^- p \rightarrow \Lambda^0 \rho^0$ at 2.6 Bev/c.

Table XX. Fits of peripheral $Y^*_1(1385)^+ \pi^-$ at $\bar{P}_{K^-}$ = 2.1 BeV/c.

$\cos\theta_{(Y^{*+},p)}$	$\Delta^2(\mathrm{GeV/c})^2$	No. of weighted events	Fraction of $Y^{*+}\pi^-$ (%)	Density Matrix Elements		
				ρ_{33}	Re ρ_{31}	Re $\rho_{3,-1}$
1.0 to 0.9	-.04 to +.08	515	55.2 ± 3.2	.19 ± .04	.09±.04	.18 ± .04
0.9 to 0.8	+.08 to +.20	544	57.3 ± 3.0	.33 ± .04	-.02±.03	.28 ± .04
0.8 to 0.6	+.20 to +.45	773	39.4 ± 2.8	.24 ± .05	.05±.04	.28 ± .05
0.6 to 0.4	+.45 to +.69	546	25.3 ± 3.4	.39 ± .07	.02 ± .07	.20 ± .07

Table XXI. Fits of peripheral $Y_1^*(1385)^+ \pi^-$ at $\bar{P}_{K^-}$ = 2.6 BeV/c.

$\cos\theta_{(Y^{*+},p)}$	Δ^2 $(GeV/c)^2$	No. of weighted events	Fraction of $Y^{*+}\pi^-$ (%)	Density Matrix Elements		
				ρ_{33}	Re ρ_{31}	Re$\rho_{3,-1}$
1.00 to 0.95	-.05 to +.03	439	50.1±3.4	.19±.05	.13±.04	.18±.04
0.95 to 0.90	+.03 to +.12	369	48.4±3.7	.26±.06	.07±.05	.28±.05
0.90 to 0.85	+.12 to +.20	375	56.2±3.6	.27±.05	.06±.04	.27±.04
0.85 to 0.80	+.20 to +.28	321	59.3±4.2	.26±.05	.00±.05	.23±.04
0.80 to 0.70	+.28 to +.45	531	42.3±3.1	.39±.04	-.02±.03	.33±.04
0.70 to 0.60	+.45 to +.62	449	43.6±3.1	.33±.05	-.08±.04	.17±.05
0.60 to 0.40	+.62 to +.95	668	20.5±2.0	.46±.05	-.01±.05	.25±.06

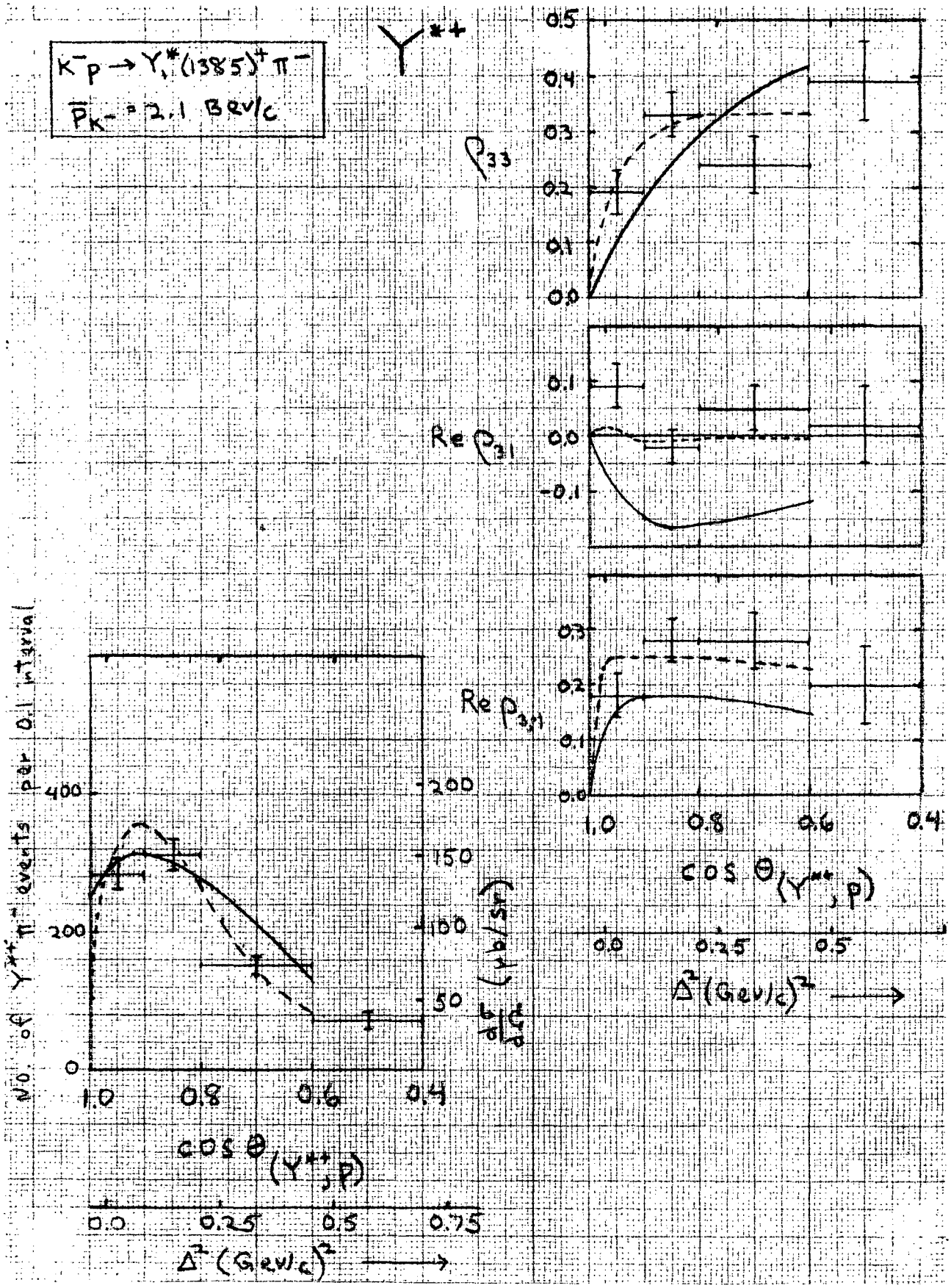

Fig. 39. Differential cross section for $K^- p \to Y_1^*(1385)^+ \pi^-$, and spin-density-matrix elements for $Y_1^*(1385)^+$ as a function of production angle, at 2.1 Bev/c. The smooth curves are calculations of Jackson et. al.[20] (see text).

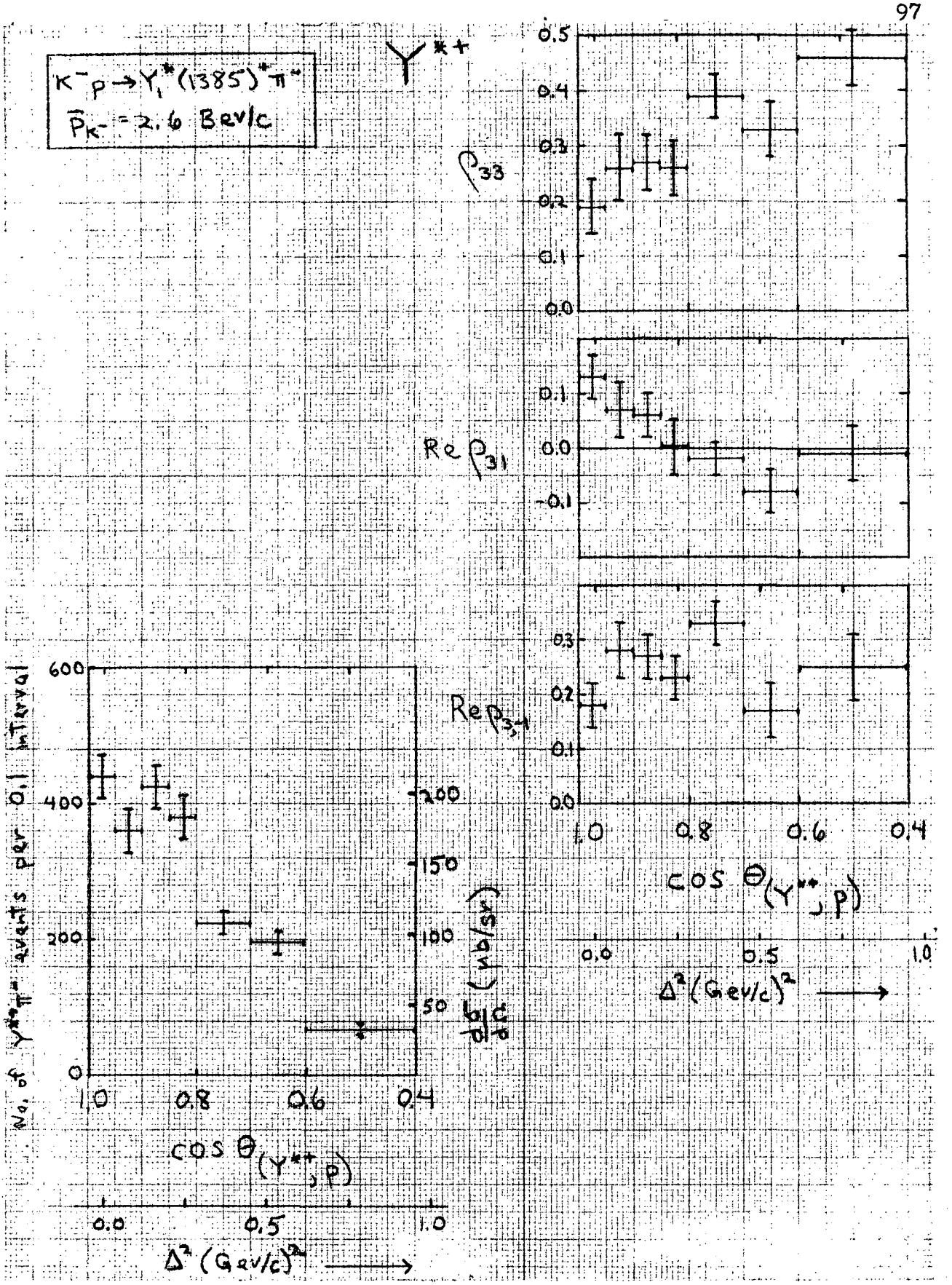

Fig. 40. Differential cross section for $K^- p \to Y_1^*(1385)^+ \pi^-$, and spin-density-matrix elements for $Y_1^*(1385)^+$ as a function of production angle, at 2.6 Bev/c.

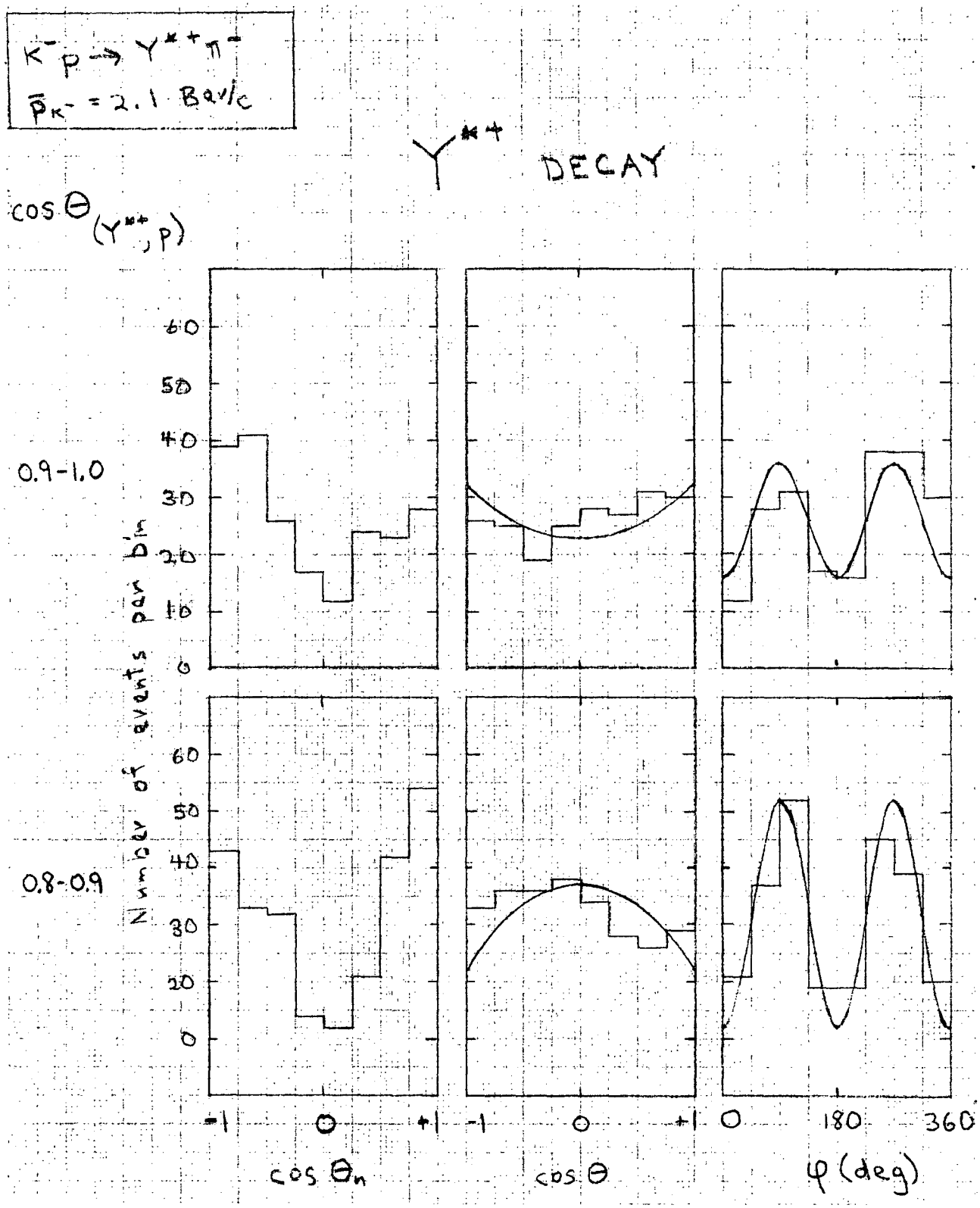

Fig. 41. Decay angular distributions for $Y_1^*(1385)^+$: the smooth curves represent the spin-density-matrix elements in Fig. 39, while the corresponding histograms are of events with 1.81 $(\text{Bev})^2 \leq m^2_{\Lambda\pi^+} \leq$ 2.04 $(\text{Bev})^2$ ($\bar{p}_{K^-}$ = 2.1 Bev/c, Part I).

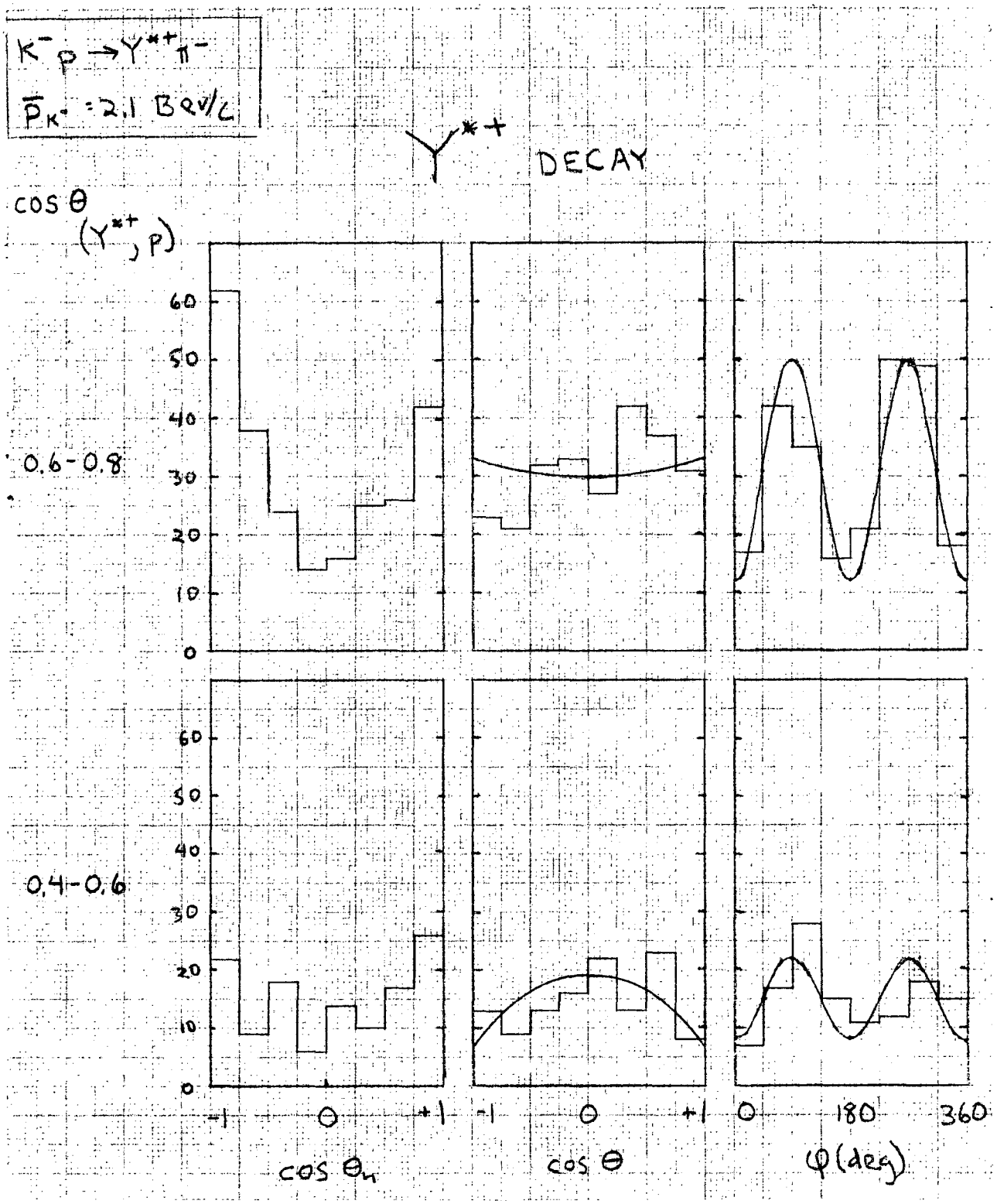

Fig. 42. Decay angular distributions for $Y^*(1385)^+$: the smooth curves represent the spin-density-matrix elements in Fig. 39, while the corresponding histograms are of events with 1.81 $(\text{Bev})^2 \leq m^2_{\Lambda\pi^+} \leq 2.04$ $(\text{Bev})^2$ ($\bar{p}_{K^-}$ = 2.1 Bev/c, Part II).

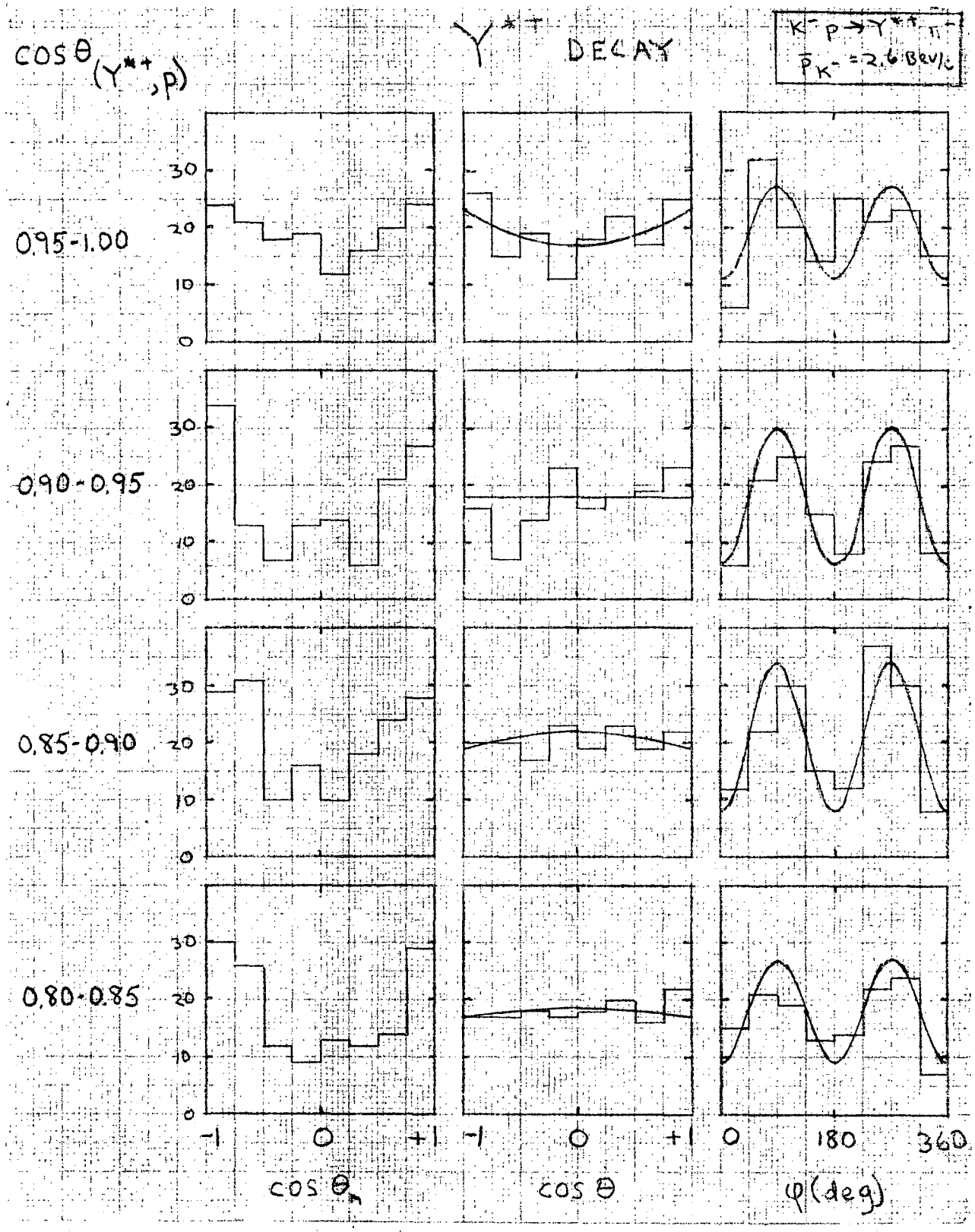

Fig. 43. Decay angular distributions for $Y_1^*(1385)^+$: the smooth curves represent the spin-density-matrix elements in Fig. 40, while the corresponding histograms are of events with 1.81 (Bev)$^2 \leq m^2_{\Lambda\pi^+} \leq$ 2.04 (Bev)^2 ($\bar{p}_{K^-}$ = 2.6 Bev/c, Part I).

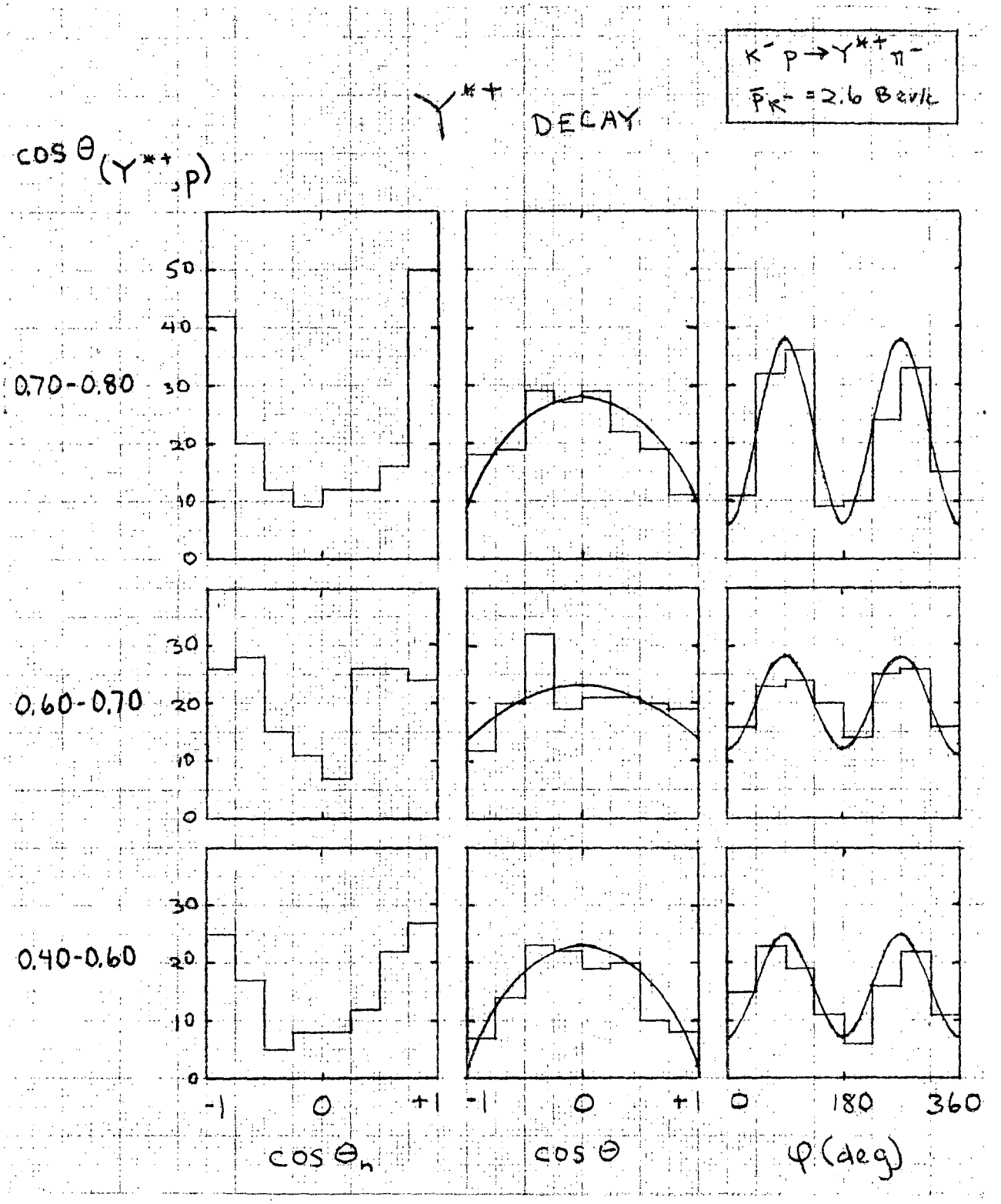

Fig. 44. Decay angular distributions for $Y_1^*(1385)^+$: the smooth curves represent the spin-density-matrix elements in Fig. 40, while the corresponding histograms are of events with 1.81 $(\text{Bev})^2 \leq m^2_{\Lambda\pi^+} \leq$ 2.04 $(\text{Bev})^2$ ($\bar{p}_{K^-}$ = 2.6 Bev/c, Part II).

are compared with calculations of Jackson[20] for the same reaction at 2.24 Bev/c. The solid curves were calculated from the relativistic magnetic dipole coupling model of K^* exchange with absorption parameters $C_+ = 0.70$, $\gamma_+ = 0.077$. The dashed curve shows the effect of an intrinsic form factor $F(\Delta^2) = M^2/(\Delta^2 + M^2)$ with $M = 0.9$ Bev. (The differential cross section curves have been normalized to correspond to our data.) Reasonable agreement is found with the calculations including the form factor.

VI. $Y_1^*(1385)^{+}_{o}$ MASSES AND WIDTHS

A. $Y_1^*(1385)^{+}_{o}$ Masses

Evidence from $K^- p \to \Lambda\pi^+\pi^-$

The measurements of the $Y_1^*(1385)^+$ and $Y_1^*(1385)^-$ masses exhibited in Table XIII, Chapter V, are expected to be relatively free from additional systematic error for the following reasons: the events used here result from four-constraint fits; the sample appears to be relatively uncontaminated and unbiased with respect to hypothesis separation; and the resonances as well as the backgrounds under them have been quite exhaustively parametrized, with correlations taken into account.

The solutions for the $\bar{p}_{K^-} = 2.1$ Bev/c and $\bar{p}_{K^-} = 2.6$ Bev/c samples are consistent; however, as the 2.6 sample is slightly more suspect with respect to systematic errors (see appendix A), we shall use only the 2.1 solution. Rounding errors upward, to reflect uncertainties on the error itself arising from its estimation in the fit, we obtain the following results:

$$M_{Y_1^*(1385)^+} = 1384.4 \pm 1 \text{ Mev}$$

$$M_{Y_1^*(1385)^-} = 1390.7 \pm 2 \text{ Mev}$$

$$M_{Y^{*-}} - M_{Y^{*+}} = 6.3 \pm 2 \text{ Mev}$$

Evidence from $K^- p \to \Lambda\pi^+\pi^o\pi^-$

The arguments advanced above for small systematic errors in the $\Lambda\pi^+\pi^-$ case all lead to the opposite conclusion here, and in fact

the various solutions in Table V (Chapter IV) are seen to be quite inconsistent on the basis of statistical errors alone. The complexity of this final state makes it difficult to sort out the various possible systematic errors, and efforts in this direction have been unsuccessful. The fits suggest a mass for the neutral $Y_1^*(1385)$ in the neighborhood of 1388 Mev.

B. $Y_1^{\backslash *}(1385)$ Width

The evidence from the $\Lambda\pi^+\pi^-$ final state again appears reasonably consistent and reliable, and we again use the solution from the $\bar{p}_{K^-}$ = 2.1 Bev/c sample:

$$\Gamma_{Y_1^*(1385)^+} = 36 \pm 3 \text{ Mev}$$

$$\Gamma_{Y_1^*(1385)^-} = 31 \pm 4 \text{ Mev}$$

(The experimental resolution, $\sigma \cong 3$ MeV, has been unfolded.[23]) The results from $\Lambda\pi^+\pi^o\pi^-$ are again unreliable. Taking into account experimental resolution and known systematic difficulties, all fitted $Y_1^*(1385)$ widths are consistent with a true width of around 36 Mev.

ACKNOWLEDGEMENTS

I would like to thank Professor Ronald R. Ross for the generous and humane guidance which he has given me, and my wife Ruth for moral support. This work would not have been possible without the efforts of many others in the Alvarez Group and at the Lawrence Radiation Laboratory.

This work was supported by the U. S. Atomic Energy Commission.

APPENDICES

A. Bubble Chamber Magnetic Field

In order to deduce the momentum of a particle from the curvature of its track, one must have knowledge of the magnetic field. This is usually obtained by direct measurement of the magnetic field in the bubble chamber while it is empty and at room temperature. While these measurements are quite precise, the magnetic properties of the materials of the bubble chamber may change at liquid hydrogen temperatures, altering the magnetic field. We have measured some such effect by analysis of tau and lambda decays.

Our experiment may be divided into two parts as follows: approximately one half of the events were processed through PACKAGE using the magnetic field measured directly in the chamber. About halfway through the run a short circuit occurred in one of the bubble chamber magnet windings. The coil was then permanently shorted out, and the run continued, but with an altered magnetic field. The new field was quickly measured in the following manner: (It was assumed that the shape of the field had not changed appreciably, so that just one parameter, a scale factor, had to be measured. Later direct measurement showed that, for purposes of this analysis, the assumption was true enough.) Various scale factors were tried, and a sample of some 100 lambda decays were fitted using each scale factor. The scale factor which lead to the smallest chi squared's for the fits was chosen. About half of the events were processed through PACKAGE using this scale factor, which amounted to some 6 o/o. The two parts of the sample will be referred to, respectively, as the "before" sample (before the bubble chamber coil short)

and the "after" sample (after the bubble chamber coil short).

In figure 45(a) we see gaussian ideograms of the mass squared of the K^- as estimated from the measured momenta of its decay products in the tau mode ($K^- \rightarrow \pi^-\pi^-\pi^+$) for "before" and "after" samples of events which fit the tau decay hypothesis. Figure 45(b) shows similar ideograms for lambda decays. The mass squared scales for the tau and the lambda have been so arranged that the masses squared quoted in the compilation of Rosenfeld and co-workers[18] for the tau and lambda fall directly below the zero point of the scale at the very top of figure 45. Thus the after samples are seen to peak up at approximately the correct values, while the before samples peak at lower values for both the tau and the lambda. (The error bars at the top of the figure indicate the errors on m^2_τ and m^2_Λ from the Rosenfeld compilation, scaled to their respective scales below.)

The m^2_τ and m^2_Λ scales also have the following property: The position of the peak of a distribution measured on the "magnetic field deviation" scale at the top tells you what percentage of magnetic field error would move the peak from the correct value to that value. Thus we conclude that the "before" magnetic field is off by -1.0±0.3 %, while the "after" magnetic field is off by -0.2±0.3 %. (We would expect this behavior of the "after" field, because it was set to give the right lambda mass, essentially).

In carrying out the separation procedure of Chapter II, measured momenta were scaled to correct for these magnetic field errors. The uncertainties in this scaling procedure are the major contribution to the discrepancies between the various curves in figure 5(a), for example.

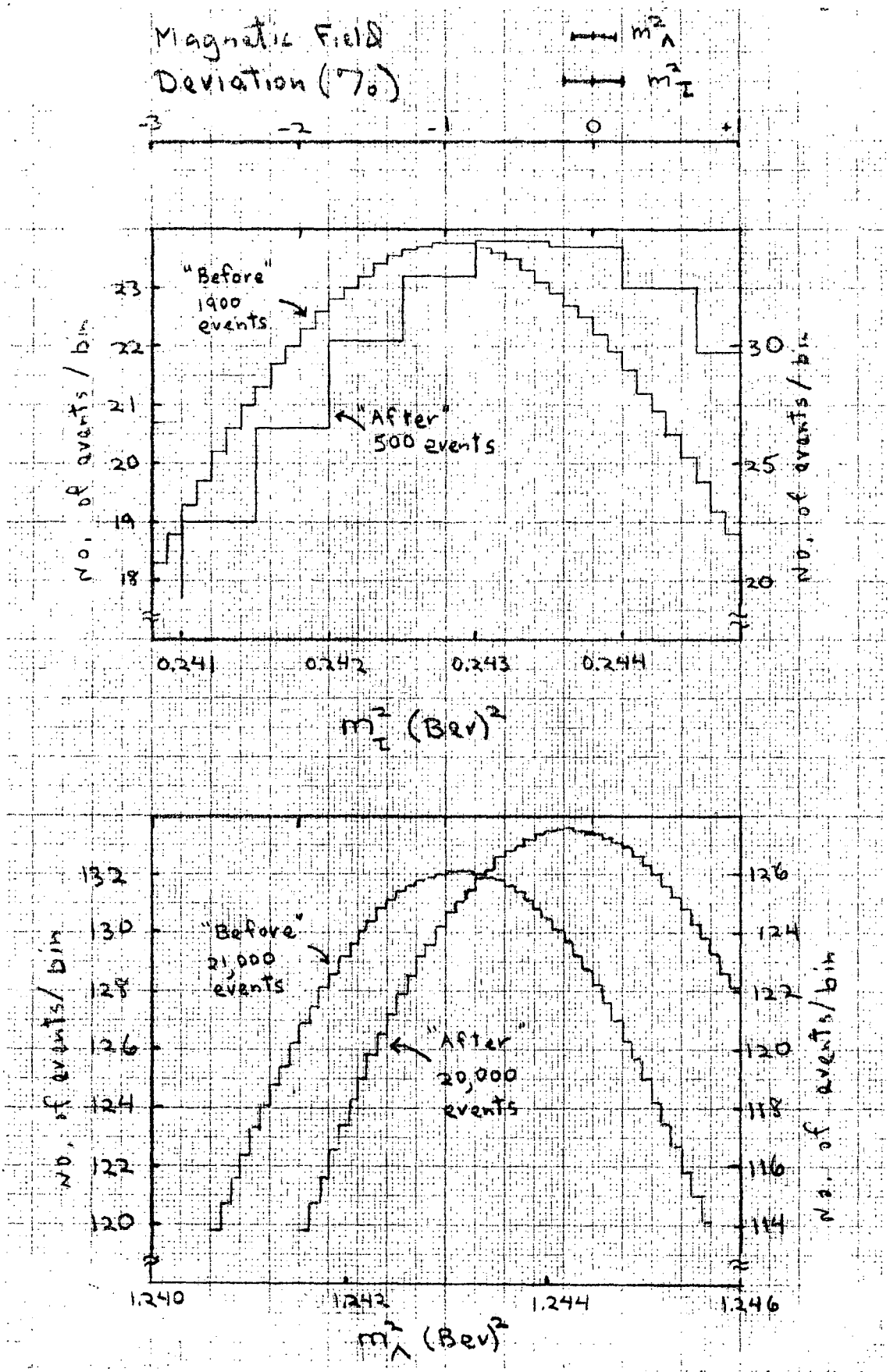

Fig. 45. Gaussian ideograms of tau and lambda masses, for samples taken before and after a short occurred in the bubble chamber magnet coil (see text).

The subsequent analyses based on fitted data were not corrected. Thus the "after" sample is essentially correct, while the "before" sample will exhibit systematic distortions due to a 1 °/o field error. In the $K^- p \rightarrow \Lambda \pi^+ \pi^-$ sample, consisting of 4-constraint fitted events, the effects are too small to be detected. In the $K^- p \rightarrow \Lambda \pi^+ \pi^o \pi^-$ 1-constraint events, these effects are dealt with explicity.

B. Weighting of Events

Short-length scanning losses of lambda decays, as well as escape losses, are dealt with by cut-off and weighting procedures. Events are included in the samples for analysis if and only if: The distance from production to decay of the lambda, projected on the scanning plane, is greater than 0.5 cm; and the production and decay vertices are both within a volume bounded by certain planes which are inside the bubble chamber and close to the walls. An event which is accepted is then weighted by the inverse of the probability that a lambda with such a (vector) momentum would decay in the region of acceptance:

$$W = 1/\left(e^{-D/\eta c \tau_\Lambda \cos\theta} - e^{-L/\eta c \tau_\Lambda} \right)$$

Where D=0.5 cm., $\eta = \frac{P\Lambda}{m_\Lambda}$, τ_Λ is the lifetime of the lambda, θ is the angle between the direction of the lambda and the scanning plane, and L is the distance from the production vertex, along the line of flight of the lambda, to the closest of the planes which define the acceptance volume. A typical distribution of resulting weights is shown in Table XXII.

Weighted events are used in all data displays, (except for distributions of beam momentum) but the total number of events quoted for any sample is unweighted. Weighted events are used in all fits; Though they are treated in a statistically correct manner, so that large weights are acceptable, no weights greater than 10 are used, for computational reasons.

Table XXII. Weights for $K^- p \to \Lambda \pi^+ \pi^o \pi^-$ events; $P_{K^-} > 2.3$ BeV/c.

Weight	Number of events
1.0-1.5	12,598
1.5-2.5	324
2.5-3.5	51
3.5-4.5	15
4.5-5.5	6
5.5-6.5	3
6.5-7.5	1
7.5-8.5	1
8.5-9.5	1
11.5-12.5	2
15.5-16.5	1

C. Approximation in FIT

A time-saving approximation in the program which we use to find the maximum of a likelihood function--FIT, developed by Philippe Eberhard--is basic to the feasibility of our analysis. This approximation makes use of the particular form of the logarithm of the likelihood function as a sum over events to approximate second derivatives:

$$w(\alpha) = \sum_i \ln f(x_i;\alpha) \quad ; \quad \text{briefly,} \quad w(\alpha) = \sum_i \ln f_i$$

$$\frac{\partial^2 w}{\partial\alpha_\mu \partial\alpha_\nu} = \frac{\partial^2}{\partial\alpha_\mu \partial\alpha_\nu}\left(\sum_i \ln f(x_i;\alpha)\right)$$

$$= \sum_i \frac{\partial^2 \ln f_i}{\partial\alpha_\mu \partial\alpha_\nu}$$

$$= \sum_i \frac{\partial}{\partial\alpha_\mu}\left(\frac{1}{f_i}\frac{\partial f_i}{\partial\alpha_\nu}\right)$$

$$= \sum_i \; -\frac{1}{f_i^2}\frac{\partial f_i}{\partial\alpha_\mu}\frac{\partial f_i}{\partial\alpha_\nu} \; + \; \frac{1}{f_i}\frac{\partial^2 f_i}{\partial\alpha_\mu \partial\alpha_\nu}$$

$$= -\sum_i \left(\frac{1}{f_i}\frac{\partial f_i}{\partial\alpha_\mu}\right)\left(\frac{1}{f_i}\frac{\partial f_i}{\partial\alpha_\nu}\right) + \sum_i \frac{1}{f_i}\frac{\partial^2 f_i}{\partial\alpha_\mu \partial\alpha_\nu}$$

$$= -\sum_i \left(\frac{\partial \ln f_i}{\partial\alpha_\mu}\right)\left(\frac{\partial \ln f_i}{\partial\alpha_\nu}\right) + (\sim 0)$$

The second sum is approximated to zero as follows: we assume that, for values of the parameters close to the solution, the distribution function $f(x;\alpha)$ adequately describes the true distribution of events in the space of the variables x which describe the individual events. Then, in the limit of large statistics, a sum over events may be converted to an integral over the variables x:

$$\sum_i^N h(x_i) \xrightarrow[\text{large statistics}]{} N\int dx\, f(x;\alpha)\, h(x)$$

Thus,

$$\sum_i \frac{1}{f(x_i;\alpha)} \frac{\partial^2 f(x_i;\alpha)}{\partial\alpha_\mu \partial\alpha_\nu}$$

$$\longrightarrow N\int dx\, f(x;\alpha)\left(\frac{1}{f(x;\alpha)} \frac{\partial^2 f(x;\alpha)}{\partial\alpha_\mu \partial\alpha_\nu}\right)$$

$$= N\int \frac{\partial^2 f(x;\alpha)}{\partial\alpha_\mu \partial\alpha_\nu}\, dx$$

$$= N \frac{\partial^2}{\partial\alpha_\mu \partial\alpha_\nu}\int f(x;\alpha)\, dx$$

$$= 0 \text{ , as } \int f(x;\alpha)\, dx = 1 \quad \text{(normalized distribution function)}$$

Eberhard points out that the second derivative matrix calculated in this way not only has the property of being "correct" near the maximum of the function w (α) if $f(x;\ \alpha_{\text{solution}})$ is the true distribution function, but is in any case negative semi-definite and hence will give rise to a step toward the maximum even if we are in a region of the function w(α) where the true second derivative is positive.

D. Subtraction Method for $Y^{*+}\rho^-$ Decay Distributions

We will discuss first a subtraction method for finding the amount of $K^-p \to Y^*\rho$, and then generalize to decay angular distributions. Figure 46 is a schematic drawing of a scatter plot of $\Lambda\pi$ mass versus $\pi\pi$ mass. The regions labeled A, B, C, and D may be characterized respectively as the $Y^*\rho$ intersection, the Y^* band, the ρ band, and the background region. These regions are chosen to be sensitive to four

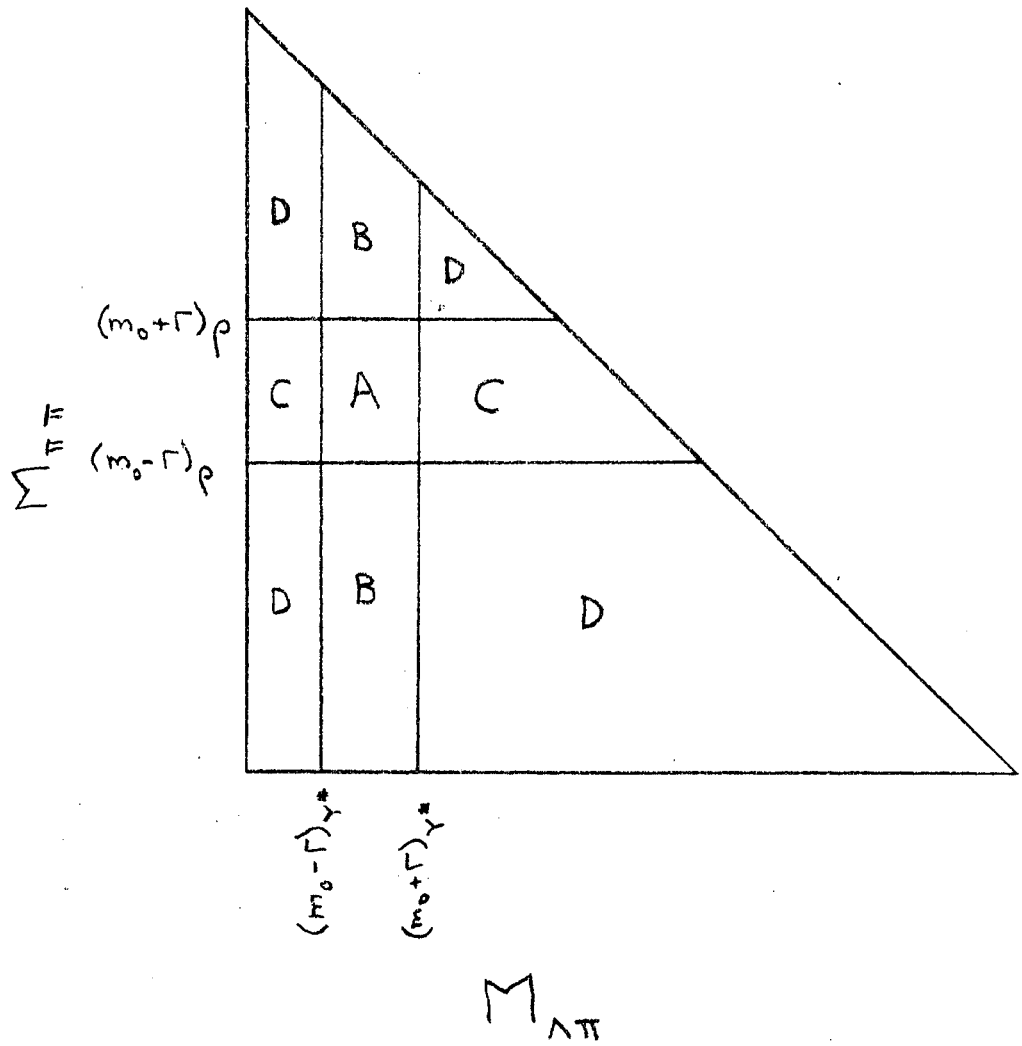

Fig. 46. Schematic scatter plot of $\Lambda\pi$ mass versus $\pi\pi$ mass.

different populations which populate the scatter plot: $Y^*\rho$ events, $Y^*\pi\pi$ events, $\rho\Lambda\pi$ events, and all others. By a Monte Carlo technique, we calculate the distribution into the four regions of each of these populations: we find the fractions $F_{\alpha\beta}$ which tell how the population of events β is distributed into the regions α. (This calculation for the background, including phase space and all other resonant processes, is based on the relative amounts derived from the fits in Chapter IV.) The number of events in the α-th region, N_α (α = A,B,C,D), can then be related to the number of events in the β-th population N_β ($\beta = Y^*\rho$, $Y^*\pi\pi$, $\rho\Lambda\pi$, background):

$$N_\alpha = F_{\alpha\beta} N_\beta$$

Solving for the N_β

$$N_\beta = (F_{\alpha\beta})^{-1} N_\alpha$$

yields, in particular, the number of $Y^*\rho$ events.

Now, if we have for example a sample of events which contains some $Y^{*+}\rho^-$, and we want to find the distribution into some bins of some angle φ which describes the direction of the π^+ in the Y^{*+} rest frame, we divide our sample up into subsamples chosen appropriately on the basis of the angle φ of the π^+ in the $\Lambda\pi^+$ rest frame, and carry out the above procedure to find the number of $Y^{*+}\rho^-$ events in each sub-sample. We thus find the number of $Y^{*+}\rho^-$ which have a Y^{*+} decaying into each chosen φ interval.

Cuts on Y^{*+} or ρ^- decay angles do not affect the distributions of $\Lambda\pi^+$ or $\pi^0\pi^-$ masses, so the fractions $F_{\alpha\beta}$ will not be altered, for

β corresponding to $Y^{*+}\rho^-$, $Y^{*+}\pi^o\pi^-$, or $\rho^-\Lambda\pi^+$. However, for the background, which includes other resonant processes, the fractions F must be recalculated for each production and decay angular interval considered.

FOOTNOTES AND REFERENCES

1. J. J. Murray, J. Button-Shafer, F. T. Shively, G. H. Trilling, J. A. Kadyk, A. Rittenberg, D. M. Siegel, J. A. Lindsey, and D. W. Merrill, A Separated 2.5 to 2.8 Gev/c K^- Beam at the Bevatron, XII International Conference on High Energy Physics, Dubna, 1964, (Atomizdat, Moscow, 1966), Vol. 2, p. 541.

2. P. G. Davey, R. I. Hulsizer, W. E. Humphrey, J. H. Munson, R. R. Ross, and A. J. Schwemin, Scanning and Measuring Projector, Review of Scientific Instruments 35, 1134 (1964).

3. James S. Lindsey and Gerald A. Smith, Production Properties and Decay Modes of the ϕ Meson, Physical Review 147, 913 (1966).

4. The problem of M^2_{miss}, when there is in fact no missing system, is dealt with by S. G. Wojcicki and F. T. Solmitz, Missing Mass Calculations, Alvarez Group Physics Memo No. 367 (1962). Otherwise, $M^2_{\Lambda+miss}$, M^2_{miss}, and E_{miss} have close to gaussian distributions if they depend in reasonably linear fashion on primitive measurements.

5. Lewis Taylor Smith, Resonance Production in K^-p Interactions at 1.80 to 1.95 Gev/c (Ph.D. Thesis, University of California, Los Angeles, 1966).

6. J. Friedman and R. Ross, Maximum Likelihood Estimate of Resonant State Production in Multiparticle Final States, Alvarez Group Programming Memo P-102, LRL (1964). (unpublished)

7. Jay Orear, Notes on Statistics for Physicists, UCRL-8417 (1958).

8. A. Barbaro-Galtieri (Lawrence Radiation Laboratory), private communication.

9. Philippe Eberhard (Lawrence Radiation Laboratory), private communication.

10. J. D. Jackson, Peripheral Production and Decay Correlations of Resonances, Reviews of Modern Physics 37, 484 (1965).

11. Darrell O. Huwe, Study of the Reaction $K^- + p \rightarrow \Lambda + \pi^+ + \pi^-$ from 1.2 to 1.7 Bev/c, (Ph.D. Thesis), UCRL-11291 (1964).

12. G. W. London, R. R. Rau, N. P. Samios, S. S. Yamamoto, M. Goldberg, S. Lichtman, M. Prime, and J. Leitner, K^- - p Interaction at 2.24 Bev/c, Physical Review 143, 1034 (1966).

13. E. S. Gelsema, J. C. Kluyver, A. G. Tenner, M. Demoulin, J. Goldberg, B. P. Gregory, G. Kayas, P. Kreybich, C. Pelletier, M. Ville, R. Barloutaud, A. Leveque, C. Louedec, J. Meyer, and A. Verglas, K^- - p Interactions at 3 Gev/c, Proceedings of the Sienna International Conference on Elementary Particles, (Societa Italiana Di Fisica, Bologna), Vol. 1, p. 134.

14. J. Mott, R. Ammar, R. E. P. Davis, W. Kropac, F. Schweingruber, M. Derrick, T. Fields, L. G. Hyman, J. Loken, and J. Simpson, Meson + Hyperon Final States in K^-p Interactions at 4.1 and 5.5 Gev/c, Physical Review Letters 18, 355 (1967).

15. Leo Stodolsky and J. J. Sakurai, Vector Meson Exchange Model for Isobar Production, Physical Review Letters 11, 90 (1963).

16. Peter Schlein (Department of Physics, University of California at Los Angeles), private communication.

17. Early reports of $Y_1^*(2250)$ include: Blanpied et al., PRL 14, 741 (1965); Bock et al., PL 17, 166 (1965); and Cool et al., PRL 16, 1228 (1966).

18. A. H. Rosenfeld, N. Barash-Schmidt, A. Barbaro-Galtieri, W. J. Podolsky, L. R. Price, Matts Roos, Paul Soding, W. J. Willis, and C. G. Wohl, Data on Particles and Resonant States, UCRL-8030 (Sept. 1967).

19. Draper, Humphrey and Ross, Confidence Level for Events Adjusted by the Method of Least Squares with Constraints, Alvarez Group Physics Memo No. 347, LRL (1964). (unpublished)

20. J. D. Jackson, J. T. Donohue, K. Gottfried, R. Keyser, and B. E. Y. Svensson, Peripheral Production and Decay of Resonances in High-Energy Meson-Nucleon Collisions, Physical Review 139, B428 (1965).

21. Orin I. Dahl, Lyndon M. Hardy, Richard I. Hess, Janos Kirz, and Donald H. Miller, Strange-Particle Production in $\pi^- p$ Interactions from 1.5 to 4.2 Bev/c Part I, UCRL-16978 (1967).

22. M. Derrick, T. Fields, J. Loken, R. Ammar, R. E. P. Davis, W. Kropac, J. Mott, and F. Schweingruber, Excited Hyperon of Mass 1680 Mev, Physical Review Letters 18, 266 (1967).

23. We have used the following approximate relationship (found by numerical folding of Breit-Wigner line shapes with Gaussians):

$$\Gamma_{observed} \cong \Gamma_{real} + \tfrac{5}{4}\sigma_{resolution}, \text{ for } \sigma_{resolution} < \tfrac{1}{2}\Gamma_{real}$$

where Γ_{real} is the full width at half-maximum of the Breit-Wigner, $\sigma_{resolution}$ is the standard deviation of the Gaussian representing the experimental resolution, and $\Gamma_{observed}$ characterizes the resulting almost-Breit-Wigner line shape as would our maximum-likelihood fitting procedure. (In terms of

the full width at half-maximum of the Gaussian resolution function,

$$\Gamma_{resolution} = 2.36\ \sigma_{resolution}$$

our relationship becomes

$$\Gamma_{observed} \cong \Gamma_{real} + 0.5\ \Gamma_{resolution}$$

which falls between the linear relationship for the folding of Breit-Wigners and the square-root-of-squares relationship for Gaussians.)